MICROCOPY RESOLUTION TEST CHART

AD-A193 093

A Final Report to

U. S. Navy

for

The Collection of Statistics on the Frequency of
Cloud Cover Over North America

Contract # N00014-85-K-0581

University of Wisconsin Account #144W850

for the period of

1 July 1985 to 30 September 1987

submitted by

Edwin W. Eloranta
Donald P. Wylie
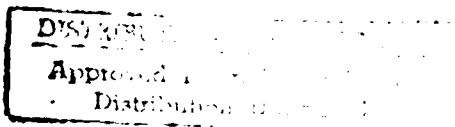
Space Science and Engineering Center
at the University of Wisconsin-Madison
1225 West Dayton Street
Madison, Wisconsin 53706
(608) 262-0544

February 1988

88 3 17 056

FINAL REPORT

CONTRACT TITLE: The Collection of Statistics on the Frequency of Cloud Cover
Over North America

NUMBER: N00014-85-K-0581

PRINCIPAL INVESTIGATORS: Edwin W. Eloranta
                                  (608) 262-7327

                                  and

                                  Donald P. Wylie
                                  (608) 263-7458
                                  Space Science and Engineering Center
                                  University of Wisconsin-Madison

CONTRACT MONITOR: Dr. P. F. Twitchell

TECHNICAL OBJECTIVES: To collect statistics on cloud cover and atmospheric
obstructions to lidar propagation.

APPROACH: We are using the GOES/VAS satellite for collecting statistics on
cloud cover. The VAS sensor on this satellite has 12 spectral channels which
can be used for defining the partially transmissive cirrus clouds. These
cirrus clouds have been confused with lower altitude opaque clouds in past
satellite studies. With the GOES/VAS system we are determining what
percentage of the cloud cover is partially transmissive. We have collected
1.75 years of data and are currently studying the geographic, seasonal and
temporal variations in cloud cover--both those that are transmissive and those
that are opaque to terrestrial radiation.

     We are calibrating the satellite data with lidar data. The High Spectral
Resolution (HSRL) lidar measures the vertical profile of extinction of visible
lidar energy by clouds and other atmospheric obstructions. The extinction and
total optical depth measurements of the lidar are being compared to satellite
derived estimates of cloud emissivity and optical depth to calibrate the
satellite data so that geographical statistics of lidar attenuation can be
produced.

ACCOMPLISHMENTS DURING FY 1987: In FY 1987 we completed 1.75 years of
satellite observations. We found that the probability of clouds opaque to
terrestrial radiation is approximately 45 percent. Partially transmissive
cirrus clouds were found 25 to 35 percent of the time and no clouds (clear
skies) were detected 20 to 25 percent of the time. The desert southwest had
the least opaque cloud cover. Partially transmissive cirrus clouds also
varied geographically but the transmissive cirrus cloud cover was more uniform
than the opaque cloud cover. Diurnal and seasonal variances in cloud cover
also were found and are discussed in the attached papers (Appendices A and B).

     We are in the process of analyzing our lidar data. We have data on
clouds with optical depths from 0.01 to 1.0. Many details of the spatial
structure of these clouds also have been revealed by the lidar data.

Quantitative measurements of extinction and optical depth also have been made of "invisible cirrus" clouds which can obstruct aircraft sensors. More details are given in Appendices C and D.

SIGNIFICANCE OF RESULTS: We have found that partially transmissive cirrus clouds account for a large fraction of the cloud cover reported by other studies. This class of cloud cover does not fully block observing systems or energy propagation. With the lidar data we intend to provide radiative transfer information so that the potential obscuration to sensors or energy transmission systems can be predicted.

FUTURE EFFORTS: We intend to continue enlarging our satellite and lidar data sets. More data are needed to produce accurate statistics. We have just begun examining cloud radiative transfer data from the HSRL lidar. Lidar-satellite comparisons will be made in the upcoming year.

PUBLICATIONS:

Wylie, D. P., and W. P. Menzel, 1988: "Cloud cover statistics using VAS", SPIE Conf. Proceedings on Optoelectronics and Laser Applications in Science and Engineering Symposium on Innovative Science and Technology, Los Angeles, CA, January 13, 1988.

Eloranta, Edwin W., and Christian J. Grund, 1988: "Lidar observations of cirrus cloud parameters," SPIE Conf. Proceedings on Optoelectronics and Laser Applications in Science and Engineering Symposium on Innovative Science and Technology, Los Angeles, CA, January 13, 1988.

Grund, C. J., 1987: "Measurements of cirrus cloud optical properties by high spectral resolution LIDAR, PhD thesis; Dept. of Meteor., University of Wisconsin-Madison, 92 pp.

Grund, C. J., 1987: "Thermally induced spectral drift cancellation in pressure-tuned Fabry-Perot etalons", App. Opt., in publication (Feb).

Grund, C. J. and E. W. Eloranta, 1987: "High spectral resolution lidar measurements of cirrus cloud optical properties", paper MD-9 Tech. Digest: Topical meeting on Laser and Optical Remote Sensing, Cape Cod, MA.

Grund, C. J. and E. W. Eloranta, 1987: "Optically significant cirrus couds may be rendered invisible to spaceborne simple lidar systems", paper MC10, Tech. Digest: Topical meeting on Laser and Optical Remote Sensing, Cape Cod, MA.

Wylie, D. P., P. Grimm and W. P. Menzel, 1988: "Cloud cover statistics from GOES/VAS", AMS Third Conf. on Sat. Meteor., Anaheim, CA, 4 Feb. 1988.

4/word/DW/reports/N0581.fr

APPENDIX A

Third Conference on Satellite Meteorology and Oceanography sponsored by the American Meteorological Society, 31 January, 1988, Anaheim, CA

CLOUD COVER STATISTICS FROM GOES/VAS

Donald P. Wylie, Peter Grimm

Space Science and Engineering Center
University of Wisconsin-Madison
Madison, Wisconsin

W. Paul Menzel

NOAA/NESDIS Advanced Satellite Products Project
Madison, Wisconsin

1. INTRODUCTION

The frequency of occurrence of cirrus clouds usually has been underestimated in cloud population studies. Satellite methods of analyzing cloud cover often mistake cirrus clouds for lower level clouds or completely miss them, because their infrared brightness temperatures are warmer than the temperature associated with their true altitudes. Thin cirrus are especially hard to identify on visible satellite images because they reflect little solar radiation and appear as dark or broken cloud fields. With the multi-spectral infrared sensor on the GOES-VAS satellite the identification of most cirrus is now possible.

A technique for deriving cloud top altitudes from the VAS infrared sensor was developed by Menzel (1983). It is also applicable to the polar orbiting High-resolution Infrared Radiometer Sounder (HIRS). The technique takes advantage of infrared channels with partial CO_2 absorption where the different channels are sensitive to different levels in the atmosphere. Thus, clouds appear on each channel in proportion to their level in the atmosphere. Low clouds will not appear at all on the high level channels, while high clouds appear on all channels. By modelling the upwelling infrared radiation from the earth atmosphere system in several VAS channels simultaneously, it is possible to infer the cloud top height independent of radiative transmissivity of the cloud. This gives the CO_2 technique the ability to distinguish thin cirrus clouds that would normally be missed by other techniques due to the transmission of terrestrial radiation through the cirrus.

The CO_2 technique has been installed on the Man-computer Interactive Data Access System (McIDAS) at the University of Wisconsin-Madison. It has been run operationally using the GOES-VAS imagery starting in October 1985. Statistics on cloud cover and especially cirrus cloud cover are being gathered for the continental United States and its bordering oceans. This paper describes the techniques and some of the first results of this program.

2. CO_2 TECHNIQUE DESCRIPTION

The VAS radiometer detects infrared radiation in twelve spectral bands that lie between 3.9 and 15 microns at 7 or 14 km resolution in addition to visible reflections at 1 km resolution. The 15 micron CO_2 band channels provide a good sensitivity to the temperature of relatively cold regions of the atmosphere. A demonstration of the vertical resolution of the three relevant CO_2 channels is given by the temperature profile weighting functions shown in Fig. 1. Each curve in the figure shows the sensitivity of the radiance observed in the spectral interval of the indicated channel to local variations in atmospheric temperature. As may be seen, only clouds above the 350 mb level will have strong contributions to the radiance to space observed by the 14.2 micron band (VAS channel 3), while the 14.0 micron band (VAS channel 4) senses down to 700 mb and the 13.3 micron band (VAS channel 5) senses down near the surface of the earth.
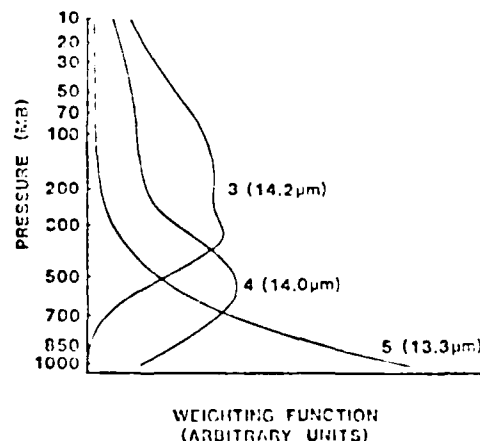

Fig. 1. The temperature profile weighting function of radiance to space as a function of emitting level for the VAS CO_2 spectral bands centered at 14.2, 14.0, and 13.3 microns.

To assign a cloud top pressure to a given cloud element, the ratio of the deviations in cloud produced radiances, $I(\nu)$, and the corresponding clear air radiances, $I_{cl}(\nu)$, for two spectral channels of frequency ν_1 and ν_2 viewing the same field-of-view is written as

$$\frac{I(\nu_1) - I_{cl}(\nu_1)}{I(\nu_2) - I_{cl}(\nu_2)} = \frac{\epsilon_1 \int_{P_s}^{P_c} \tau(\nu_1, p)\frac{dB[\nu_1,T(p)]}{dp} dp}{\epsilon_2 \int_{P_s}^{P_c} \tau(\nu_2,p)\frac{dB[\nu_2,T(p)]}{dp} dp}$$

In this equation ϵ is the cloud emittance, P_s the surface pressure, P_c the cloud pressure, $\tau(\nu, p)$ the fractional transmittance of radiation of frequency ν emitted from the atmospheric pressure level (p) arriving at the top of the atmosphere (p = 0), and $B[\nu,T(p)]$ is the Planck radiance of frequency ν for temperature $T(p)$. If the frequencies are close enough together, then $\epsilon_1 \approx \epsilon_2$, and one has an expression by which the pressure of the cloud within the field-of-view (FOV) can be specified. The left side of equation (1) is determined from the VAS observed radiances and clear air radiances provided from spatial analyses of VAS clear-sky radiance observations. The right side of equation (1) is calculated from a temperature profile and the profiles of atmospheric transmittance for the spectral channels as a function of P_c, the cloud top pressure (discrete values at ~50 mb intervals spanning 1000 to 100 mb are used). In this study, global forecast temperature and moisture fields from the National Meteorological Center (NMC) are used. The optimum cloud top pressure is determined when the absolute difference |right (ν_1, ν_2) - left (ν_1, ν_2, P_c)| is a minimum.

Once a cloud height has been determined, an effective cloud amount can be evaluated from the infrared window channel data using the relation

$$N\epsilon = \frac{I(w) - I_{cl}(w)}{B[w, T(P_c)] - I_{cl}(w)}$$

Here N is the fractional cloud cover within the FOV, Nc the effective cloud amount, w represents the window channel frequency, and $B[w, T(p_c)]$ is the opaque cloud radiance.

Using the ratios of radiances of the three CO_2 spectral channels, three separate cloud top pressures can be determined (14.2/14.0, 14.0/13.3, and 14.2/13.3). If $(I - I_{cl})$ is within the noise response of the instrument $(\sim 1$ mW m^{-2} - sr^{-1} - cm^{-1}) the resulting P_c is rejected. Using the infrared window and the three cloud top pressures, three effective cloud amount determinations are made. As described by Menzel (1983), the most representative cloud height and amount are those that best satisfy the radiative transfer equation for the three CO_2 channels.

If no ratio of radiances can be reliably calculated because $(I - I_{cl})$ is within the instrument noise level, then a cloud top pressure is calculated directly from the VAS observed 11.2 micron infrared-window channel brightness temperature and the temperature profile. In this way all clouds are assigned a cloud top pressure either by CO_2 or infrared-window calculations.

The CO_2 technique is independent of the fractional cloud cover; heights and effective cloud amounts can be determined for partially cloudy FOVs. However, the CO_2 technique sees only the highest cloud and cannot resolve multi-layer clouds. Because the VAS FOV resolution is coarse (14 km for this work), very small element clouds are difficult to detect. Also, because the weighting functions for the VAS channels are broad, there is an inherent lack of vertical resolution in the measurements. Nonetheless, reliable cloud statistics can be calculated with appropriate application of the technique.

Since October 1985, the VAS instrument on board GOES-6 has been programmed to gather sounding data over the United States at least twice daily (near 1200 GMT and 0000 GMT) and as often as four times daily (near 00, 0600, 1200, and 1800 GMT). The CO_2 technique has been applied to these data routinely. In this study, radiances for three FOVs were averaged for cloud height and amount determinations (representing an area of 14 by 42 km at the satellite subpoint) at roughly 100 km spacing. Surface observations were used to adjust the global forecast temperature and moisture fields. No adjustments for topography were made. Transmittances were determined from line by line calculations with the spectral response functions for the appropriate VAS channels.

3. VALIDATION

Quantitative comparisons are shown in Fig. 2. The CO_2 (or infrared window where necessary for low clouds) cloud top pressures are shown with the determinations from radiosondes. Cloud-top pressures are estimated from 1200 or 0000 GMT radiosonde temperature and dew point temperature profiles by noting where the dew point temperature profile becomes much drier as it emerges from the cloud and hence indicates cloud-top pressure. Since the profile analysis is not always definitive, a reliable radiosonde cloud height determination is not always available, especially in cirrus clouds. VAS observations were usually within 30 minutes of the raobs and were gathered over a three month period. The range of VAS cloud top pressures is from the four FOVs nearest to the radiosonde location. The VAS
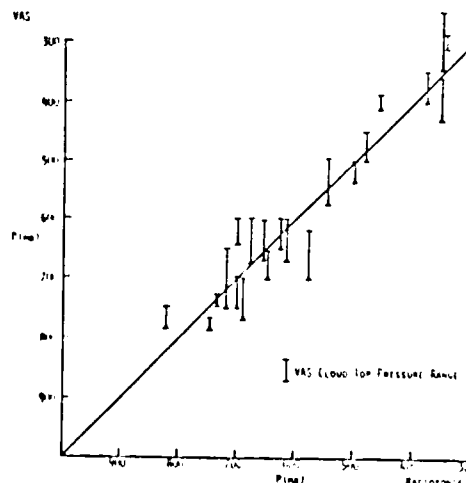

Fig. 2. VAS versus radiosonde cloud top pressures observed during winter 1985-86. RMS difference is 40 mb.

cloud top pressures compare extremely well with the radiosonde determinations; they are within 40 mb rms of each other. It should be noted that most of the height determinations below 600 mb are infrared window calculations. Validation of the cirrus heights will be accomplished with lidar determinations in future work.

4.   EXAMPLE STATISTICS

Cloud cover is a highly variable phenomenon which depends heavily on the storm tracks and other weather conditions. Detailed statistics of the November 1985 cloud summary for two cities in the midwestern United States (shown in Table 1) provide an example of how cloud cover can vary over short distances. Madison, Wisconsin and Chicago, Illinois are separated by approximately 150 km. The statistics of the satellite cloud observations for local noon (1800 GMT) are given for ten intervals of cloud top altitude and for five intervals of effective cloud amount or emissivity. The left column gives the frequency of cloud reports by altitude regardless of the cloud amount/emissivity. The next five columns show the distribution of cloud reports for five intervals of cloud amount or emissivity. The low cloud amount/emissivities (center columns) indicate cirrus clouds which were partially transmitting infrared radiation, while the right column summarizes the reports of opaque clouds that did not transmit upwelling radiation. The sum of the five right columns should account for all of the cloud reports (100%).

Both cities experienced many days of deep opaque cloud cover. This is evident by the high frequency of reports from 400 to 200 mb in the left column. Clear sky conditions were indicated by the 1000 mb reports. Chicago had 29% clear reports, while Madison only had 12%. The frequency of cirrus cloud reports that partially transmitted upwelling infrared radiation (emissivities less than .8) were also higher in Madison (27% summed over columns 2 through 5) compared to Chicago (16%). The thicker opaque cloud cover (right column) was also higher at 61% in Madison compared to 54% in Chicago. These differences reflect the fact that the position of the polar front and cyclone tracks were north of Chicago during the month.

5.   GEOGRAPHICAL COVERAGE

Statistical results for the entire United States plus coastal oceans for 13 months (October 1985 to October 86) are shown in Table 2 (coverage includes 27° to 51°N latitude and 55° to 157°W longitude). Cloud height determinations were made near 1800 GMT using the VAS radiances (the statistics reflect over 984,000 determinations). The most immediate finding is that 26% of the area was covered with thin or cirrus clouds. Approximately 45% of the United States was covered with thick opaque clouds and truly clear sky conditions occurred about 29% of the time. The cloud top pressures were distributed with 10% above 300 mb, 21% between 300 and 500 mb, 40% between 500 and 900 mb, and 29% at the surface (clear sky conditions). The thin clouds were mostly above 500 mb.

The geographical distribution of cloudy, cirrus and clear sky conditions for the year of October 1985 thru October 1986, is summarized in

TABLE 1.   Cloud Statistics for Madison, Wisconsin 42°N 90°W November 1985. 483 Observations in a 2°x2° box over 19 days from 1500 to 1800 GMT.

Level(mb)	Cloud Emissivity				
	0.0-0.2	0.2-0.4	0.4-0.6	0.6-0.8	0.8-1.0
100-199	0%	0%	0%	0%	0%
200-299	0	1	2	2	6
300-399	0	2	3	4	13
400-499	0	3	3	2	12
500-599	0	1	1	1	6
600-699	0	0	1	1	11
700-799	0	0	0	0	9
800-899	0	0	0	0	3
900-999	0	0	0	0	1
1000-1099	12	0	0	0	0
Total	12%	7%	10%	10%	61%

12% Clear   27% Cirrus   61% Cloudy

Cloud Statistics for Chicago, Illinois 42°N 88°W November 1985. 408 Observations in a 2°x2° box over 19 days from 1500 to 1800 GMT.

Level(mb)	Cloud Emissivity				
	0.0-0.2	0.2-0.4	0.4-0.6	0.6-0.8	0.8-1.0
100-199	0%	0%	0%	0%	0%
200-299	0	1	1	0	16
300-399	0	1	2	1	11
400-499	0	1	3	1	4
500-599	1	1	1	1	5
600-699	0	0	0	1	9
700-799	1	0	0	0	8
800-899	0	0	0	0	1
900-999	0	0	0	0	0
1000-1099	29	0	0	0	0
Total	31%	4%	7%	4%	54%

29% Clear   17% Cirrus   54% Cloudy

TABLE 2.   Cloud Statistics for United States, 27° to 51°N and 55° to 157°W for October 1985 thru October 1986 near 1800 GMT.

Level(mb)	Cloud Emissivity				
	0.0-0.2	0.2-0.4	0.4-0.6	0.6-0.95	0.95-1.0
100-199	0%	0%	0%	0%	0%
200-299	2	2	2	2	2
300-399	1	3	2	3	3
400-499	1	2	2	2	3
500-599	0	0	1	1	3
600-699	0	0	0	0	6
700-799	0	0	0	0	13
800-899	0	0	0	0	10
900-999	0	0	0	0	5
1000-1099	27	0	0	0	0
Total	31%	7%	7%	8%	45%

29% Clear   26% Cirrus   45% Cloudy

Fig. 3. All reports inside 2° latitude by 2° longitude boxes for each day at 1800 GMT were averaged together to produce the cloud statistics. Cloudy indicates all reports with cloud amounts/ emissivities greater than 0.95 in Fig. 3a. Cloud reports with cloud amounts/ emissivities less than 0.95 were summarized as cirrus in Fig. 3b, and clear sky reports are summarized in Fig. 3c. A large change in cloud cover with latitude is apparent. The states of Arizona and New Mexico in the central southern United States has the lowest frequency of cloudy conditions and the highest frequency of clear conditions. The frequency of clear reports reinforces the descriptor "Sun Belt" associated with southern states bordering Mexico. Transmissive cirrus clouds (Fig. 3b) were found at all locations in frequencies of 10 to 30%. The highest occurrences were in the northwestern mountain states of Utah, Colorado, and Wyoming. An increase in cirrus reports with latitude also is apparent.

6.   CONCLUSIONS

        This is a preliminary report of an ongoing study of cloud cover. Definitive conclusions on cloud cover statistics must wait until more years of data are compiled. However, these statistics for one year show results which have been reasonably anticipated. The most obvious finding of this study is the high incidence of thin cirrus clouds. Cirrus clouds have been given little attention in the past because they do not yield precipitation or damaging weather. But they do have a large impact on the radiative balance of the earth. Thin cirrus allow solar heating yet at the same time trap upwelling terrestrial infrared radiation. Our cloud statistics indicate that thin cirrus (cloud amount/ emissivities less than 0.95) occur 15 to 40% of the time over the United States. Thus, they are very numerous and must have a large effect on the heat balance of the earth.
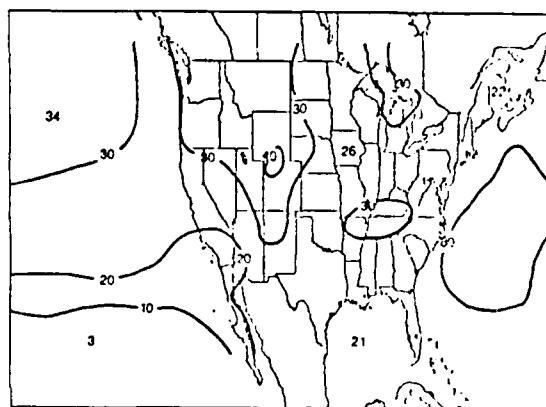
7.   REFERENCES

Menzel, W. P., W. L. Smith, and T. R. Stewart, 1983: Improved cloud motion wind vector and altitude assignment using VAS. J. Clim. Appl. Meteor. 22, 377-384.
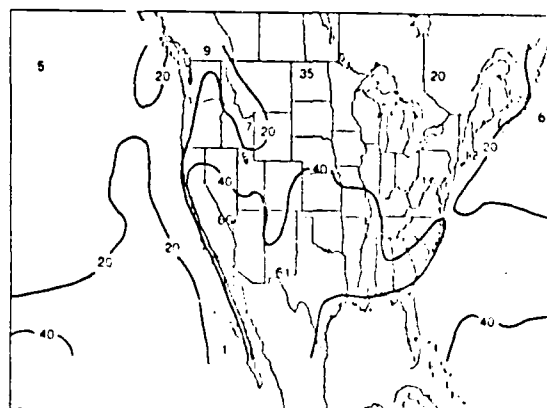
8.   ACKNOWLEDGMENTS
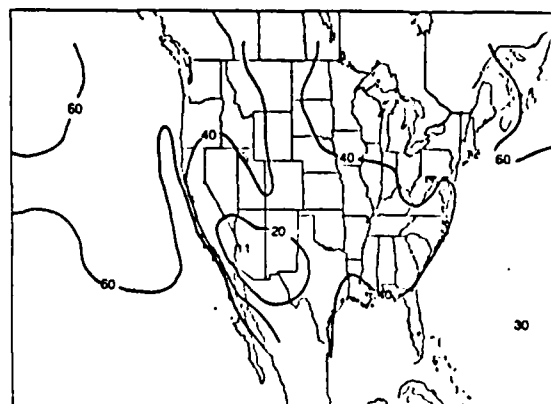
A Probability of Opaque Cloud Cover (%)

B Probability of Cirrus Clouds (%)

C Probability of Clear Sky (%)

Fig. 3. Geographic distribution of VAS determinations of cloudy (a), cirrus (b), and clear (c) sky conditions for October 1985 thru October 1986.

APPENDIX B

Cloud cover statistics using VAS

D. P. Wylie and W. P. Menzel[1]

Space Science and Engineering Center, NOAA/NESDIS Advanced Satellite Products Project[1]
1225 West Dayton Street, Madison, Wisconsin 53706

ABSTRACT

Statistics of cloud characteristics over North America have been calculated for the past two years. The frequency of cloud cover with the associated heights and infrared attenuation were charted using the CO_2 channel radiometric data from the geostationary VISSR Atmospheric Sounder (VAS). Cloud top pressures were determined from the ratio of VAS CO_2 channel radiances in a radiative transfer equation formulation. Cloud emissivities were then calculated from infrared window channel observations. CO_2 techniques derived height and emissivity assignments have been found to be reliable in all cloud types, including thin cirrus clouds where other techniques have been inconsistent. Observations since 1985 revealed that 25% to 35% of the United States was covered with thin clouds (radiative attenuation was less than 95%), 45% was covered with thick opaque clouds, and 20% to 30% had clear sky conditions. Geographical distribution of cloud cover shows a latitudinal dependence mainly over the Pacific Ocean. Moderate seasonal and diurnal changes were also found.

1. INTRODUCTION

The frequency of cirrus clouds usually has been underestimated in cloud population studies. Satellite methods of analyzing cloud cover often mistake cirrus clouds for lower level clouds or completely miss them, because their infrared brightness temperatures are warmer than the temperature associated with their true altitudes. Thin cirrus are especially hard to identify on visible satellite images because they reflect little solar radiation and appear as dark or broken cloud fields. With the multispectral infrared sensor on the GOES-VAS satellite, the identification of most cirrus is now possible.

A technique for deriving cloud top altitudes from the VAS infrared sensor was developed by Menzel (1983).[1] It is also applicable to the polar orbiting High-resolution Infrared Radiometer Sounder (HIRS). The technique takes advantage of infrared channels with partial CO_2 absorption where the different channels are sensitive to different levels in the atmosphere. Thus, clouds appear on each channel in proportion to their level in the atmosphere. Low clouds will not appear at all on the high level channels, while high clouds appear on all channels. By modelling the upwelling infrared radiation from the earth atmosphere system in several VAS channels simultaneously, it is possible to infer the cloud top height independence of radiative transmissivity of the cloud. This gives the CO_2 technique the ability to distinguish thin cirrus clouds that would normally be missed by other techniques due to the transmission of terrestrial radiation through the cirrus.

The CO_2 technique has been installed on the Man computer Interactive Data Access System (McIDAS) at the University of Wisconsin-Madison. It has been run operationally using the GOES-VAS imagery starting in October 1985. Statistics on cloud cover and especially cirrus cloud cover are being gathered for the continental United States and its bordering oceans. This paper describes the techniques and some of the first results of this program.

2. TECHNIQUE DESCRIPTION

The VAS radiometer detects infrared radiation in 12 spectral bands that lie between 3.9 and 15 microns at 7 or 14 km resolution in addition to visible reflections at 1 km resolution. The 15 micron CO_2 band channels provide a good sensitivity to the temperature of relatively cold regions of the atmosphere. A demonstration of the vertical resolution of the three relevant CO_2 channels is given by the temperature profile weighting functions shown in Fig. 1. Each curve in the figure shows the sensitivity of the radiance observed in the spectral interval of the indicated channel to local variations in atmospheric temperature. As may be seen, only clouds above the 350 mb level will have strong contributions to the radiance to space observed by the 14.2 micron band (VAS channel 3), while the 14.0 micron band (VAS channel 4) senses down to 700 mb and the 13.3 micron band (VAS channel 5) senses down near the surface of the earth.

To assign a cloud top pressure to a given cloud element, the ratio of the deviations in cloud produced radiances, $I(v)$, and the corresponding clear air radiances, $I_{cl}(v)$, for two spectral channels of frequency v_1 and v_2 viewing the same field-of-view is written as
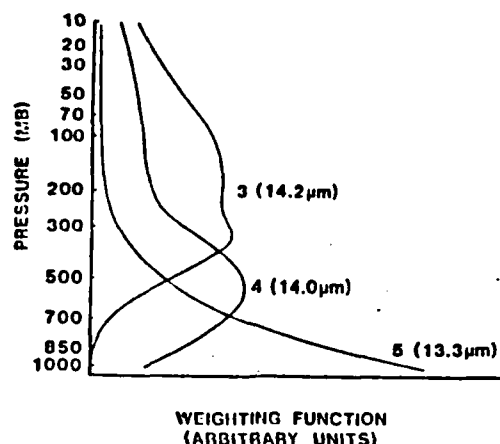
Figure 1. The temperature profile weighting function of radiance to space as a function of emitting level for the VAS CO_2 spectral bands centered at 14.2, 14.0, and 13.3 microns.

$$\frac{I(\nu_1) - I_{c1}(\nu_1)}{I(\nu_2) - I_{c1}(\nu_2)} = \frac{\epsilon_1 \int_{P_s}^{P_c} \tau(\nu_1,p) \dfrac{dB[\nu_1, T(p)]}{dp} dp}{\epsilon_2 \int_{P_s}^{P_c} \tau(\nu_2,p) \dfrac{dB[\nu_2, T(p)]}{dp} dp} . \tag{1}$$

In this equation, ϵ is the cloud emissivity, P_s the surface pressure, P_c the cloud pressure, $\tau(\nu,p)$ the fractional transmittance of radiation of frequency ν emitted from the atmospheric pressure level (p) arriving at the top of the atmosphere (p = 0), and $B[\nu,T(p)]$ is the Planck radiance of frequency ν for temperature $T(p)$. If the frequencies are close enough together, then $\epsilon_1 = \epsilon_2$, and one has an expression by which the pressure of the cloud within the field-of-view (FOV) can be specified. The left side of equation (1) is determined from the VAS observed radiances and clear air radiances provided from spatial analyses of VAS clear-sky radiance observations. The right side of equation (1) is calculated from a temperature profile and the profiles of atmospheric transmittance for the spectral channels as a function of P_c, the cloud top pressure (discrete values at ~50 mb intervals spanning 10000 to 100 mb are used). In this study, global forecast temperature and moisture fields from the National Meteorological Center (NMC) are used. The optimum cloud top pressure is determined when the absolute difference |right (ν_1, ν_2) - left (ν_1, ν_2, P_c)| is a minimum.

Once a cloud height has been determined, an effective cloud amount (also referred to as effective emissivity in this paper) can be evaluated from the infrared window channel data using the relation

$$\epsilon = \frac{I(w) - I_{c1}(w)}{B[w, T(P_c)] - I_{c1}(w)} . \tag{2}$$

Here N is the fractional cloud cover within the FOV, Nϵ the effective cloud amount, w represents the window channel frequency, and $B[w, T(P_c)]$ is the opaque cloud radiance.

Using the ratios of radiances of the three CO_2 spectral channels, three separate cloud top pressures can be determined (14.2/14.0, 14.0/13.3, and 14.2/13.3). If (I - I$_{c1}$) is within the noise response of the instrument ($\sim$1 mW m^{-2} - sr^{-1} - cm^{-1}), the resulting P_c is rejected. Using the infrared window and the three cloud top pressures, three effective cloud amount determinations are made. As described by Menzel (1983), the most representative cloud height and amount are those that best satisfy the radiative transfer equation for the three CO_2 channels.

If no ratio of radiances can be reliably calculated because (I - I$_{c1}$) is within the instrument noise level, then a cloud top pressure is calculated directly from the VAS observed 11.2 micron infrared-window channel brightness temperature and the temperature profile. In this way, all clouds are assigned a cloud top pressure either by CO_2 or infrared-window calculations.

The CO_2 technique is independent of the fractional cloud cover; heights and effective cloud amounts can be determined for partially cloudy FOVs. However, the CO_2 technique sees only the highest cloud and cannot resolve multi-layer clouds. Because the VAS FOV

resolution is coarse (14 km for this work), very small element clouds are difficult to detect. Also, because the weighting functions for the VAS channels are broad, there is an inherent lack of vertical resolution in the measurements. Nonetheless, reliable cloud statistics can be calculated with appropriate application of the technique.

Since October 1985, the VAS instrument on board GOES-East has been programmed to gather sounding data over the United States at least twice daily (near 1200 GMT and 000 GMT) and as often as four times daily (near 600, 1200, 1800, and 0000 GMT). The CO_2 technique has been applied to these data routinely. In this study, radiances for three FOVs were averaged for cloud height and amount determinations (representing an area of 14 by 42 km at the satellite subpoint) at roughly 100 km spacing. Surface observations were used to adjust the global forecast temperature and moisture fields. No adjustments for topography were made. Transmittances were determined from line-by-line calculations with the spectral response functions for the appropriate VAS channels.

3. VALIDATION

Quantitative comparisons are shown in Figure 2. The CO_2 (or infrared window where necessary for low clouds) cloud top pressures are shown with the determinations from radiosondes. Cloud-top pressures are estimated from 1200 or 0000 GMT radiosonde temperature and dew point temperature profiles by noting where the dew point temperature profile becomes much drier as it emerges from the cloud and hence indicates cloud-top pressure. Since the profile analysis is not always definitive, a reliable radiosonde cloud height determination is not always available, especially in cirrus clouds. VAS observations were usually within 30 minutes of the raobs and were gathered over a three month period. The range of VAS cloud top pressures is from the four FOVs nearest to the radiosonde location. The VAS cloud top pressures compare extremely well with the radiosonde determinations; they are within 40 mb rms of each other. It should be noted that most of the height determinations below 600 mb are infrared window calculations. Validation of the cirrus heights has been started by comparing with lidar determinations.
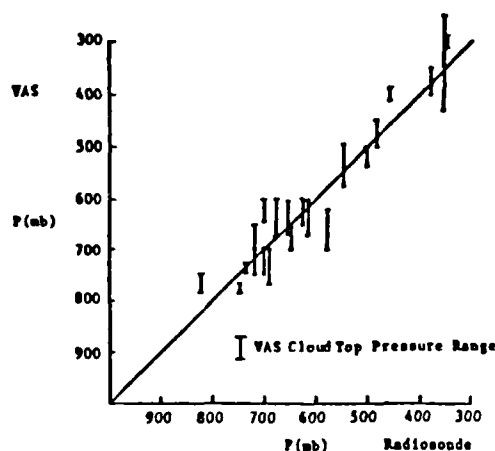

Figure 2. VAS versus radiosonde cloud top pressures observed during winter 1985-86. RMS differences is 40 mb.

4. MEAN STATISTICS

Cloud cover is a highly variable phenomenon which depends heavily on the storm tracks and other weather conditions. A statistical summary of all the cloud observations made from October 1985 through October 1987 are shown in Table 1. They cover the area from 27° to 51°N latitude and 55° to 150°W longitude. Over 2.7 million observations were collected. The cloud top pressure determinations were subdivided into ten vertical levels from 100 mb to 1000 mb in each row of Table 1. High clouds above 300 mb comprised 11% of the observations. 42% were between 300 mb and 800 mb. Low clouds below 800 mb were found 17% of the time. Clear sky conditions, labelled as 1000 mb, were found 30% of the time.

The effective cloud emissivities were subdivided into five intervals shown in each column of Table 1. The right column contains the opaque or near opaque cloud observations. We consider effective emissivity observations greater than 0.95 to be opaque clouds since the cloud top height derived from equation (1) is very close to the height derived from the window channel by itself. The other four columns separate the cloud height reports by effective emissivities ranging from the thin low emissivity clouds on the left to the thick high emissivity clouds on the right.

Table 1. Cloud Statistics for the United States
27° to 51°N and 55° to 150°W for October 1985 through October 1987

Level (mb)	Effective Emissivity				
	0.0-0.2	0.2-0.4	0.4-0.6	0.6-0.95	0.95-1.0
100-199	0	0	0	0	0
200-299	2	3	2	2	2
300-399	1	3	3	3	3
400-499	0	1	2	2	2
500-599	0	0	1	1	2
600-699	0	0	0	0	6
700-799	0	0	0	0	12
800-899	0	0	0	0	1?
900-999	0	0	0	0	5
1000 (clear)	30	0	0	0	0
	33 %	7 %	8 %	8 %	44 %
	30% Clear		26% Cirrus		44% Cloudy

Cirrus clouds are defined as observations with effective emissivities less than 0.95. 26% of our observations fell into this category. They were found from 200 to 600 mb. Clouds opaque to infrared radiation with effective emissivities greater than 0.95 (right column) were found 44% of the time. The remaining observations, 1000 mb (clear sky), were found 30% of the time. Thus, 70% of the satellite observations over North America for the past two years found clouds.

5. GEOGRAPHICAL COVERAGE

The geographical distributions of cloudy, cirrus and clear sky conditions from October 1985 through October 1987 are summarized in Figure 3. All reports inside 2° latitude by 2° longitude boxes were averaged together to produce the cloud statistics. The opaque cloud cover panel (Figure 3A) shows the probability of finding cloud cover with effective emissivity >0.95. Cloud reports with effective emissivities <0.95 were called cirrus clouds (probabilities are shown in Figure 3B). The probability of clear sky conditions (no detectable cloud) are shown in Figure 3C. Opaque cloud cover shows large geographical changes between the desert states of Arizona and New Mexico and the rest of the country. The clear sky probabilities reinforce the descriptor "sun belt" associated with the southern states of the U.S. Transmissive cirrus clouds were found in all locations, more frequently in the northwestern mountain states (Utah, Colorado, and Wyoming) and less frequently over the subtropical Pacific Ocean.

6. SEASONAL CHANGES

December, January and February observations were averaged for one winter. June, July and August observations were averaged for two summers. The results are shown in Table 2.

Fewer clouds were found in the summer than in the winter. Opaque clouds comprised 50% in the winter and dropped to 43% in the summer. Non-opaque cirrus were found 31% of the time in the winter while they were found only 26% of the time in the summer. Clear sky observations increased from 19% in the winter to 31% in the summer.

Table 2. Winter to Summer Seasonal Changes in Mean Cloud Cover
for 27°-51°N, 55°-150°W

	Winter	Summer
Cirrus clouds	31 %	26 %
Opaque clouds	50 %	43 %
Clear skies	19 %	31 %

The mean height of non-opaque cirrus observations also changed between the winter and summer seasons. The mean height of all non-opaque cirrus observations is shown in Figure 4A. The cirrus cloud tops appear to be lowest in the Rocky Mountains where an average height of 400 mb was found (this could change if topography were taken into account in the algorithm). Higher cirrus cloud top averages were found east of the Rockies (340 mb) and over the oceans (320 mb).

These height averages were lower in the winter than in the summer. Generally, 50 to 100 mb change occurred in the average height over most of the continental United States (see Figure 4B). The largest changes were in the Ohio Valley and the smallest changes were in the Pacific northwestern states.
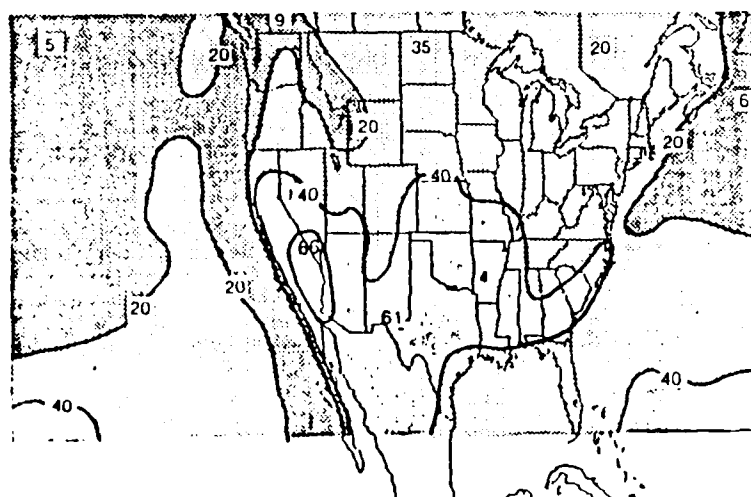
7. DIURNAL CHANGES

Moderate diurnal changes were found in the cloud data from the past two years (see Table 3). Opaque cloud cover over the study area changed from a maximum of 45% at 18:00 GMT to a minimum of 37% at 06:00 GMT. Non-opaque cirrus had smaller changes on the average. They
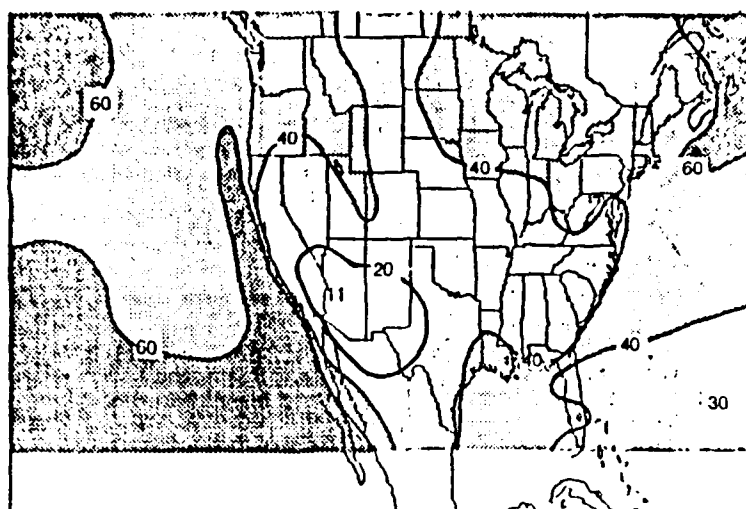
Probability of Opaque Cloud Cover (%)
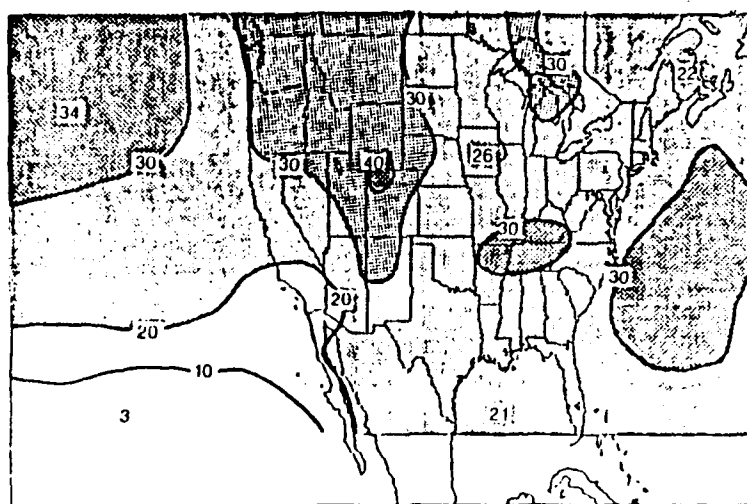
Probability of Cirrus Clouds (%)

Probability of Clear Sky (%)

Figure 3. The geographical distributions of (A) cloudy, (B) cirrus, and (C) clear sky conditions from October 1985 through October 1987.

AVERAGE HEIGHT OF CIRRUS (mb)

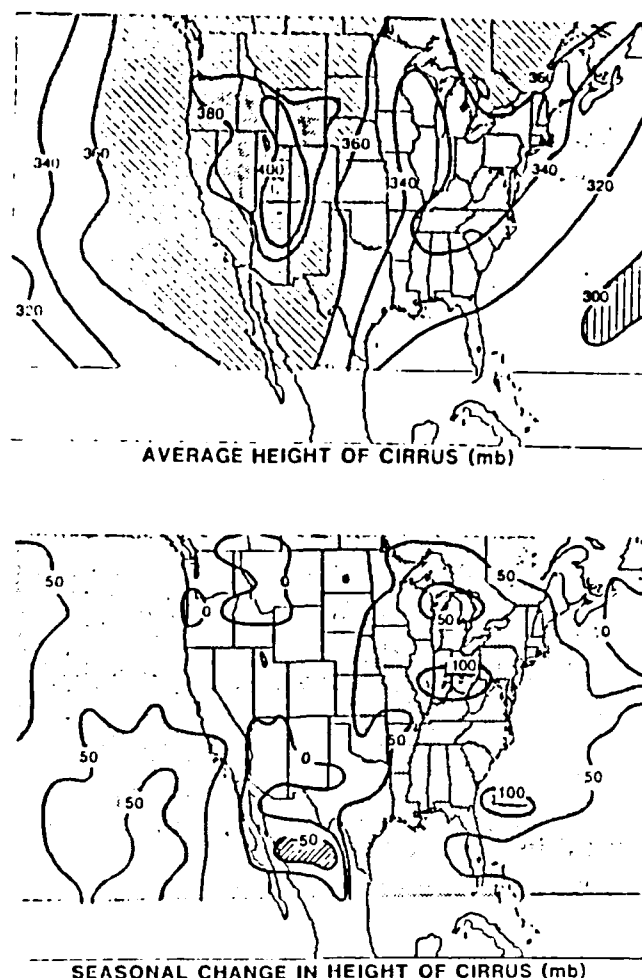**SEASONAL CHANGE IN HEIGHT OF CIRRUS (mb)**

Figure 4. (A) The average heights of the cirrus observations from October 1985 through October 1987. (B) The seasonal change in the heights of the cirrus, winter minus summer.

Table 3. Average Frequency of Cloud Observations for Four Time Periods Each Day

GMT	Cirrus Clouds	Opaque Clouds	Clear Sky
00	28 %	38 %	34 %
06	24	37	39
12	23	40	37
18	24	45	31

comprised 23 to 24% of the data for all times sampled , except at 00:00 GMT when 28% were found. clear sky observations had diurnal fluctuations similar to the opaque clouds changing from 31% at 18:00 GMT to 39% at 06:00 GMT. The largest diurnal changes were found during the summer season.

Geographically, the largest diurnal changes in transmissive cirrus observations occurred along the Gulf coastal states and in the Rocky Mountains (see Figure 5). In the Gulf coast and Colorado where cirrus cloud observations increased over the day, the opaque cloud observations decreased.

8. DISCUSSION AND CONCLUSIONS

This is a preliminary report of an ongoing study of cloud cover. Definitive conclusions on cloud cover statistics must wait until more years of data and more analyses are compiled. However, some interesting trends are emerging. The most obvious finding is the height incidence of transmissive cirrus clouds. Cirrus clouds have been given little attention in the past because they do not yield precipitation or damaging weather, but they have a large impact on atmospheric radiation.
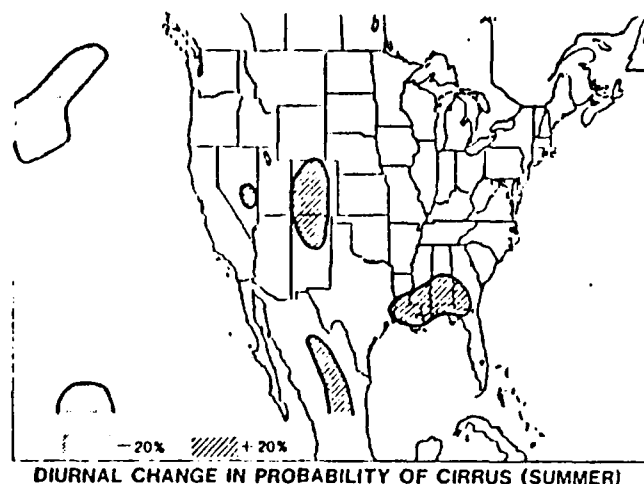
DIURNAL CHANGE IN PROBABILITY OF CIRRUS (SUMMER)

Figure 5.   Geographical distribution of the diurnal change in the probability of cirrus observations (p.m. minus a.m.) for summer.

These cloud statistics for October 1985 through October 1987 indicate that transmissive cirrus occur 25 to 35% of the time over the continental United States.   Small seasonal and diurnal changes in the frequency of cirrus clouds (about 5%) were not strongly connected with those of opaque clouds (about 8%).   This suggests that cirrus can be related to large scale synoptic patterns and are not always directly related to other cloud types.

9.   ACKNOWLEDGMENTS

The authors gratefully acknowledge the efforts of William Smith, Jr. and Peter Grimm who performed most of the data processing presented here.

10.   REFERENCES

1.   Menzel, W. P., W. L. Smith, and T. R. Stewart, 1983:   Improved cloud motion wind vector and altitude assignment using VAS.   J. Clim. and Applied Meteor., 22, 377-384.

Lidar Observations of Cirrus Cloud Parameters

Edwin W. Eloranta and Christian J. Grund

University of Wisconsin, Department of Meteorology
1225 W. Dayton St., Madison, Wisconsin 53706

Abstract

Cirrus cloud observations obtained with the University of Wisconsin High Spectral
Resolution Lidar and High Performance Nd:Yag lidar are presented. These include accurate
determination of the optical depths, backscatter phase functions, three-dimensional spatial
structure and internal wind fields.

1. INTRODUCTION

Cirrus clouds exert an important influence on the earth's radiation balance by
reflecting incoming solar radiation and trapping outgoing terrestrial radiation. Crystal
fallout from these clouds can seed underlying supercooled water clouds producing
precipitation. The influence of these clouds can profoundly effect a wide range of remote
sensors which attempt to look either up through the cloud at objects above the atmosphere,
or down from space at objects below the clouds. Scattering and absorption in the cloud
attenuates radiation from the target. Thermal radiation from the cloud and scattering of
ambient radiation provides increased background noise. Image contrast and the divergence
of transmitted optical beams can be adversely affected by the multiple scattering effects
of intervening cirrus clouds. Despite the importance of cirrus cloud effects they are our
least studied and most poorly understood common cloud form. Many basic questions remain
unanswered: we have only rudimentary forecast capabilities, we suspect that subvisible
clouds which may have important optical effects occur frequently, we know little about
cloud geometry, less about statistics of cloud free lines of sight and very little about
the optical properties of these clouds.

The difficulty of making measurements at cirrus altitudes has hampered
observations. Recent improvements in both active and passive remote sensors along with a
growing realization of the importance of these clouds has sparked new interest in this
research topic. This paper presents the preliminary results of one type of observation.

2. LIDAR EQUIPMENT

The University of Wisconsin operates two lidar systems with unique capabilities;
one which can make unambiguous remote measurements of optical extinction and backscatter
cross sections, and a second system which can acquire high spatial resolution, three-
dimensional pictures of atmosphere structure.

The High Spectral Resolution Lidar (HSRL) uses the Doppler broadening of signals
scattered from air molecules to distinguish molecular scattering from aerosol scattering.
Since the molecular backscatter cross section can be calculated from an atmospheric density
profile, the molecular component of the lidar return can be used as a calibration target
which is available everywhere in the scanned volume. Backscatter measured from this known
target then allows direct calculation of the optical extinction and the backscatter cross
section. While the HSRL was designed primarily for the characterization of boundary layer
aerosol scattering, we have adapted the system to the demanding task of cirrus
measurements.

The molecular scattering component of lidar return, which provides the HSRL
calibration, becomes difficult to measure inside the cirrus cloud. This occurs because
cirrus clouds have typical altitudes of up to 15 km producing four deleterious effects:
1) the signal is reduced by the additional range to the target, 2) the reduction in air
density decreases the molecular scattering cross section, 3) the lower temperature reduces
the spectral width of the Doppler-broadened molecular scattering making it more difficult
to separate from the unbroadened aerosol component, and 4) the backscatter cross section
of the cloud is typically very much larger than the molecular cross section, thus requiring
very accurate inversion of the lidar signals to separate the molecular scattering from the
cloud scattering.

The UW Nd:Yag lidar has been designed to rapidly scan large atmospheric volumes in
order to provide three-dimensional maps of aerosol structure. This lidar has a large aper-

ture (0.5m), rapid angular scanning capability (25 deg/sec), high average power (25 Watts), fast pulse repetition rate (30 Hz) and capability to store large quantities of data on a 2.6 gigabyte capacity write once optical disk system. These characteristics allow observation of cirrus cloud geometries with unprecedented spatial and temporal resolution.

3. OBSERVATION PROGRAM

The HSRL was operated for a total 124 hours during the FIRE field experiment during the period of October 15 to November 2, 1986, with periodic operations adding another 65 hours in the period between the experiment and Dec. 1, 1987. During all of these observations the HSRL was operated from a site on the campus of the University of Wisconsin in Madison, Wisconsin.

The Nd:Yag lidar was operated as a part of the NASA FIFE experiment from a site just south of Manhattan, Kansas during the period from June 30 to July 9, 1987. From September 23 to November 6, 197 this lidar was operated from a field site approximately 30 miles south of Madison, Wisconsin. During of these measurement campaigns the lidar was used for both the observation of cirrus clouds and the atmospheric boundary layer. In this paper we report on the cirrus cloud measurements.

4. MEASURED OPTICAL PROPERTIES

The HSRL has been used to measure optical depths, mean backscatter phase functions and backscatter cross section profiles in cirrus clouds. Results of these measurements will be presented in this paper. Figure 1 provides a typical example of the backscatter cross section profile measured in an optically thin cirrus cloud. Table 1 summarizes optical characteristics thus far established for cirrus clouds observed as part of the FIRE experiment.
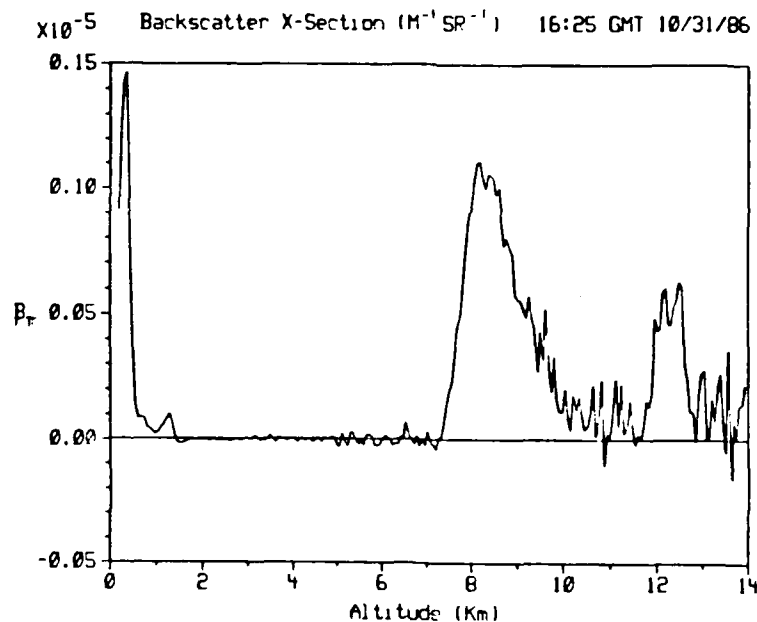

Fig. 1 Autumn "warm sector" cirrus backscatter cross section profile. The two layer structure is often observed in this type of formation.

Table 1: HSRL Measured Cirrus Cloud Optical Properties

Date	Time GMT	Altitude km	Optical Thickness	$\mathbb{P}_a(\tau)/4\pi$ Sr^{-1}	T C°
10/27/86	23:00	8.0	.03 ± .006	.028	-32.6
10/31/86	14:25	10.5	.11 ± .037	.030	-59.0
10/31/86	15:05	10.2	.09 ± .034	.032	-51.5
10/31/86	15:45	9.1	.12 ± .049	.024	-41.5
10/31/86	16:25	8.6	.07 ± .032	.039	-38.0
10/31/86	16:25	12.1	.02 ± .012	.023	-66.5
10/31/86	17:05	8.8	.05 ± .019	.034	-39.3
10/31/86	17:05	12.1	.01 ± .007	.045	-66.5

Observations of Cirrus backscatter phase functions made by Platt and Dilley show a marked dependence on cloud temperature. Our HSRL derived backscatter phase functions made over Madison, Wisconsin have thus far provided no evidence to support a cloud temperature dependence (see fig. 2).
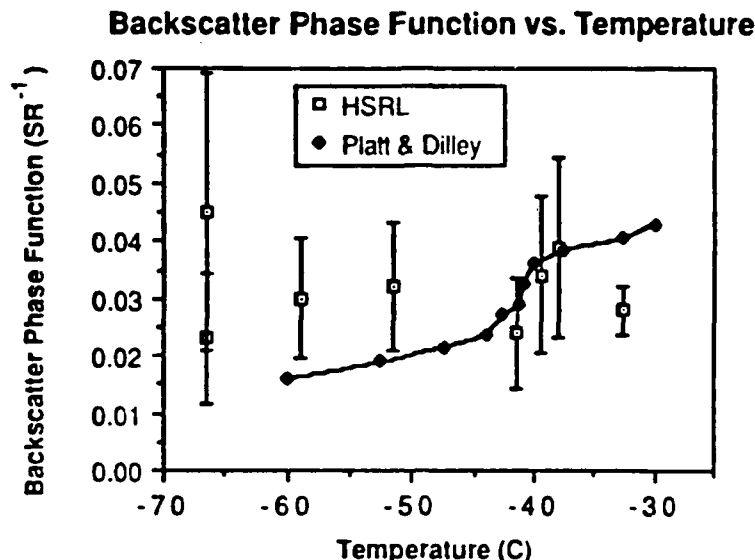
Backscatter Phase Function vs. Temperature

Fig. 2. The relationship of $P_a(\pi)/4\pi$ to temperature as reported by Platt & Dilley is compared with the independent HSRL measurements acquired during FIRE. A clear cut relationship between backscatter phase function and temperature is not apparent in the latter data set. Mie calculations show that an ensemble of liquid water spheres with an average size parameters of 500 could be expected to exhibit a backscatter phase function of .072 SR^{-1}.[2]

In our presentation, we will show examples of zenith angle specular backscatter from oriented ice crystals observed with the Nd:Yag system. In some cases the cone of enhanced backscatter exhibits 1/e full widths on the order of 1 degree, indicating crystals with large, horizontally-oriented flat faces. The presence of these sporadic, localized regions of specular reflection indicates the heterogeneous nature of ice crystal scattering properties within the cloud.

5. STRUCTURE OF CIRRUS CLOUDS

Preliminary examination of data acquired with the new UW Nd:Yag lidar has revealed organized cirrus cloud structure on scales ranging from our minimum resolution of 10 meters to the largest scales thus far observed of 50 km.

Casual 'eyeball' observations reveal that cirrus clouds frequently have complex three dimensional shapes. With conventional instruments it is difficult to map this structure. Even with a high repetition rate lidar, it is difficult to scan a sufficiently large volume in a short enough time to produce 3-D images which incorporate the large range of spatial scales represented by the clouds. The time available to generate an image is limited by the rapid motion and temporal evolution of the clouds.

Using the new UW Nd:Yag lidar we have begun studies of the 3-dimensional structure of cirrus clouds. In one type of observation, the lidar scans two orthogonal planes which cross at the zenith. One plane is approximately aligned with the mean motion of the cirrus and the other is perpendicular to the motion. This scan pattern allows construction of three dimensional pictures of cirrus clouds. the high repetition rate of this lidar allows a pair of scan planes to be completed in 30 seconds, with each plane showing a segment 8 km long at the cloud altitude. Height resolution of 15 meters is coupled with horizontal resolutions on the order of 20 meters. To observe larger spatial scales, a 60 km long section of cloud can be scanned in approximately 30 seconds, with only minor degradation in resolution. Space-time correlations can be used to provide the vertical profiles of the horizontal wind in the clouds as well as to investigate the scale sizes of the cloud structure. In the simplest 3-D display mode the two intersecting scan planes can be combined in perspective views and successive image pairs displayed to provide a time lapse movie of the cirrus structures. A display of this type will be included in our

presentation. At our laboratory we have also combined these images into true 3-D displays using cross polarized images for left and right eyes coupled with eyeglass filters. Additional 3-D depictions are planned using the cross-wind pictures and the measured wind speed to build 3-D volume filling images.

Observations of the cirrus clouds with our Nd:Yag lidar show considerable variability in the spatial structure of the clouds. Since this lidar is new, beginning operations in June of 1987, our data sample is rather small; it appears, however, that the cirrus clouds resulting from cumulonimbus formations tend to be different from clouds formed as a result of other processes. Many of the 'anvil cirrus' clouds are strongly layered with thin stable layers interspaced with thin apparently turbulent layers. The air mass cirrus developments observed during the Wisconsin fall often have much greater vertical extent with individual vertically developed structures embedded in the layer. These clouds often have thicknesses of several kilometers. These differences may be due to the fact that the vertical growth of cumulonimbus clouds is only halted by very stable air above the tropopause. The cirrus clouds are thus injected into a very stable regime often characterized by large wind shear; this stability coupled with the shear then produces the interspaced turbulent and stable layers. It seems likely that the air mass cirrus are produced in layers which are convectively unstable thus producing the greater vertical development.

6. ACKNOWLEDGMENTS

7. REFERENCES

1. Platt, C.M.R. and A.C. Dilley, "Determination of cirrus particle single-scattering phase function from lidar and solar radiometer data," App. Opt. 23, 380-386 (1984).

2. Shipley, S.T., "The measurement of rainfall by lidar", Ph.D. Thesis, University of Wisconsin, 187 pp. (1978).

OPTICAL PROPERTIES
BY HIGH SPECTRAL RESOLUTION
LIDAR

by
CHRISTIAN JOHN GRUND

A thesis submitted in partial fulfillment of the requirements for the degree of

Doctor of Philosophy
(Meteorology)
at the
UNIVERSITY OF WISCONSIN – MADISON

1987

II. Instrument Theory

This chapter has been included to offer the reader an introduction to the basic principles of lidar measurements, to define the quantities measured by lidar systems, and to establish the basis for HSRL measurements and calibration. Part A presents the basic operational lidar equations, while part B will cover the calibration theory. The reader with a minimal interest in

MEASUREMENT OF CIRRUS CLOUD OPTICAL PROPERTIES
BY HIGH SPECTRAL RESOLUTION LIDAR

by

CHRISTIAN JOHN GRUND

A thesis submitted in partial fulfillment of
the requirements for the degree of

Doctor of Philosophy
(Meteorology)

at the

UNIVERSITY OF WISCONSIN - MADISON

1987

MEASUREMENT OF CIRRUS CLOUD OPTICAL PROPERTIES BY
HIGH SPECTRAL RESOLUTION LIDAR

Christian John Grund

Under the supervision of Dr. Edwin Walter Eloranta and Professor James Adolf Weinman

Lidar backscatter signals are generated by scattering from both molecules and particles. The spectral distribution of light scattered by molecules is Doppler-broadened by rapid, thermally induced, molecular motions. Light scattered by aerosols and cirrus particles is essentia. / unshifted because of the relatively slow Brownian motion of particles. Using this difference, the High Spectral Resolution Lidar (HSRL) interferometrically separates particulate from molecular backscatter. By using the distribution of molecular scattering as a known target, the HSRL achieves unambiguous, calibrated measurements of atmospheric extinction, backscatter cross section, and backscatter phase function.

The HSRL was used during the FIRE IFO experiment (Oct.-Nov. 1986) to observe the optical properties and occurrence of cirrus clouds at Madison, Wisconsin. Significant improvements in instrument and calibration technique were accomplished which enabled the HSRL to perform optical property measurements at cirrus cloud altitudes. Successful eye-safe measurements were achieved during both day and night conditions using only 50 mW of average power at an 8 kHz repetition rate.

Range-time indicator displays of the lidar backscatter signal were generated which depict the height, occurrence and layer thickness of the clouds. Part of the data were analysed and calibrated backscatter cross section profiles were produced as well as time and range averaged values of extinction and backscatter phase function. Backscatter phase functions ranged from .027 - .045 sr^{-1}, with no apparent dependence on in-situ temperature.

Backscatter cross section profiles indicated that cirrus cloud-top structures often diminish slowly with height. Theoretical calculations were made which demonstrated that clouds of significant total optical thickness exhibiting realistic extinction profiles which diminished with height, could be "invisible" to nadir viewing space borne simple lidar systems

Approved by: _____ On _____

Approved by: _____ On _____

Acknowledgements

I would like to thank Dr. Edwin W. Eloranta and Professor James A. Weinman for serving as my advisors during the many years of research which have culminated in this thesis. Ed deserves special credit for his support and for the many shared hours spent in solving instrument and calibration difficulties. Ed's and Jim's comments, criticisms, and suggestions were instrumental in the clear and concise preparation of this work.

I would also like to thank Professors Fredrick Roesler, Pao Wang, Rolland Stull, and Charles Stearns for participating in my oral defense.

Special thanks go to Dan Forrest and Bob Chojancki for their expert assistance in software development. Dan's keen abilities at envisioning complicated logic flow are commendable and have often saved many hours of debugging time.

It is with special warmth that I thank Diane, my wife, for her loving support during these last trying months. Though she was six months pregnant during the FIRE operations, she would often rise at three AM and drive me to work so that I could have the HSRL up and running by dawn.

Dedicated to my family and especially to the memory of my father, Christian, and to my daughter Brigid Sky, whose birth spurred me on to complete this thesis.

Table of Contents

I. Introduction

Determination of the radiative effects cirrus clouds has become increasingly important to the meteorological community in recent years. Of paramount interest are the effects of cirrus on the local and planetary energy balance. Using a one dimensional radiative-convective model, Stephens and Webster (1981) have shown that a 4% change in cloudiness can have the same effect on surface temperature as a 1% change in the solar constant. This study indicated that the response of surface temperature to small changes in cloud properties is larger for optically thin clouds than for optically thick clouds since thick cloud properties tend to approach fixed radiative limits. High clouds were shown to act as net planetary warmers, with a linear dependence of equilibrium surface temperature on cloud cover. A cirrus cloud, with 20 gm/m^2 integrated equivalent liquid water path and complete sky coverage, was shown to enhance the surface temperature by 15^0 C over clear sky conditions. Clearly, measurements of the height, fractional cover, geographic distribution, optical extinction, and phase function (angular dependence of scattering) of cirrus are needed to provide realistic limits on these quantities so that the true effects of high clouds on global climate may be assessed.

Because cirrus clouds strongly effect upwelling and downwelling radiation in the atmosphere, the optical properties, height and probability of occurrence of these clouds are also of interest to satellite meteorologists. Since the infrared emissivity of cirrus changes more rapidly at lower than at higher cloud albedos (Stephens and Webster (1981)), visually thin (often

invisible) cirrus can have large and variable effects on the calibration of passive IR sounding measurements (Wylie and Menzel (1986)).

It has been shown that cloud radiative properties can have significant effects on the organization and maintenance of cirrus (Starr and Cox (1985)). Measurements of the variability and optical thickness of these clouds will aid in the modeling of such effects.

Space-borne simple lidar systems are currently planned which will operate in conjunction with co-located passive radiometers (Russell et.al. (1981)). Cloud height and optical thickness derived from the lidar profiles will be used to improve radiometric temperature retrievals by establishing the existence, height, and depth of optically thin clouds and providing the exact height of opaque clouds in the radiometer field of view (FOV). Fore-knowledge of cirrus scattering properties, extent and variability are needed to aid in the design and implementation of such systems.

Techniques have been developed for the remote assessment of liquid-water-cloud microphysical properties from lidar returns. Dubinsky et.al. (1985) demonstrate a linear relationship between mass concentration and optical extinction for droplet size parameters greater than 20. They also show that the mean droplet size may be derived from the slope of the extinction - mass concentration relationship for a given cloud. Measurement of the variability of cirrus optical properties will aid in the extension of these techniques to mixed-phase and, perhaps, ice clouds.

A glance at the Range-Time indicator (RTI) display in Fig. 1 will easily convince the reader of the variability of cirrus cloud cover. Cirrus layers may often be visually thin as evidenced by the complete penetration achieved by

Fig. 1

the lidar; yet, they may exceed 3 km in physical thickness.

Several methods are available for the estimation of cirrus cloud properties. Because cirrus clouds are composed of ensembles of mixed-phase and ice particles, and because ice crystal habits vary so widely, it is difficult to model the optical behavior of these clouds. Consequently, optical model calculations for only a few simple crystal shapes have been attempted (e.g. Wendling et.al. (1979), Liou (1980), Welch et.al. (1980)). The scattering cross section and scattering phase function of hexagonal ice crystals were considered in the first two studies. The latter study calculated the scattering properties of ice columns, bullets, and spheres.

Laboratory experiments have been carried out by attempting to recreate the low temperatures and pressures of the cirrus cloud environment (Sassen and Liou (1979)). While laboratory conditions allow a great degree of experimental control and repeatability, they are limited by the difficulty of replicating the complex dynamic effects of the natural environment on crystal interaction and formation. In addition, the determination of the phase function at angles near 180 degrees (backscatter phase function) is difficult because of instrument design considerations. It is for this reason that the measurements of Sassen and Liou were only carried out to 175 degrees. As can be seen from equation 1.1, the true value of the backscatter phase function has an important impact on lidar measurements since the observed backscatter from any range is proportional to this quantity.

$$N(R) = \frac{N_0 c}{2} \frac{A_r}{R^2} \beta(R) \frac{\mathbb{P}_\pi(R)}{4\pi} e^{-2\int_0^R \beta_\varepsilon(r')\, dr'}$$

(1.1)

Where:

R   range

N(R)   number of photons per unit time incident on the receiver from range R

N_0 number of photons transmitted in the laser pulse

c   speed of light

$\beta(R)$ total scattering cross section per unit volume (*aerosol + molecular)

$\mathbb{P}_\pi(R)/4\pi$ effective backscatter phase function at range R (due to aerosol and molecular scattering)

$\beta_\varepsilon(R)$ total extinction cross section per unit volume (aerosol + molecular)

A_r area of the receiver

The quantity $\beta(R) \cdot \mathbb{P}_\pi(R)/4\pi$ is known as the backscatter cross section and will be referred to often in this thesis.

Simple lidar techniques are capable of providing direct and accurate

---

* the term aerosol when used as a descriptor in HSRL equations means any particulate matter which contributes significantly to scattering of the transmitted laser beam and has a mass two or more orders of magnitude greater than that of air molecules. Thus, dust and cirrus cloud particles both fall into this category.

measurements of cloud fraction and altitude under most conditions. To make calibrated quantitative measurements of atmospheric extinction requires more sophisticated techniques. This may be easily seen by examining the lidar equation (eq. 1.1). The received energy from any range is a linear-function of the backscatter cross section at that range, multiplied by an exponential dependence on integrated extinction cross section.

One method of determining extinction from simple lidar returns assumes an analytic power law relationship between backscatter cross section and extinction. Such assumed relationships are questionable for spherical aerosols and they may be entirely unfounded for the faceted scatterers found in cirrus. The method then applies a Bernoulli solution to the lidar equation. The unknown constant in this solution is evaluated by assuming crude knowledge of the extinction at a far range (Klett (1981)). In addition, the technique is only stable in optically thick atmospheres.

Another technique makes use of lidar retrievals obtained at several elevation angles through horizontally stacked layers (Spinhirne et.al. (1980)). The method requires each layer to be horizontally homogeneous. The lidar equation is solved with the assumption that the information contained in each angle scan was produced by the same vertical profile of extinction. Clearly, the spatial and temporal variability of cirrus are sufficient to render this method inapplicable.

A technique called lidar tomography has been presented by Weinman (1984). This method is based on the angle scanning method but performed from a moving platform, thus avoiding the need for homogeneity. However, the technique would require aircraft operations for cirrus observations. In addition, the crystal alignments often found in ice clouds would present

different backscatter phase functions for fore and aft views of the same volumes which would prevent the determinations of unique extinction values.

An iterative approach presented by Eloranta and Forrest (1986), makes use of the additional information content in scans to determine the unknown coefficient in the Bernoulli solution. The Bernoulli solution is applied to each of many lidar profiles taken at different elevation angles through the lower atmosphere. A median profile of extinction vs. altitude is produced from the angle scans. Each initial guess profile is then corrected by the median value of its deviation from the median extinction vs. altitude profile. A new set of Bernoulli solutions is computed, and the process is repeated until an arbitrary convergence criterion is satisfied for the ensemble of shots. To date, this technique has been applied only to enhance detail in range height indicator (RHI) displays of lidar data. Although this algorithm provides stable, and convergent solutions to the lidar equation, it has not yet been shown that the solutions produced represent the correct extinction values. In addition, this algorithm is limited to solutions involving one or two fixed backscatter phase functions (Eloranta (1987)).

Platt and Diley (1984) have made measurements of cirrus extinction and backscatter phase function at a wavelength of 694 nm. Their method depends on calibration of the lidar returns by establishing a below-cloud range characterized by pure Rayleigh scattering. The integrated aerosol contribution to the extinction below this range is then removed by normalizing the backscatter profile with a cloud-free profile obtained just before or just after the cloud observation. With this calibrated backscatter

signal, the observed signal was corrected for attenuation to yield the true backscatter cross section on the assumption of a constant backscatter to extinction ratio (backscatter phase function). The backscatter phase function was estimated by extrapolation to an absorption of 1 from a plot of radiometer determined IR absorption against integrated backscatter cross section. Measurements made by this method have produced results for the backscatter phase function which vary systematically with temperature. Problems with this method include the establishment of an "aerosol free" region from which to calibrate the backscatter cross section, the assumption that the total aerosol content of the lower atmosphere remains constant from cloud to no-cloud observations, and the assumption of constant backscatter to extinction ratio. Additional uncertainties result from the need to correct for multiple scattering because of the wide FOV lidar used, and the accurate calibration of the radiometer, including estimation of thermal emissions from the surface which are subsequently scattered by the cloud. As the authors point out in a previous paper (Platt and Dilly 1981), plots of IR emittance against integrated backscatter did not always yield a well defined relationship, and these "anomalous" returns were removed from the data set. It was assumed that the anomalies were due to non-random orientations of ice crystals in the cloud.

In contrast, the HSRL (High Spectral Resolution Lidar) technique (Shipley et.al. (1983), Sroga et.al. (1983), Chapter II) is capable of separately determining the backscatter cross section, extinction and backscatter phase function. The only information required, in addition to the two spectral channel lidar return, is a profile of atmospheric molecular

density. Thus HSRL measurements of extinction and backscatter phase function in cirrus are unique and independent of questionable assumptions.

A major goal of this thesis is to outline the steps necessary to achieve a functional performance level of the HSRL instrumentation and calibration sufficient to demonstrate the feasibility of making backscatter cross section, extinction and backscatter phase function measurements in cirrus.

Another major goal of this thesis is to report selected HSRL remote measurements of backscatter cross section, extinction and backscatter phase function in visually thin cirrus, and to compare these unique direct measurements with the quantities derived by other methods.

An ancillary goal of this thesis is to provide a synoptic representation of the cirrus altitude and cloud cover variability for the period of October 15 - November 2, 1986 at Madison, Wisconsin. These measurements were made in conjunction with the FIRE IFO (F(irst) I(nternational Satellite Cloud Climatology Project) R(egional) E(xperiment) I(ntensive) F(ield) O(bservations)).

Consequently, the remainder of this thesis is divided into four major sections. For the readers convenience, and to make chapter III comprehensible, a review of the HSRL measurement technique and calibration theory is presented in Chapter II. Chapter III concerns the advancements in the HSRL instrumentation and calibration techniques necessary for the accomplishment of the stated measurement goals. Chapter IV contains the results of the measurements and explains the particular methods used to derive the reported quantities. The summary, and conclusions are presented in chapter V.

II. Instrument Theory

This chapter has been included to offer the reader an introduction to the basic principles of lidar measurements, to define the quantities measured by lidar systems, and to establish the basis for HSRL measurements and calibration. Part A presents the basic operational lidar equations, while part B will cover the calibration theory. The reader with a minimal interest in instrumentation and calibration techniques may skip part B of this chapter and chapter III. Part A of this chapter should provide sufficient background for the casual reader to interpret the results presented in chapter IV. However, the reader with a more pointed interest in instrumentation and calibration, if not already familiar with the HSRL, should read part B as an introduction to chapter III.

A. Measurement Theory

In monostatic lidar systems, a short burst of laser light is emitted towards the observed direction. As the beam propagates, it is subjected to scattering by molecules and aerosols (e.g. dust particles, cloud droplets, ice crystals). Some of that scattered energy is directed backwards towards the lidar receiver. Along the outward and return propagation paths, the signal is subject to extinction due to the scattering processes and to absorption.

In addition, it is also possible that photons may be multiply scattered into the receiver, and can thus contribute to the measured signal. Several conditions can encourage the multiple scattering process. Wide receiver FOV's or distant range observations can allow the the lidar to receive

photons from a large area which increases the probability of viewing additional scattering events. The probability of observing multiple scattering also increases with the optical thickness of the scattering media and with penetration depth. In addition, as scatterers become large compared to the wavelength of the lidar, the forward diffraction peak narrows, increasing the number of singly scattered photons which remain in the beam (see Weinman (1976)).

The signal measured at the receiver is actually the sum of the signals due to the above processes and the background skylight. The outlined mechanisms may be represented mathematically as:

$$N(R) = \frac{N_0 c}{2} \frac{A_r}{R^2} \left[\beta_a(R) \frac{P_a(\pi,R)}{4\pi} + \beta_m(R) \frac{P_m(\pi)}{4\pi} \right] e^{-2 \int_0^R \beta_\varepsilon(r') \, dr'} + M(R) + b$$

(2.2)

Where:

R	range
N(R)	number of photons incident on the receiver per unit time
N_0	Number of photons transmitted
c	speed of light
A_r	area of the telescope
$\beta_a(R)$	aerosol scattering cross section per unit volume
$P_a(\pi,R)/4\pi$	aerosol backscatter phase function
$\beta_m(R)$	molecular scattering cross section per unit

volume

$\mathbb{P}_m(\pi)/4\pi$ molecular backscatter phase function ($3/8\pi$)

$\beta_\varepsilon(R)$ total extinction cross section per unit volume

b   number of background photons incident on the receiver per unit time

M(R)   multiple scattering contribution incident on the receiver per unit time

For simplicity, the multiple scattering term M(R) will be discussed in appendix A and is also dropped for this discussion. A_r is a fixed parameter of the system and will assumed equal to 1. It will further be assumed that the background skylight b has been measured and subtracted from the received signal.

The spectral distribution of the light backscattered by molecules ($\beta_m(R){\cdot}\mathbb{P}_m(\pi)/4\pi$) differs significantly from that generated by particulate scattering ($\beta_a(R){\cdot}\mathbb{P}_a(R)/4\pi$). This is because the mean velocity of the relatively massive aerosols is two orders of magnitude smaller than that of air molecules. The spectral broadening due to molecular scattering in air is given by :

$$\frac{d\ln(N_m(\sigma))}{d\sigma} = \sqrt{\frac{\overline{m}c}{8\pi\sigma_0^2 kT}}\; e^{\left[-\overline{m}c^2(\sigma-\sigma_0)^2 / 8\sigma_0^2 kT\right]}$$

Fiocco and DiWolf (1968)   (2.3)

Where:

σ scattered light wavenumber

σ_0	incident light wavenumber
$N_m(\sigma)$	number of photons scattered by molecules
$\overline{m}$	mean molecular mass
c	speed of light
k	Boltzman constant
T	Kelvin temperature

The HSRL is capable of separating the photons backscattered by aerosols from those backscattered by molecules. A more detailed discussion of the method by which this separation is accomplished is presented in section B. Accordingly, two separate lidar equations may be written:

For molecular scattering:

$$N_m(R)\, R^2 = \frac{N_0\, c}{2}\, \beta_m(R)\, \frac{3}{8\pi}\, e^{-2\int_0^R \beta_\varepsilon(r')\, dr'}$$

$$(2.4)$$

Where $N_m(R)$ is the number of photons incident on the receiver per unit time which were scattered by air molecules from range R.

For aerosol scattering:

$$N_a(R)\, R^2 = \frac{N_0\, c}{2}\, \beta_a(R)\, \frac{P_a(\pi, R)}{4\pi}\, e^{-2\int_0^R \beta_\varepsilon(r')\, dr'}$$

$$(2.5)$$

Where $N_a(R)$ is the number of photons incident on the receiver per unit time from range R which were scattered by aerosols.

Because the scattering properties of molecules are well known, $\beta_m(R)$ may be calculated from a profile of temperature and pressure at range.

$$\beta_m(R) = C_{air} \, P_{atm}(R) \, / \, T(R)$$

(2.6)

Where:

P_{atm} pressure in hPa

T   Kelvin temperature

C_{air} = $4.483 \cdot 10^{-8}$ K hPa^{-1}m^{-1} at 510 nm

Thus, the signal from pure molecular scattering provides a calibrated target at every range and the only unknown quantity in equation 2.4 is the extinction cross section. By rearranging terms, the extinction may be found:

$$\beta_\epsilon(R) = -.5 \, [\, d(\ln(N_m(R)R^2))/dR - d(\ln(\beta_m(R)))/dR]$$

(2.7)

The first term in the square brackets is the slope of the natural log of the molecular return. The second term accounts for the signal loss or gain due to the change in the molecular density with range.

The backscatter cross section may be determined from the ratio of eq. 2.5 to eq. 2.4:

$$\beta_a(R) \, \frac{\mathbb{P}_a(\pi,R)}{4\pi} = \beta_m(R) \frac{3}{8\pi} \frac{N_a(R)}{N_m(R)}$$

(2.8)

If the particulate and gaseous absorption are negligible (i.e. the albedo for single scattering = 1), the aerosol scattering cross section may be determined as:

$$\beta_a = \beta_\varepsilon - \beta_m \qquad (2.9)$$

Equation 2.8 may now be solved for the backscatter phase function:

$$\frac{\mathbf{P}_a(\pi,R)}{4\pi} = \beta_m(R)\frac{3}{8\pi}\frac{N_a(R)}{\beta_a(R)\,N_m(R)}$$

$$(2.10)$$

B. Calibration Theory

As shown in eqs. 2.6-2.10, the separation of photons scattered by aerosols from those scattered by molecules is essential to the unique determination of the extinction and backscatter phase function. This section will consider the methods by which the lidar return spectrum is analysed to produce such separate returns.

Following the discussion in section A, the singly-scattered signal $S(R)$ received per unit time by a simple lidar may be represented as the sum of photons scattered by molecules, photons scattered by aerosols, and the background skylight:

$$S(R) = [\gamma_m(R)N_m(R) + \gamma_a(R)N_a(R) + b]\,\gamma_E$$

$$(2.11)$$

where γ_E represents the non-spectral and non-range dependent component of the system efficiency for the conversion of photons incident on the receiver to photons detected. It includes the photo-detector quantum efficiency, area of the receiver, loss of photons at optical surfaces, and other system calibration constants. The factors $\gamma_a(R)$ and $\gamma_m(R)$ relate the efficiency with which incident aerosol-scattered and molecular-scattered photons are respectively converted to signals wherever the system throughput varies wavelength or range. For simple lidar systems, $\gamma_a(R) = \gamma_m(R) = \gamma_0(R)$ where $\gamma_0(R)$ is the system overlap function.

The HSRL observes $S(R)$ in two different channels having differing spectral characteristics. One channel primarily measures the central region of the return spectrum which contains most of the aerosol backscatter and

the central portion of the Doppler-broadened molecular backscatter. The other channel measures the wings of the Doppler-broadened spectrum and a small amount of the central spectral region of S(R). The instrument was constructed using a multi-etalon spectrometer in the receiver and is described in detail in Shipley et.al. (1983); significant system changes are outlined in Grund (1984). Because the signals in each channel are different linear combinations of the aerosol scattered and molecular scattered photons, one may write:

$$S_m(R) = C_{am}(R) \, N_a(R) + C_{mm}(R) \, N_m(R) + b_m \qquad (2.12)$$

$$S_a(R) = C_{aa}(R) \, N_a(R) + C_{ma}(R) \, N_m(R) + b_a \qquad (2.13)$$

Where:

$S_m(R)$ number of counts measured in the molecular channel per unit time

$S_a(R)$ number of counts measured in the aerosol channel per unit time

$C_{am}(R)$ fraction aerosol scattered photons incident on the receiver which are subsequently detected in the molecular channel

$C_{mm}(R)$ fraction of molecular scattered photons incident on the receiver which are subsequently detected in the molecular channel

$C_{aa}(R)$ fraction of aerosol scattered photons incident on the receiver which are subsequently detected in the aerosol channel

$C_{ma}(R)$ fraction of molecular scattered photons incident on the receiver which are subsequently detected in the

aerosol channel

b_a, b_m background light measured per unit time in the

aerosol, molecular channel

In this representation, the factor γ_E and γ_a have been combined for the aerosol channel and are represented by the coefficients C_{aa} and C_{am}; γ_E and γ_m are combined for the molecular channel and are represented by coefficients C_{ma} and C_{mm}. It is further assumed at this point that an appropriate subtraction of the skylight contributions to eq.'s 2.12 and 2.13 has been performed. Solving these equations yields:

$$N_m(R) = (C_{aa}(R)S_m(R) - C_{am}(R)S_a(R)) / \delta(R) \qquad (2.14)$$

$$N_a(R) = (C_{mm}(R) S_a(R) - C_{ma}(R) S_m(R)) / \delta(R) \qquad (2.15)$$

Where:

$$\delta(R) = C_{aa}(R) C_{mm}(R) - C_{ma}(R) C_{am}(R)$$

The calibration coefficients are shown here with a range dependence because previous constructions of the HSRL have been subject to spectral bandpass changes with range. In addition, coefficients C_{ma} and C_{mm} have a weak dependence upon the temperature at range. The current system has undergone significant modifications which have removed the strong instrument-related calibration dependence on range. These changes will be discussed in chapter III.

At present, the coefficients C_{aa} and C_{am} are determined by directly observing diffuse and attenuated laser light through the receiver spectrometer. Since the light has not been Doppler-shifted by inelastic collisions, this is equivalent to observing pure aerosol scatter from the atmosphere. Thus, C_{aa} is the observed signal in the aerosol channel, and

C_{am} is the observed signal in the molecular channel.

The receiver is then swept across the observed laser spectrum to obtain the convolution of the receiver channel bandpasses with the transmitted laser spectrum. The observations of C_{aa} and C_{am} at each point in this convolution are equivalent to the values of these coefficients for different relative receiver-transmitter spectral tune positions. Thus, tuning drift may be estimated during HSRL operations by intermittently viewing the laser light directly with the receiver and determining the ratio of aerosol to molecular channel signals which most closely matches the same quantity observed in a recent calibration scan.

Coefficients $C_{mm}(R)$ and $C_{ma}(R)$ can now be calculated from the calibration scans. As equations 2.12 and 2.13 show, these coefficients are determined directly from the aerosol and molecular channel signals under conditions of pure molecular scattering. It is is not practical to generate this sort of scattering under operational conditions, so eq. 2.3 is used to predict the molecular spectral shape for the temperatures at range. $C_{mm}(R)$ and $C_{ma}(R)$ are then determined from the convolution of the normalized predicted molecular spectrum with the calibration scans from the molecular and aerosol channels, respectively. Account of the operational tuning drift can be made by choosing the C_{mm} and C_{ma} from the appropriate convolution offset for the best tune determined from the ratio matching method outlined above. Current practices for the determination of C_{ma} and C_{mm} will be discussed in greater detail in part B of chapter III.

Other instrument parameters which require calibration have been lumped together in the terms generically denoted $\gamma(R)$ in eq. 2.11. These terms include the conversion efficiency of the receiver, the degree to which

the receiver fully views the laser beam at range (overlap function), and any signal correlated instrument noise. Instrument noise which is uncorrelated with signals (e.g. photomultiplier tube dark count) may be treated as background signal and combined in term b of eq. 2.2.

In the HSRL, the conversion efficiency of the receiver is included in the calibration coefficients and is implicitly determined by the calibration method described. The overlap function is important only in the near range. For the current HSRL, complete overlap is achieved beyond a range of 2 km. The major cause of signal correlated noise in HSRL measurements has been photomultiplier afterpulsing (AP). AP is a process by which detection of a photon may produce some probability for the observation of an additional, time-delayed, signal pulse. AP is due to the backward acceleration of ions dislodged from the photomultiplier tube anode by the original photon signal. These ions eventually strike the photocathode and dislodge additional electrons which are subsequently accelerated by the dynode chain and measured at the anode as signal. In the past, it has been necessary to correct for the effects of AP in the HSRL data (Sroga (1983), Grund(1984)). The mathematical form of this correction is given by:

$$\gamma(R) = 1 - \int_{0}^{R} (S(r') - b) \ \Phi(R - r') \ dr'$$

$$(16)$$

Where $\Phi(R)$ is the photomultiplier afterpulse probability distribution.

Because the magnitude of $\gamma(R)$ depends on the sum of signals present from all previous ranges, this correction term can become large for some photomultipliers.

III. Adaptation of the HSRL to Cirrus Measurements

The University of Wisconsin HSRL instrumentation has passed through many stages of development since the first feasibility study by Shipley et. al. in 1975. The original instrumentation design was field tested in 1980. The results of these tests and the first successful attempts at instrument calibration are reported in Sroga et.al. (1983).

Analysis of the field test results revealed several instrument design flaws which produced large calibration uncertainties and made operations difficult. In view of these problems, it is to Dr. Sroga's credit that he was able to demonstrate the feasibility of the instrument design by showing significant relationships between HSRL measurements and boundary layer profiles. Error bars reported for this original data were based only on confidence of fit of a spectrometer model to an HSRL calibration scan since other error dependencies were unknown at that time. Sroga's data were acquired in a down looking mode from an aircraft platform flying at ~4 km altitude. The measurements were made within a range of 2 to 4 km from the HSRL. The reported measurements were averages over several hours of flight time. Average aerosol cross section and boundary-layer bulk average backscatter phase functions were presented.

In order to highlight the current capabilities of the HSRL, it is important to note that, in the down-looking mode, the molecular density increases with range. The molecular backscatter profile is used as a known calibration target, and, for upward pointing cirrus observations, this necessary target decreases with range. In addition, the signal is reduced by an additional

factor of ~10 due to the R^2 effect.

Analysis of the field test data results indicated the need for significant instrument improvements which would increase system reliability and decrease calibration uncertainty. Among these were a change to a higher power copper chloride laser, temperature stabilization of the multi-etalon receiver/transmitter system, conversion to a coaxial receiver/transmitter optical axis configuration, and correction for the full distribution of photomultiplier afterpulsing. These and other system modifications as well as boundary layer aerosol measurements were reported in Grund (1984) and Grund and Eloranta (1985). These measurements were taken along a fixed horizontal path, and produced time resolved results demonstrating the effects of changes in relative humidity on aerosol extinction and backscatter phase function. The measurement range terminated on a smoke stack at 4080 m. Operating in this manner decreased background light and allowed continuous checks on calibration from the stack reflection.

Because measurements of cirrus cloud optical parameters by HSRL technique are much more difficult than previously attempted measurements of boundary layer aerosols, several limitations of the of the first and second versions of the HSRL were evident.

1. Background count removal must be made with great accuracy since the ratio of signal to background is small at cirrus distances and because the background light is enhanced by cloud-scattered sunlight. Background light effects were lessened in previous measurements by viewing the atmospheric backscatter against the ground or a stack, or by operating at a

wavelength where the solar corona is highly absorbing.

2. Time delayed, signal correlated noise (i.e. photomultiplier tube afterpulsing) must be minimized since the noise injected by the relatively large cloud backscatter can easily mask the smaller molecular backscatter component from altitudes within and above the cloud.

3. For measurements in cirrus, calibration coefficient uncertainties needed to be decreased significantly for several reasons. Inaccuracies in the coefficients Caa and Cam can easily cause some of the relatively large cloud-related backscatter to appear in the separated molecular return, upsetting both signal intensity and slope determinations. Secondly, the first problem is aggravated by the small molecular densities (hence small molecular backscatter cross sections) at cirrus altitudes. In addition, the low temperatures at cirrus altitudes cause a narrowing of the Doppler width of the molecular spectrum which lessens the effective signal separation between the channels.

Accordingly, the achievement of the measurement goals presented in this thesis demanded instrument modifications and the development of several new calibration methods. Part A of this chapter will outline the instrument modifications while part B will consider the new calibration techniques.

In reviewing this chapter it is important that the reader keep in mind that the ability to make any measurement is not a simple function of the theoretical abilities of the instrument to make the observations. It is also intimately dependent on the accuracy with which the instrument may be

calibrated in terms of the quantities sought. Meaningful results associated with the latter dependency require good instrument design and operation practices. Such operations have been achieved with the HSRL only by a process of continuous critical analysis of atmospheric data and improvements to the instrument design and calibration technique based on the results of those data analyses.

In this chapter, frequent reference will be made to the theoretical principals and techniques outlined in chapter II. The reader is therefore advised to become thoroughly familiar with that material before proceeding.

A. Instrumentation

For the HSRL, the ability to measure extinction and backscatter phase function depends upon the accuracy with which the slope of the log of the separated molecular return is determined (see eq. 2.4). In addition, the accuracy of backscatter cross section and phase function measurements is related to the accuracy with which the ratio of the magnitudes of the aerosol and molecular signals can be determined (see eq. 2.10).

The molecular signal slope determinations may be severely degraded if:

1. The background light is not correctly removed from the signal, causing a range squared perturbation to appear imposed on the data.

2. Local observations of the transmitted spectrum do not represent the true spectral distribution of probe light at range. This effect precludes accurate determination of calibration coefficients C_{aa} and C_{am} at range causing an increase in the cross-talk between retrieved signals. Thus, molecular signal slopes will be perturbed in any region with strong particulate scattering, as in cirrus clouds.

3. A systematic range dependence of the calibration coefficients will have similar effects to those outlined in 2 except that the amount of cross-talk will vary with range.

4. Time delayed, signal correlated noise (afterpulsing) can easily mask the small molecular scattering signal at cirrus altitudes.

The approaches by which each of these problems has been addressed were often interrelated and will therefore be discussed together.

The HSRL makes estimates of the background light component of the lidar signal by counting photons received in each channel over a specified time following a specified delay from each laser firing. In order to reach cirrus altitudes it was necessary to modify the copper chloride laser to reduce the pulse repetition rate (PRR) from 10 kHz to less than 8 kHz. This change allowed sufficient time between laser pulses for the backscattered signal to decay and for background signal integration to take place. Another advantage of operation at the lower PRR has been increased thyratron lifetime and higher per pulse peak energies. Higher per pulse energies yield signal gains over background skylight and therefore improve measurement capabilities, particularly while observing cirrus.

The data system uses significantly different counting electronics for processing the range resolved signal from that used for determining the integrated background signal. It was discovered that there were systematic errors between background signals recorded in data bins and those recorded in the background counters. These differences were eliminated by improvements in the photon counting electronics, and by developing an empirical correction algorithm for the background counter signals. The empirical corrections were generated by observing ~30 million photons from a low level white light source, and determining the average ratio of data bin counts to background counter detected counts.

Local calibration of the HSRL was accomplished by scanning the receiver spectrometer across the transmitted laser spectrum in order to

determine the two-channel system spectral response. It was determined that the energy variations of the laser were not random as previously supposed. Thus, the overall shape of calibration scans were modulated by systematic laser energy variations leading to increased uncertainties in the knowledge of the calibration coefficients. Coefficients Caa and Cam (see eq.'s 2.12, 2.13) are respectively proportional to the aerosol and molecular channel amplitudes and are thus highly sensitive to the effects of energy variations.

To lessen the calibration uncertainties due to laser energy variations an energy monitor was integrated into the system and calibration scans were normalized by output laser energy. The effect of this normalization on a typical calibration scan is illustrated in Fig. 2. Energy normalized scans are represented by lines while unnormalized scans are plotted as symbols. The aerosol channel scans are plotted in circle and solid line, with the molecular scans plotted in diamond and dashed line. To aid in comparison, both sets of scans were normalized by the respective areas under the aerosol curves. Biases due to long term laser energy variations can be seen in the regions where the unnormalized points systematically over or under estimate the energy normalized values. This is most clearly evident in the more gently sloped molecular channel trace. Also note that the energy normalization removes much of the point scatter throughout both scans.

Because the spectral bandpass of etalons depends upon the angular distribution of the incident light, it was necessary for Sroga et.al. (1983) to generate a ray tracing model of the original HSRL optical configuration. This model predicted the range dependence of the calibration coefficients. Modification of the system from a paraxial conjugate aperture configuration to a coaxial receiver/transmitter construction reduced the magnitude of this
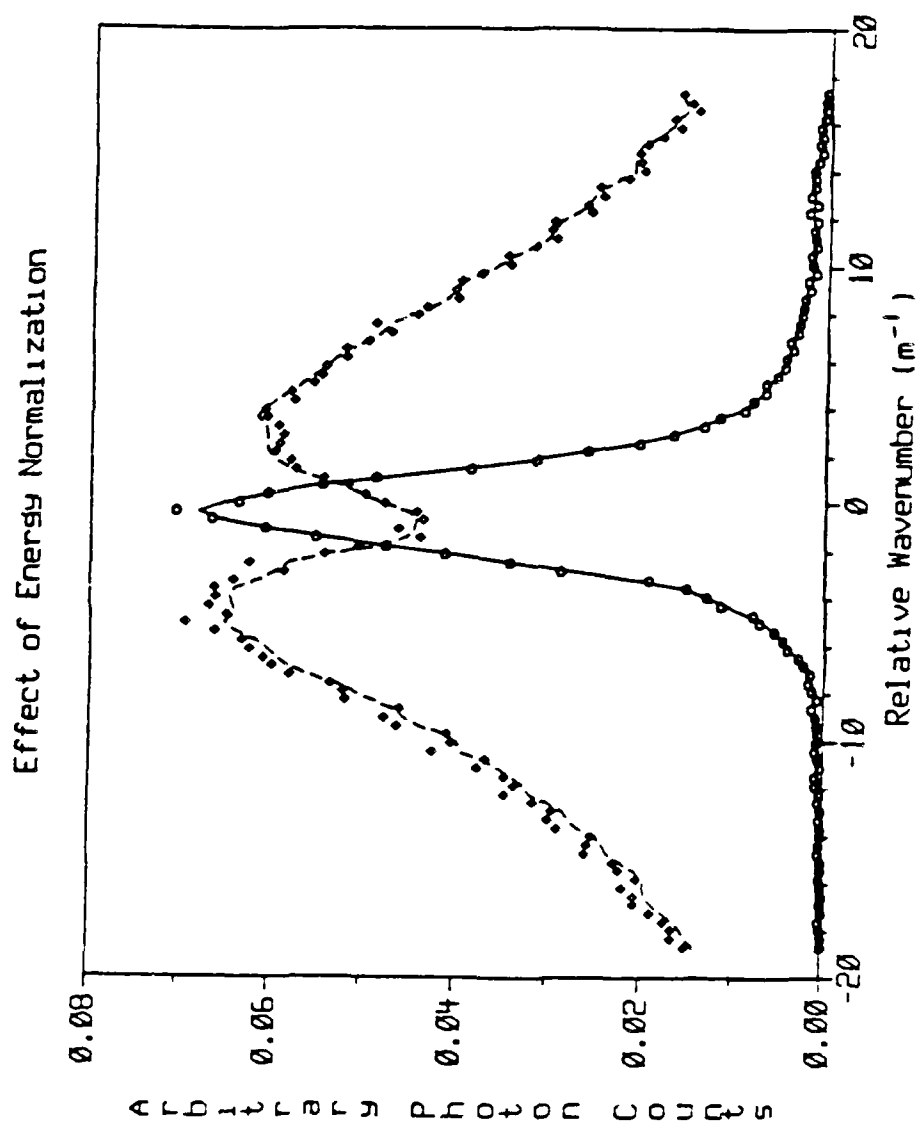
Fig. 2 By adding energy normalization (line plots), both point scatter and the effects of systematic laser energy drift are reduced in raw HSRL calibration scans (point plots). Solid line plots are for the aerosol channel while the molecular channel scan is plotted in dashed line

range dependent correction. However, as pointed out in Grund (1984) the loss of the conjugate aperture arrangement caused a new range dependence associated with uncertainties in the paraxiallity of the receiver and transmitter optical axes. The former problem is of little consequence to measurements at cirrus altitudes because at these ranges, the focal plane of the sensed volume closely approaches the input aperture of the receiver and the effect of telescope obstructions no longer affect the spatial distribution of light in the aperture. The angular misalignment effect still remains, however. In order to eliminate both of these instrument induced error sources, a ray position "scrambling" optical fiber was employed (see Fig. 3). The fiber was rigidly supported, coaxially aligned with the receiver optic axis, and had ends polished to 1 wave. The length of the fiber was 100 mm, with a core diameter equal to that of the input aperture (1.23 mm). The fiber had a numerical aperture of .66, was composed of F-2 glass and had a cladding diameter of 1.25 mm. The length was chosen so that rays entering the aperture from the smallest unobstructed diameter of the telescope primary must achieve at least two reflections from the fiber walls as they transit through the fiber. Thus, all rays from the telescope which impinge on the input aperture end of the fiber are preserved in angle relative to the optical axis, while the exit positions are effectively randomized. By this technique the position of any particular ray was randomized on each of the etalons, while the ensemble angular distribution was maintained. A strong dependence of the calibration coefficients on range was thereby eliminated.
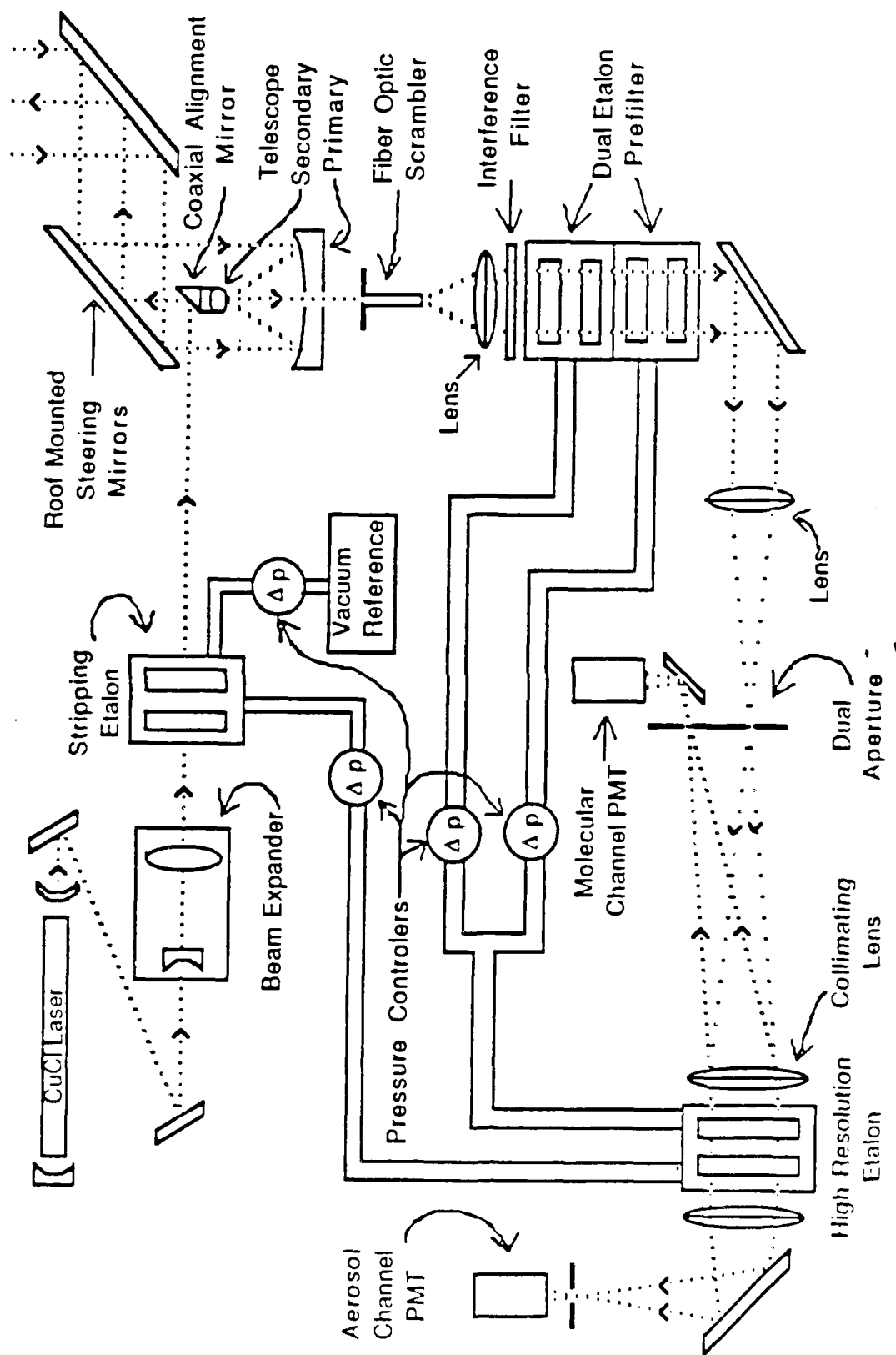
Fig. 3 HSRL Receiver/Transmitter

By observation of calibration scans from several hard targets at varying ranges (e.g. smoke stacks, water tanks, etc.), it was possible to compare the spectral response of the system at range with that observed locally, and with that predicted by the model of Sroga et.al (1983). In order to remove the effects of variability in extinction between the lidar and the target, the ratio of observed aerosol to molecular channel signals was utilized for comparison with a like ratio of signals locally observed. As can be seen in fig. 4, no range dependence was apparent between .42 and 7.14 km. This lack of range dependence illustrates the utility of the aperture scrambling technique.

Observed Calibration Range Dependence
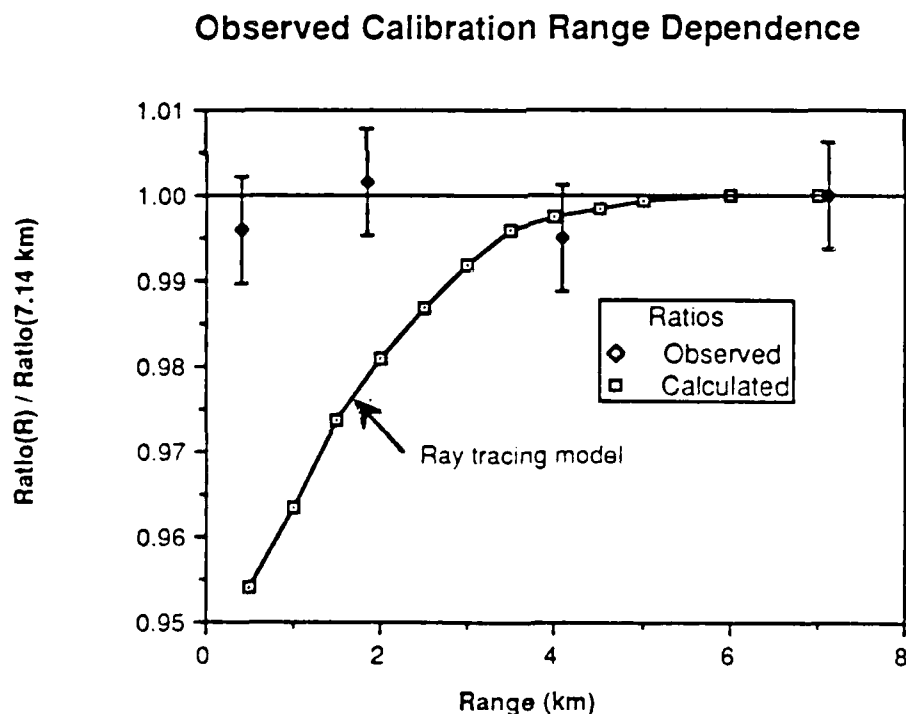
Fig. 4. This figure demonstrates the ability of the optical fiber scrambler to reduce the range dependence of the HSRL receiver spectral bandpass. The expected range dependence of the ratio C_{aa}/C_{am} was calculated using a ray tracing instrument model (Sroga et al. (1983)). The point observations of this ratio were

obtained by summing many minutes of data while viewing hard targets at the ranges indicated (e.g. water tanks, smoke stacks). C_{aa}/C_{am} is used in this comparison in order to remove the effects of extinction between the HSRL and the observed targets, and to cancel the non-spectral intensity-modulating effects of geometric overlap. The plotted values have been normalized to the appropriate ratio at 7.14 km to facilitate comparisons. Error bars on the measured ratios were determined from photon counting statistics.

The initial attempts at experimentally determinig the calibration coefficient range dependence by the above method revealed a systematic bias toward wider spectral bandpass in local observations with respect to those at range. The disconcerting systematic increase in the full width at half maximum (FWHM) of the local spectral observations with respect to the FWHM at any range was traced to contamination of the local scans by off-axis laser light and light generated with poor angular properties. Some of the contamination was inherently generated by the laser; part was caused by a secondary laser cavity created by feedback from the laser stripping etalon; and, an additional component was traced to unstripped laser light scattering into the receiver. The latter problem was solved by the addition of shielding to the receiver input area. The first two problems were solved by the inclusion of a spatial filter in the calibration light pathway. This spatial filter has an angular acceptance of 1 milliradian which is somewhat larger than the 320 microradian telescope FOV. This design for the spatial filter seemed adequate to provide a good coincidence between observed spectral widths locally and at range. Fig. 5 is a plot of the spatial filter aperture diameter vs. observed spectral FWHM for various aperture diameters. Note the flattening of the response at a diameter of about 100 micrometers which corresponds to an angular acceptance of 1 milliradian.

This figure shows that the angular distribution of the contamination light falls well outside the angular acceptance of the telescope (320 µR). The illustrated bimodal distribution demonstrates that the light contamination may be adequately removed by this technique.
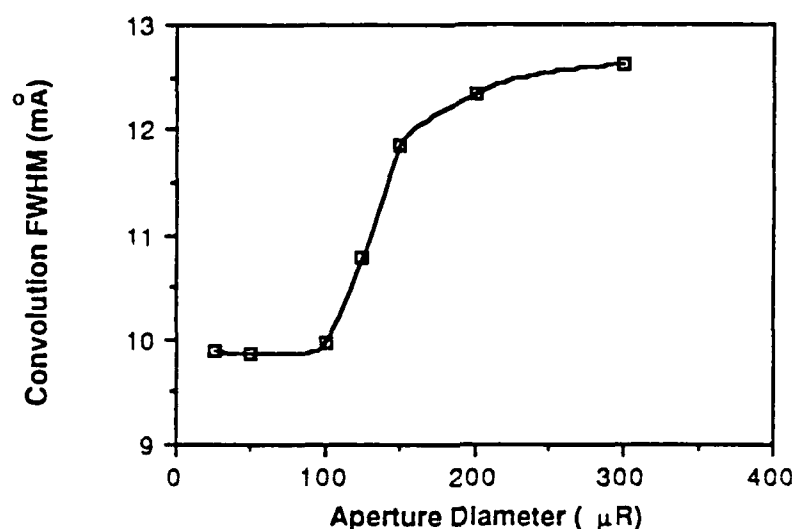
Spectral FWHM vs. Spatial Filter Aperture Dia.

Fig. 5   Spectral FWHM of the transmitted laser as viewed by the receiver spectrometer as a function of spatial filter aperture diameter. The spatial filter employed a 100 mm fl. lens.

A further improvement in local calibration accuracy was achieved by uniformly scattering the calibration light across the telescope FOV while the telescope was blocked to all other light. This configuration provides an identical pathway for calibration light and for backscattered light from the atmosphere, thus insuring similar optical axes and angular distribution for both input mechanisms. Systematic differences in the mean angle of the ray bundles from each source were thereby eliminated.

Photomultiplier tubes exhibit some probability of producing a time distribution of spurious photon counts following each true photon event. This

process is called afterpulsing (AP) and is a function of PMT construction and voltage divider acceleration potentials. The problem was recognized and corrected by Sroga et.al. (1983). Corrections were extended to a newly observed secondary afterpulse by Grund (1984). As pointed out in the latter study, the secondary distribution precluded background count assessment in the time beyond the last range observation and before the next laser pulse. This was because the secondary AP distribution from strong near-range signals appeared in this time period. The problem has been completely eliminated in the current system configuration by the inclusion of new, low-afterpulsing phototubes (EMI Gencom 9863B/100). A comparison of the old AP distribution with the performance of the current system is illustrated in Fig. 6. Without this system modification, measurements in cirrus would not have been possible as the relatively weak high-altitude signals would have been degraded by cumulative AP induced noise, and accurate background measurement would not have been possible because of AP contamination.

With a narrow FOV instrument, it is particularly difficult to make and maintain adjustment of the transmitted beam within the receiver FOV. Accordingly, a beam expansion telescope was added to the laser transmitter, thus lessening sensitivity to the natural drift of the laser optical axis and also lessening the sensitivity of the system to errors in the receiver/transmitter coaxiallity alignment. To facilitate the coaxial adjustment, a 5 inch aperture, high accuracy (10 µ radian) corner cube was used to retro-reflect the transmitted laser beam into the receiver telescope. The focused image of the laser was then observed in the spectrometer input aperture. The laser coaxiallity alignment mirror was adjusted until the image
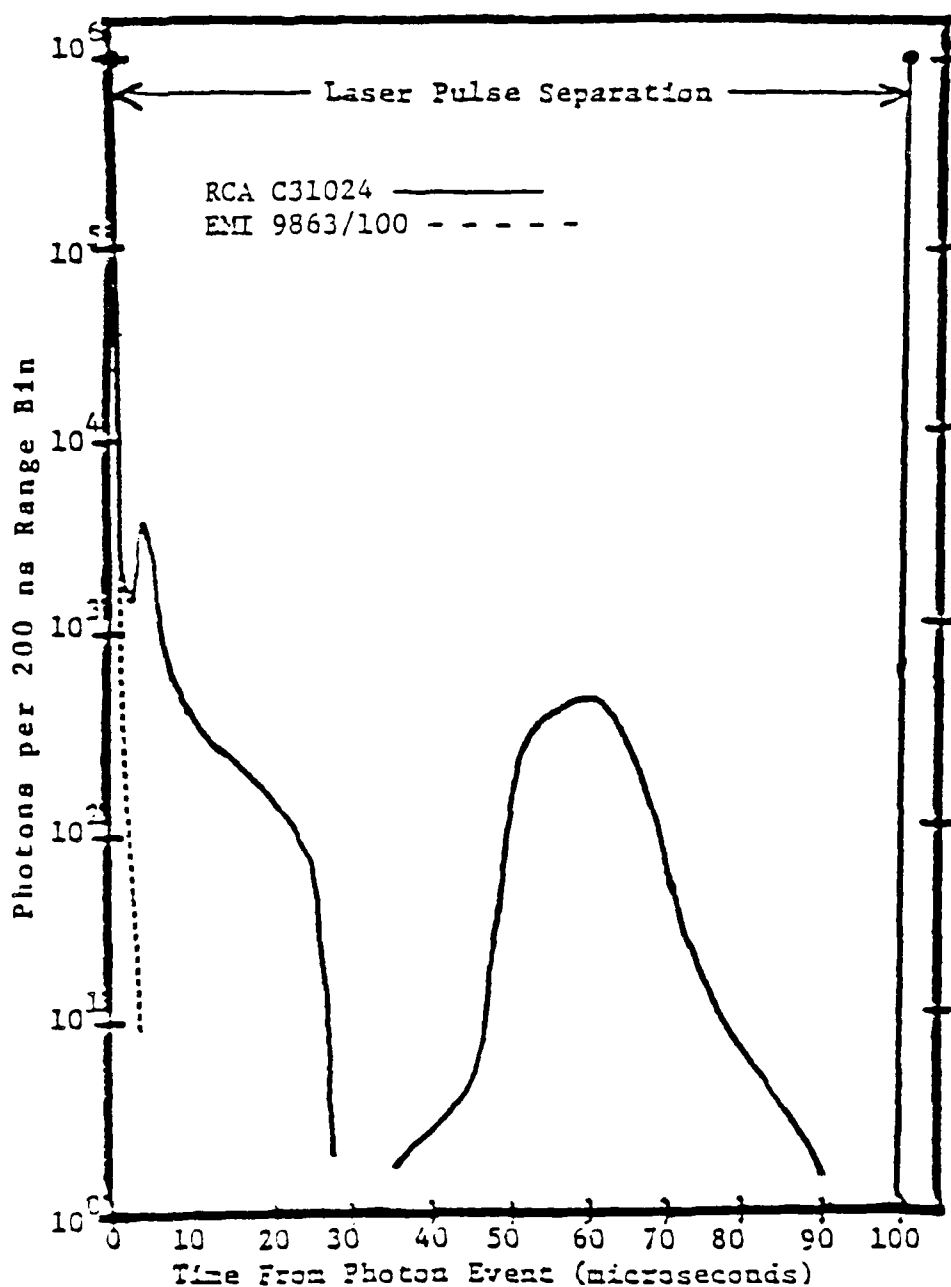
Fig. 6 Photomultiplier tube afterpulsing distribution for the currently used EMI 9863/100B tubes as compared with the formerly used RCA C31024 tubes. Note the comparatively small primary and lack of secondary AP in the EMI tube distributions. These traces were achieved by observing attenuated laser light with the HSRL receiver and data system. The photon rate was maintained at less than .05 photons per laser pulse to minimize potential overlap of photon events.

point of the laser was centered in the aperture. Thus a once difficult adjustment was accomplished routinely.

With the etalon pressure controller configuration reported in Grund (1984), it was noted that reference pressure stability was insufficient and that the control loop between the laser etalon and the high resolution (HR) etalon was too loose. Accordingly, a new pressure reference and sensor for the laser etalon were incorporated. The pressure control configuration was also changed so that the laser etalon pressure acted as a master reference to which the HR etalon pressure was slaved.

A simplified schematic of the current system configuration has been presented in Fig. 3, and a summary of system specifications is given in Table 3.1.

Table 3.1: System Parameters

HSRL Receiver:

Telescope:

Primary diameter	.35 m
Secondary diameter	.114 m
Focal length	3.85 m
F.O.V. (full width)	320 μR

Pre-filter: 50 mm diameter plates

Fiber optic Scrambler	100 mm X 1.23 mm dia
	.66 N.A., F-2 glass
Interference filter (FWHM)	1 nm at 510.6 nm
Etalon spacers (E_1, E_2)	1.003, .726 mm
Combined bandwidth (FWHM)	2.5 pm

High resolution etalon: 150 mm diameter plates

Etalon spacer	12.786 mm
Bandwidth (FWHM)	.6 pm

Photomultiplier tubes: EMI Gencom 9863B/100

HSRL Transmitter:

Laser: $CuCl_2$ (lasing on Cu lines at 510.6 nm and 578.2 nm)

Beam expansion factor	3
Transmitted beam diameter	30 mm
Transmitted power	50 mW at 510.6 nm
Bandwidth (stripped FWHM)	.4 pm
Pulse repetition rate	8 kHz
Pulse length	15 ns
Input power	4 kv , .5 A at 8 kHz

B. Calibration

In an attempt to meet the calibration accuracies required for measurements of cirrus, a critical examination was performed of the fit of the non-linear regression model of Sroga et.al. (1983) to the observed calibration scans. This study revealed certain systematic errors. The first type of error was the appearance of unmodeled excess light in the wings of the aerosol channel response. The second error appeared as an overestimate of the peak of the aerosol channel response, and a related underestimate of the center of the molecular response curve.

The first error was reduced by incorporating the functional form of the raw laser output spectrum into the model. The raw laser line has a FWHM of about 5 pm, and is composed of three hyperfine elements which greatly overlap (see Grund (1984)). The hyperfine structure caused perturbations in the observed spectrum with respect to that modeled by assuming a flat distribution for the laser.

After several improvements to the algorithms used to model the components of the spectrometer, errors of central misfit in the aerosol and molecular channel were actually worsened. Apparently, the remaining errors of fit were due to the unmodeled effects of etalon plate defects. Such defects are related to alignment and adjustment of optical components in addition to fixed flaws in the elements themselves. It was not expected that they should be either randomly distributed or fixed parameters of the system. Thus, modeling these flaws was considered inappropriate, and a new technique was sought to remove the effects of noise in the calibration scans.

Originally, the spectrometer model was developed to create reasonable

fits to very noisy calibration scans, and to allow modeling of the range dependence of the calibration coefficients. Since current scans are free of energy variations and appear to contain only statistical noise, a much simpler model based on purely statistical considerations could be employed. Since, in the current system, the first order range dependence of the calibration coefficients had been eliminated by the fiber optic scrambler, it was no longer necessary to predict the overlap effects on the calibration coefficients.

As a consequence of the problems with the non-linear model fit, and of the simplifications of system calibration response brought about by instrumentation changes, a new model was devised. The calibration fits were done by a more pliable and more computationally efficient spline approximation to the calibration scans. Coefficients Caa and Cam were taken directly from the value of the spline fits to the aerosol and molecular scans, respectively. Cma and Cmm were derived by a convolution of the expected molecular (Doppler-broadened) spectrum with the raw aerosol and molecular scans, respectively (see eq.'s 3.17, 3.18). Smoothing was performed by the convolution process in the case of the latter two coefficients. Since the temperatures at cirrus heights may vary widely, the expected molecular spectral broadening was calculated at height from an appropriate temperature profile. C_{ma} and C_{mm} were calculated from the laser spectrum as observed by the receiver:

$$C_{ma}(T,\sigma) = \int_{-\infty}^{+\infty} \frac{d \ln(N_m(\sigma'-\sigma_0))}{d\sigma} S_a(\sigma') \, d\sigma'$$

$$(3.17)$$

$$C_{mm}(T,\sigma) = \int\limits_{-\infty}^{+\infty} \frac{d\ln(N_m(\sigma'-\sigma_0))}{d\sigma} \, S_m(\sigma') \, d\sigma'$$

(3.18)

Where the first term in the integral is evaluated at temperature T according to equation 2.3 and S_a, S_m are the observed calibration scan signals in the aerosol and molecular channels, respectively.

In the past, a single set of calibration coefficients based on a single calibration scan had been used to invert bulk averaged data. The process involved determining a best guess of the average spectral center of transmitted light relative to the receiver spectrometer. This was accomplished by observing the average aerosol to molecular channel signal ratio for highly diffuse and attenuated laser light scattered into the receiver. Matching this ratio to the ratio of C_{aa} to C_{am}, predicted from the calibration scan, provided a good guess at the average receiver-transmitter mistune for the data sum. As stated in the introduction to this chapter, cirrus measurements require very accurate knowledge of the calibration coefficients. The previous method of calibration was not without problems in this respect. The method introduced a non-linear signal separation component into the bulk averaging scheme since tuning drifts over the averaging time caused shifts in the coefficients, hence changes in the distribution of photons between the aerosol and molecular channels. Fig. 7 shows the typical drift in the ratio of C_{aa} to C_{am} over a 3.3 hour period.

Because of the non-linear effects of this drift problem, and the need for

HSRL Uniform Aperture Illumination: 10/31/86 14:00 GMT
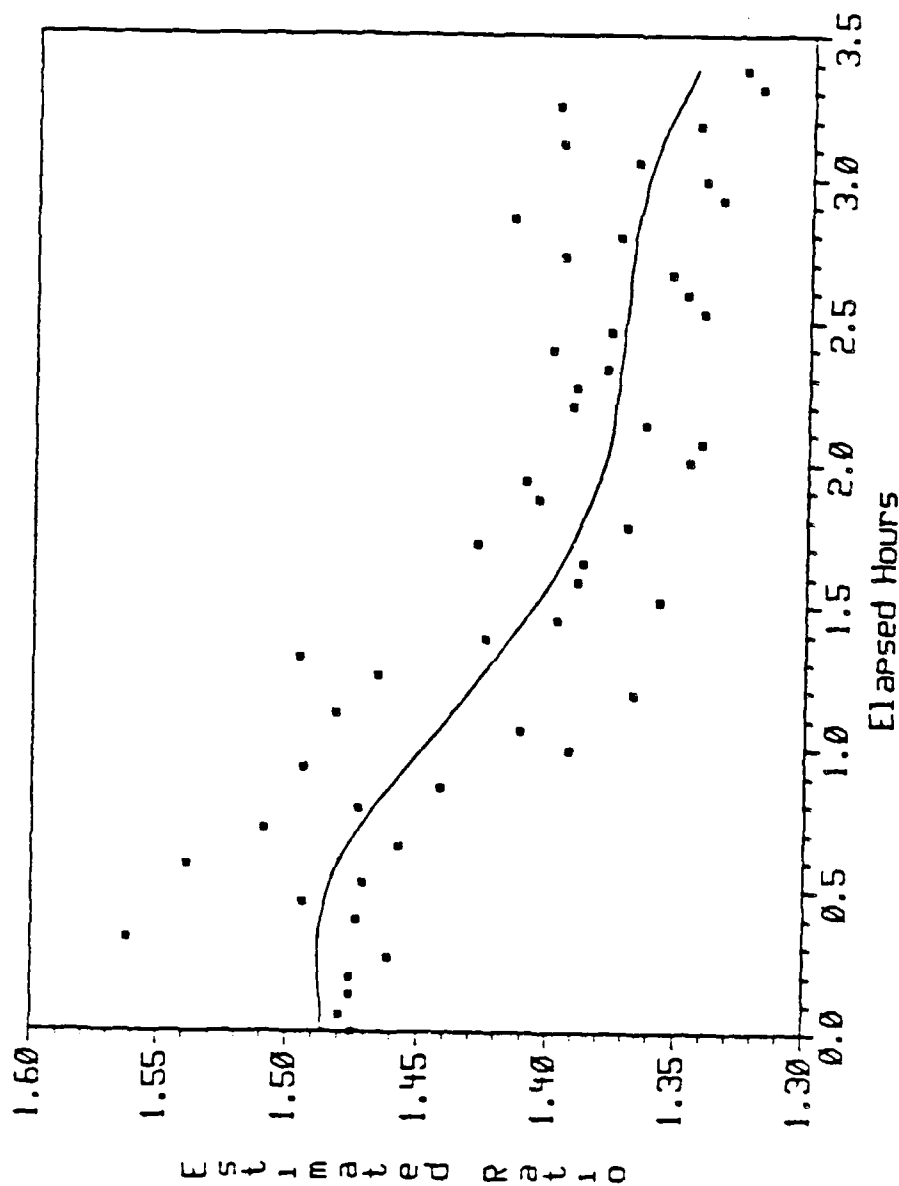
Fig 7. Record of the tuning ratio C_{aa} / C_{am} during data acquisition on 10/31/86. The measurements were obtained from the ratio of the observed aerosol to molecular channel signals while viewing diffuse and attenuated laser light with the HSRL receiver.

improved calibration coefficient estimates necessary for measurements in cirrus, a new algorithm for data inversion was developed. This algorithm made use of a calibration scan performed before and after each 2 - 10 hour data acquisition segment. A linear interpolation between these scans was performed for each lidar shot, and a new set of coefficients defined for that shot. Tuning drift was recorded at 3.5 minute intervals by interrupting data acquisition and measuring the ratio of aerosol to molecular channel signals while the receiver directly viewed diffuse and attenuated laser light. This drift record was used to determine the particular set of coefficients appropriate to each shot. A discussion of the fluctuations in the tuning ratio may be found in part D of this chapter. The solid line plotted in fig. 7 is a spline fit to tuning ratio drift observations for 10/31/86 and represents the actual values used in the inversion of that data as presented in the next chapter.

Thus, this scheme accounts for both the non-linear effects of transmitter-receiver drift, as well as total system bandpass and throughput changes. Implementation of this new calibration method was made possible by the computational efficiency of the spline fit model outlined above.

An example of the improvement achieved by employing this technique may be found in fig. 8. Shown in dashed line is a molecular scattering profile created by inverting the sum of raw data with a single set of average coefficients. The solid line is the same raw data set with the inversion performed on a shot by shot basis using interpolated coefficients before summing. In order to show the effectiveness of the technique more clearly, noise has been filtered from the profiles using a spline fit. The region between 8 and 11 km contains a cirrus cloud; thus, the apparent increase in
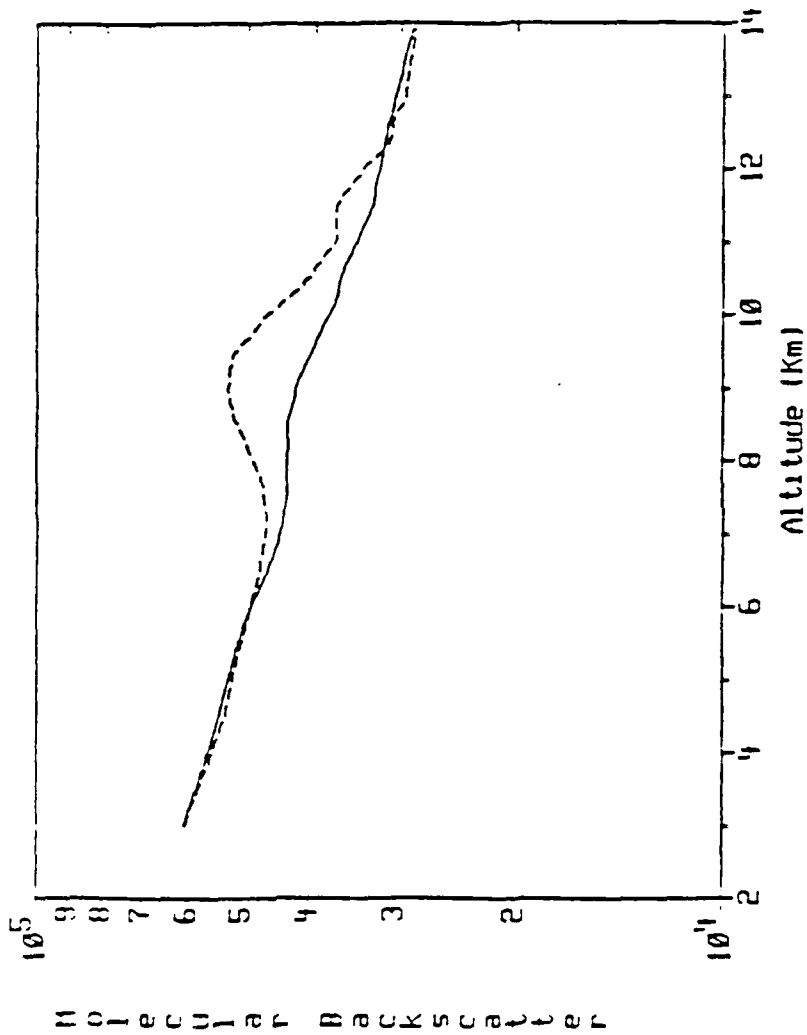
Fig. 8 Inaccuracies in the determination of calibration coefficients C_{aa} and C_{am} lead to a residual aerosol signal in the molecular channel which can be seen as a decrease in the log slope of the signal (7 - 12 km). The effect can be severe when average coefficients are used to separate aerosol from molecular scattering in long time averages of raw data (dashed line). The effect is lessened when each shot is synthetically calibrated before summing (solid line).

molecular signal in this region is due to incomplete separation of the photons scattered by cloud particles from those scattered by molecules. Incomplete separation of the molecular signal is due to inaccuracies in the determination of C_{aa} and C_{am}. The new technique shows an 8 fold improvement in the signal separation. Some residual cross-talk still remains, but this represents an estimated error of +.15% in C_{am} or a -.11% error in C_{aa}. Further improvements in the determination of the coefficients will require better estimates of the tuning drift with time.

C. Effects of statistical noise on extinction measurements

As shown in chapter II, HSRL measurements of extinction depend on the accuracy of determination of the log slope of the inverted molecular backscatter return (see eq. 2.7). In addition to photon counting noise in the backscattered signal, account must be taken of the statistical variations in the determination of the background light. Inaccuracies in the background light subtraction produce a systematic R^2 modulation of the observed signal. The current HSRL configuration produces signals (~10^2 photons/second) which are small compared to background light levels (~10^4 photons/second) for daylight measurements at cirrus altitudes. Thus, it was found necessary to evaluate the effects of errors in background light estimation in order to establish error bars on the presented measurements. For reasons outlined later in this section, the HSRL extinction measurements were evaluated over the entire depth of cloud.

By writing:

$$\tau = .5 \ln\left[\frac{\beta_m(R_2)}{\beta_m(R_1)}\right] + .5 \ln\left[R_1^2 (N_{m1} - N_{\varepsilon 1})\right] - .5 \ln\left[R_2^2 (N_{m2} - N_{\varepsilon 2})\right]$$

Where:

R_1, R_2 inner and outer range in the optical thickness estimate

τ optical depth from R_1 to R_2

N_{m1}, N_{m2} observed molecular signal at R_1, R_2

$N_{\varepsilon 1}, N_{\varepsilon 2}$ total error signal at R_1, R_2

An estimate of the error in the total optical thickness of the cloud

induced by errors in $N_{\varepsilon 1}$ and $N_{\varepsilon 2}$ may be written:

$$d\tau = \frac{\partial \tau}{\partial N_{\varepsilon 1}} dN_{\varepsilon 1} + \frac{\partial \tau}{\partial N_{\varepsilon 2}} dN_{\varepsilon 2}$$

which may be evaluated as:

$$\overline{d\tau} = \sqrt{\left[\frac{\partial \tau}{\partial N_{\varepsilon 1}} dN_{\varepsilon 1}\right]^2 + \left[\frac{\partial \tau}{\partial N_{\varepsilon 2}} dN_{\varepsilon 2}\right]^2 + 2\left[\frac{\partial \tau}{\partial N_{\varepsilon 1}} \frac{\partial \tau}{\partial N_{\varepsilon 2}} dN^2_{\varepsilon_b}\right]}$$

(3.19)

where $\overline{d\tau}$ is the average error in the optical thickness and N_{ε_b} is the expected number of error photons due to a mistake in the estimation of the background signal. Because the same background signal is subtracted from the measured signals at both ranges, N_{ε_b} appears in the covariance term in this expression. It is important to note that the correlated term relates to errors in the background estimation, while the other two uncorrelated error terms relate to the total errors at R_1 and R_2 due to photon counting statistics in the measured signal. N_{ε_b} may be estimated as:

$$dN^2_{\varepsilon_b} = \sqrt{C^2_{am} B_a + C^2_{mm}(R_1) B_m} \cdot \sqrt{C^2_{am} B_a + C^2_{mm}(R_2) B_m} \cdot \xi^2$$

Where $B_{a,m}$* are the total accumulated background counts in the aerosol and molecular channel background counters and ξ is the ratio of receiver range bin integration time to background counter integration time.

---

*Note that $B_{a,m} = b_{a,m} / \xi$

Using:

$$N_{\varepsilon 1,2} = \sqrt{C_{am}^2 \, S_a(R_{1,2}) + C_{mm}^2(R_{1,2}) \, S_m(R_{1,2})}$$

The partial derivatives may be evaluated as:

$$\frac{\partial \tau}{\partial N_{\varepsilon 1}} = \frac{-.5}{N_{m1} - N_{\varepsilon 1}}$$

and:

$$\frac{\partial \tau}{\partial N_{\varepsilon 2}} = \frac{.5}{N_{m2} - N_{\varepsilon 2}}$$

Since signal errors are dependent on the square root of photon counts, any process which increases the effective number of backscattered signal photons will reduce the measurement errors.

Longer background count integration times ($<\xi$) would decrease the error contribution from statistical variations in skylight estimation. However, the current HSRL transmitter is limited to an 8 kHz pulse repetition rate which precludes longer background count integration on a shot by shot basis.

Longer signal averaging times result in statistical error reductions from all sources. Unfortunately, the loss of time resolution can create difficulties in measurements in non-stationary phenomena, such as cirrus.

Statistical errors are also reduced by increasing $R_2 - R_1$, providing the signal remains measurably non-zero at the far range point. This method limits the range resolution for extinction measurements, however.

In current HSRL operations, the per shot background count statistical

variations exceed the cloud signal at cirrus heights. Constrained curve fitting procedures can help remove statistical noise in the signal in regions where there is good knowledge of the functional form of the signal. Such is the case in clear air regions which are characterized by pure Rayleigh scattering. This latter technique has been employed in this thesis and will be discussed in chapter IV.

D. Observed Scatter in the Tuning Ratio Estimations

A typical record of S_a / S_m measurements for local uniform aperture illumination of the receiver with transmitted laser light was presented in fig. 7. Observations of this sort were made to produce HSRL calibration scans and also to track tuning drift between calibration scans during data acquisition. Point scatter in this plot may be generated by two mechanisms. The first is photon counting noise. This mechanism accounts for about half the short time scale variations observed. Longer time averages would reduce these variations, but would also significantly increase the system calibration time at the expense of data acquisition time. Less attenuation of the laser light input to the receiver would also result in improved statistics. The limitation here is that all the photons are contained within the 15 ns wide laser pulse. Significant increases in the counting rate observed by the receiver would exceed the maximum counting rate capabilities of the data system and introduce non-linearities in the measured signals. Thus, counting rates are restricted to an average of less than .1 photons per laser pulse.

The remaining half of the deviations in the ratio may be due to short term variability of the spectral tune of the laser relative to the receiver. Possible sources for this wavelength jitter include etalon pressure controller variations and changes in the angular characteristics of the laser light. Pressure controller jitter has not been observed at a level sufficient to have a significant effect on the observed ratios.

An approximate calculation, based on the time-variant displacement of

a retro-reflection of the laser observed in the image plane of the telescope, has only accounted for 10% of the remaining fluctuations. The maximum value of this effect was evaluated by making the assumption that all the light in the laser beam is concentrated at the maximum laser divergence half-angle (~30 μR), and that the central axis of the beam undergoes an angular displacement equal to that observed in the focal plane of the telescope. For small angles the effect may be evaluated using:

$$\partial\sigma = \sigma\, \theta\, \partial\theta$$

(3.20)

Where σ is the wavenumber of the laser light and θ is the angle between the incident radiation and the optical axis of the etalon.

The remaining variance in the tuning ratio remains unexplained; but, since the scatter seems to be random, the effect is abated by employing a spline fit to the observed ratio during calibration scan processing. In data analysis, the ratio actually used to determine temporal tune variations is taken from this spline fit through all calibration checks performed during the appropriate data segment.

IV. Data acquisition and analysis

The data presented in this chapter were acquired at Madison, Wisconsin during the FIRE experiment in the Fall of 1986. A summary of the HSRL operations during this period may be found in Fig. 9.

The HSRL experimental data set contains 124 hours of observations of which 43 hours were spent establishing system calibrations. The atmospheric data acquisition period represents some 75,588 actual backscatter profiles. Each 4 second profile was a range-resolved average over 30,000 transmitted laser pulses.

During the 105 hours of fixed, vertically-pointing operations, high clouds (above 6 km altitude) were observed for 36.5 hours. Cloud free periods were observed for 50.2 hours, while periods of low, middle, and mixed height clouds were observed during the remaining 18.3 hours. In this latter category, it must be noted that low clouds were present whenever weather prevented operations. Additionally, high clouds may not have been observed during overcast conditions because of the limited penetration capability of the lidar.

A synoptic depiction of the data observations is presented in figures 10 through 22. These views are range time indicator (RTI) displays of the HSRL fixed, vertically-pointing data acquisition periods. Thus, they represent a time history of cloud generation, dissipation and wind driven drift over the lidar site. Altitude, variability, and physical thickness of the cloud layers (where penetration is achieved) are clearly shown in this form

Fig. 9: Hsrl Operations During Fire

Time (GMT) / **1986 Date**

Legend:
- Calibration
- Data
- Maintenence
- Failure
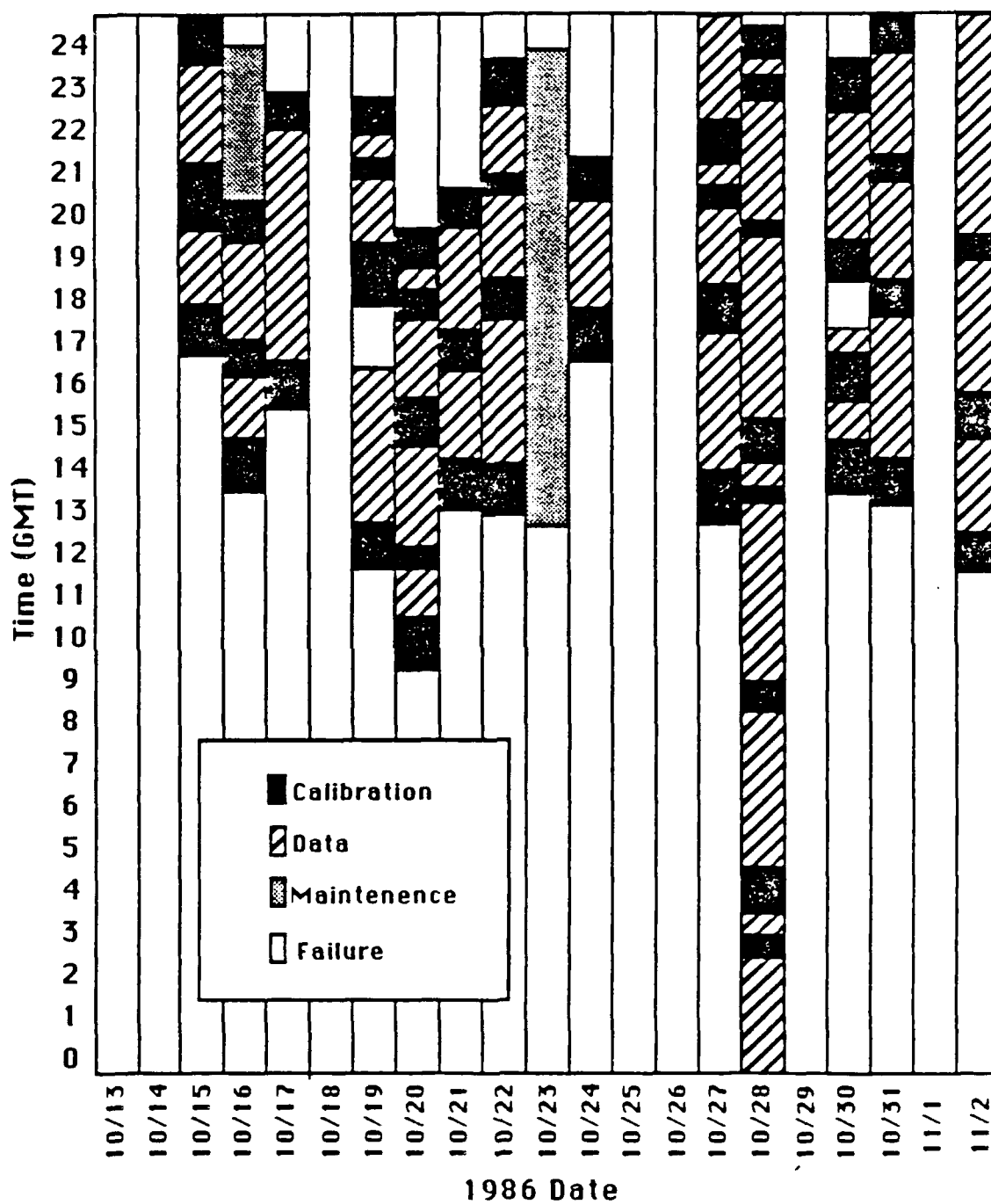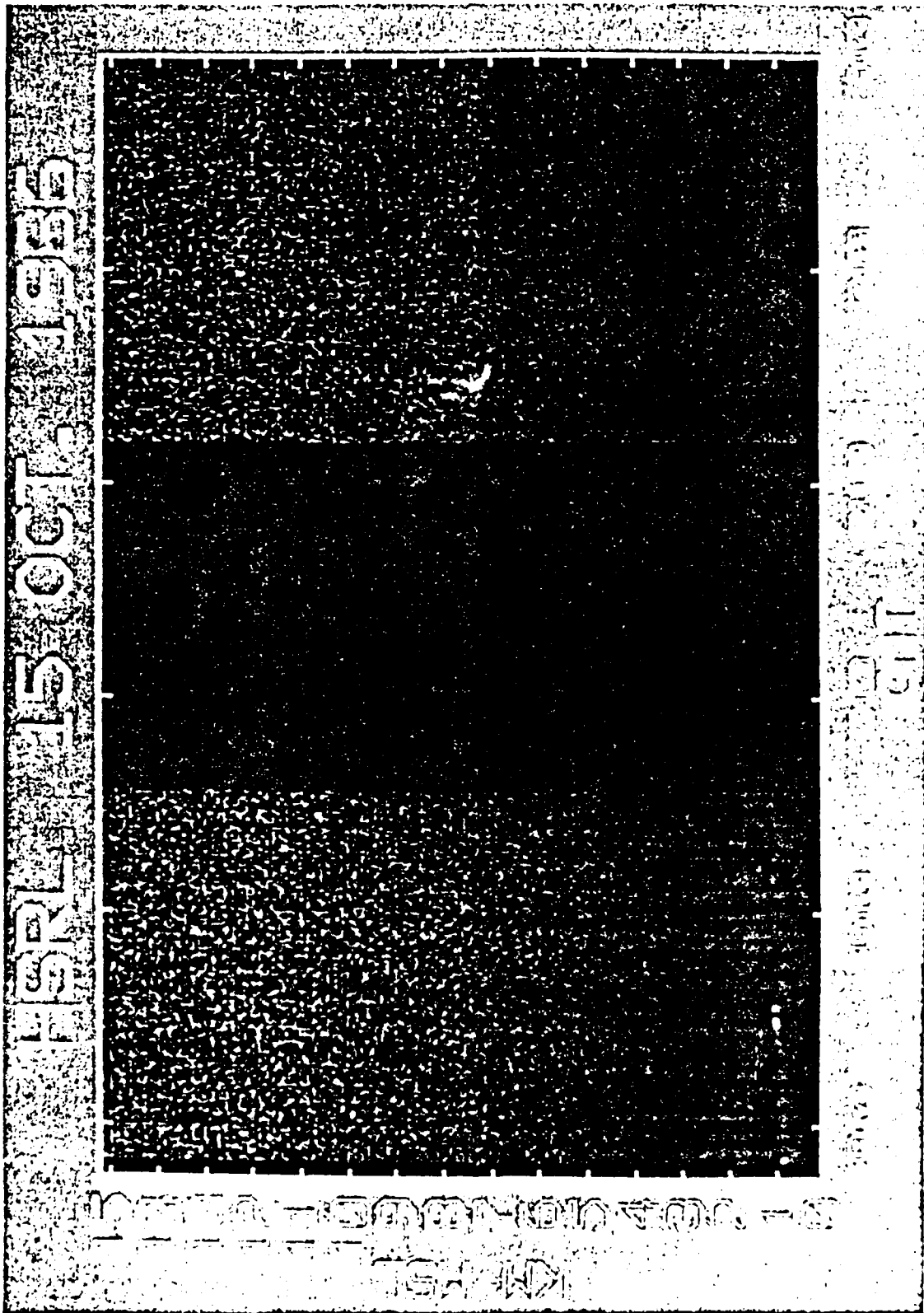
Fig. 10

Fig. 11

Fig. 12

Fig. 13

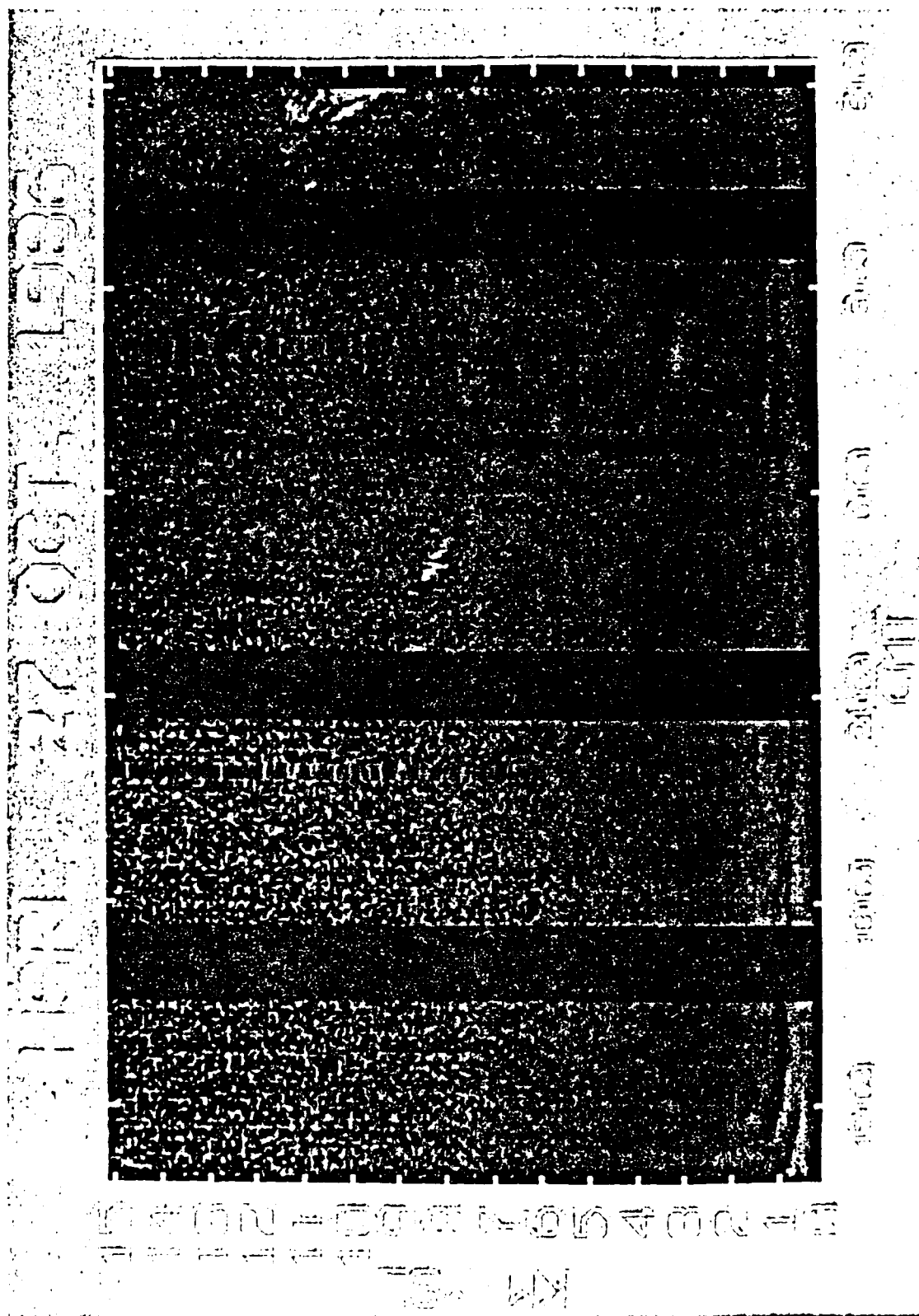Fig. 14

Fig. 15

59

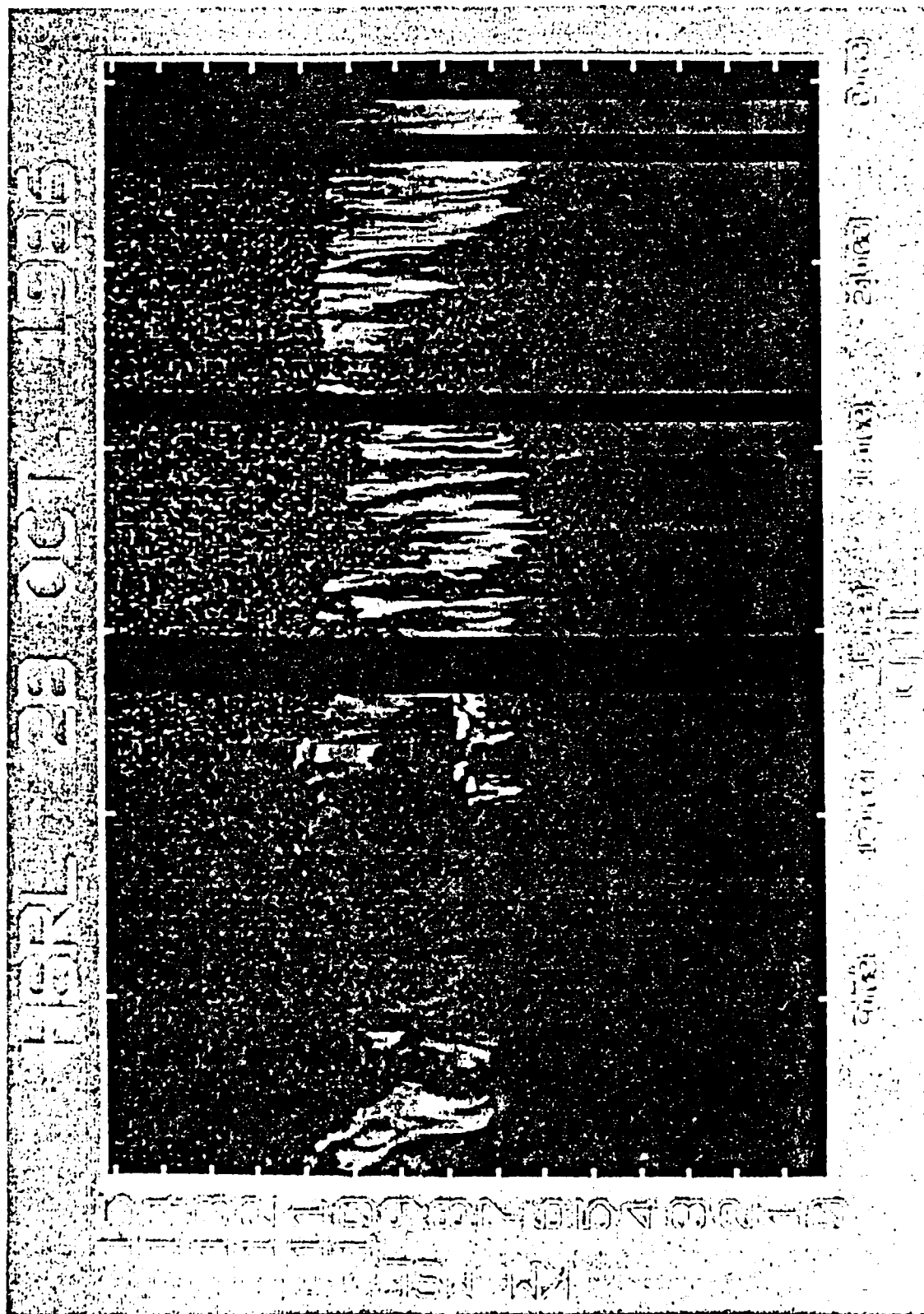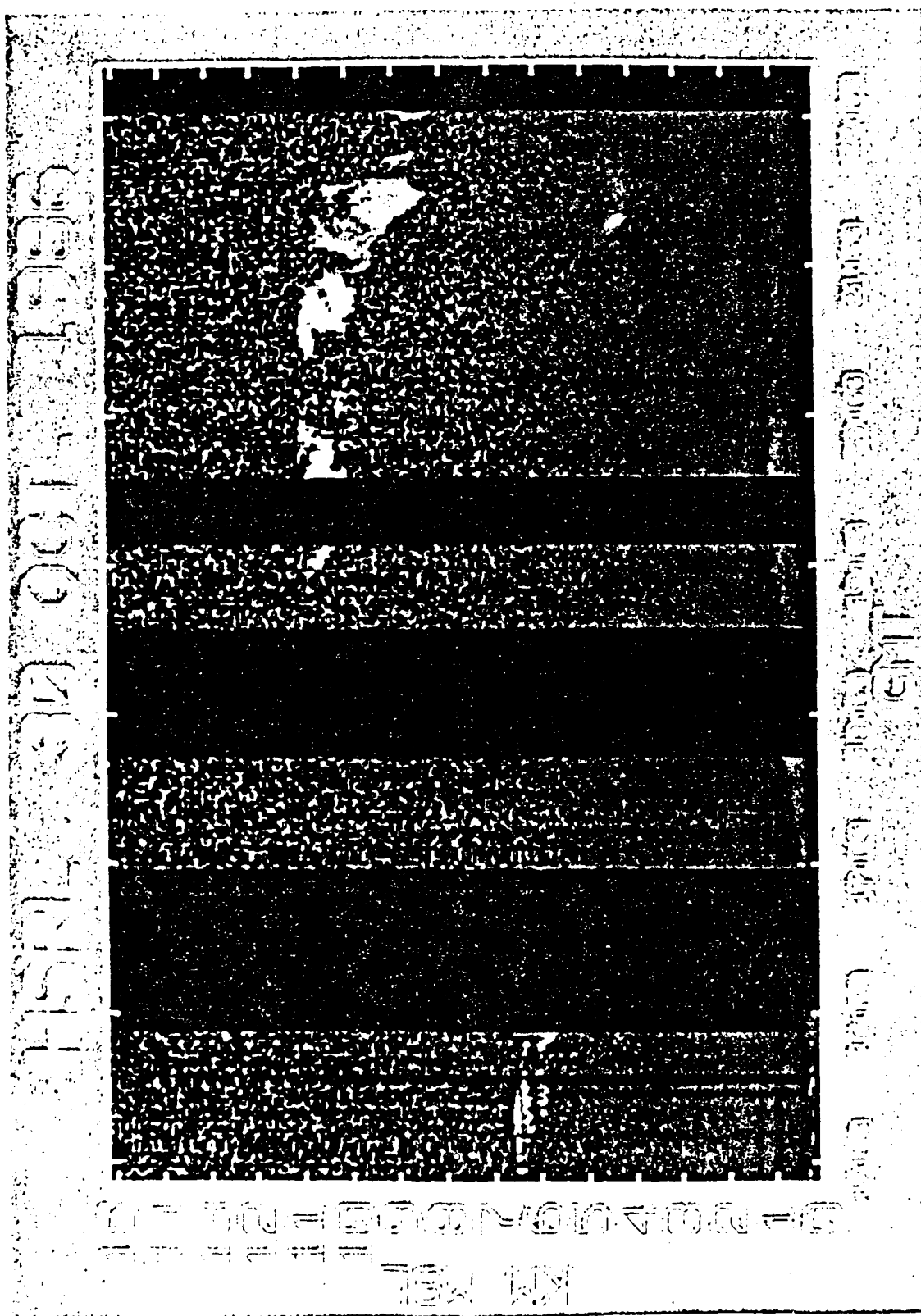Fig. 16

Fig. 17

Fig. 18

62
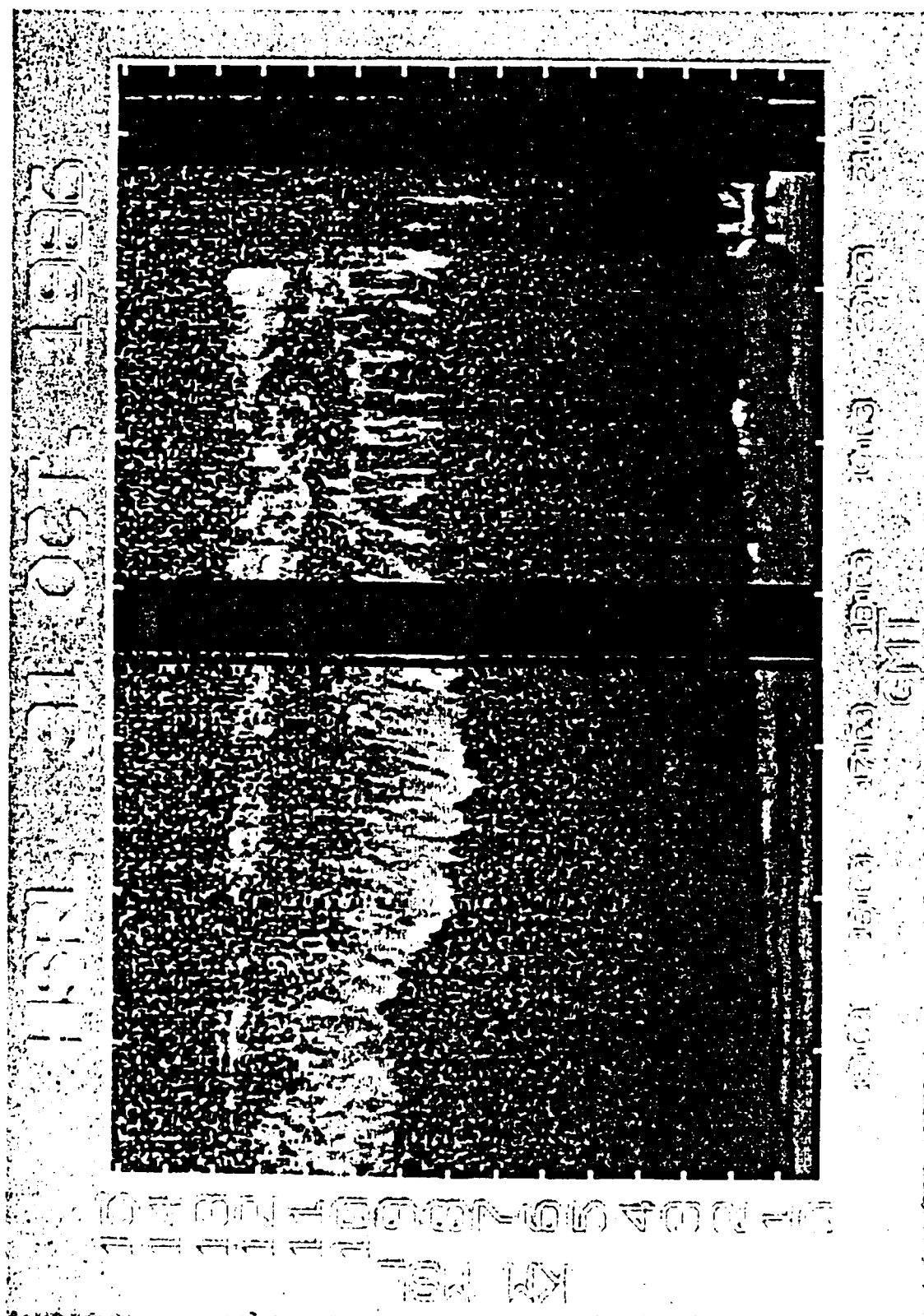

Fig. 19

63
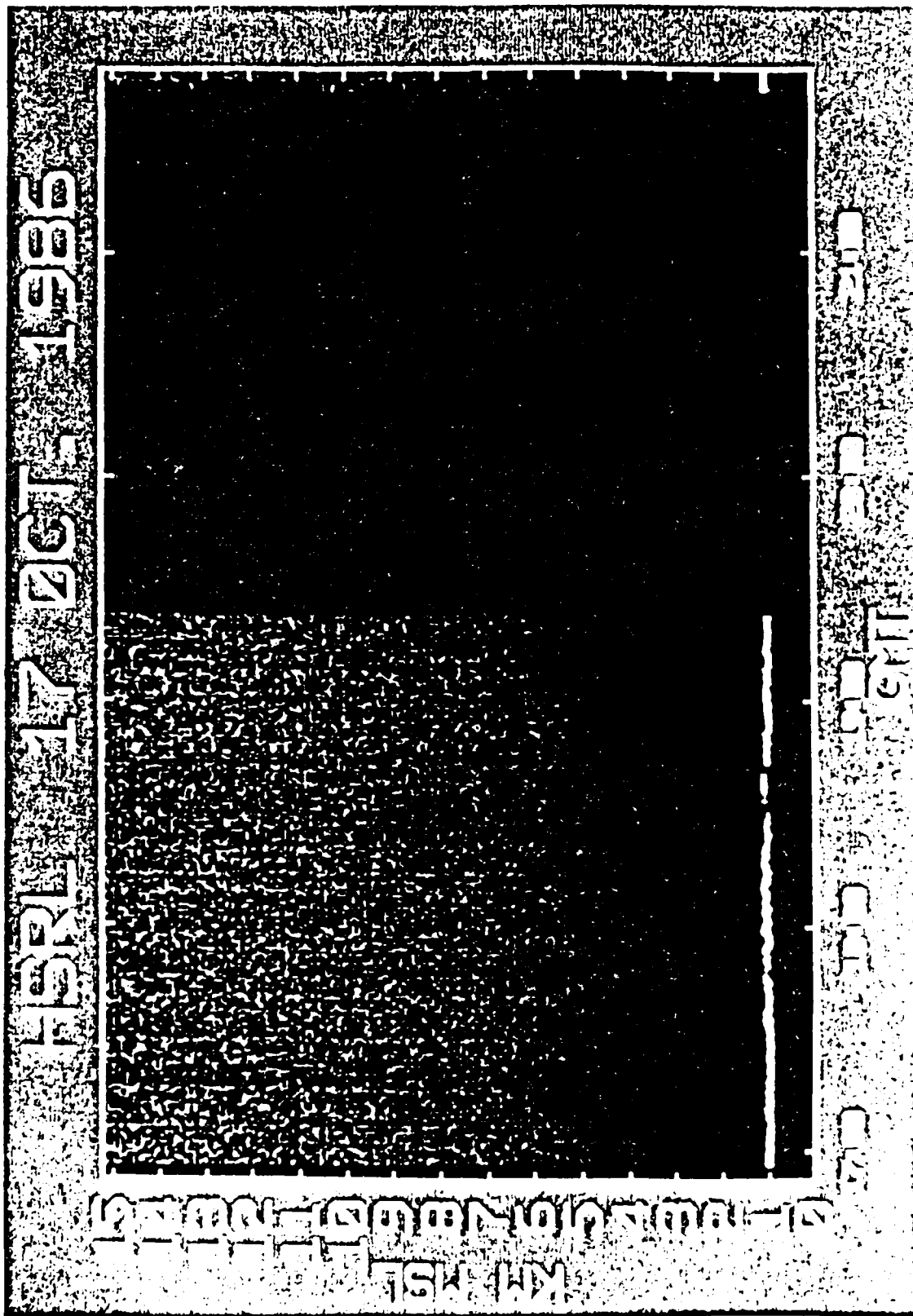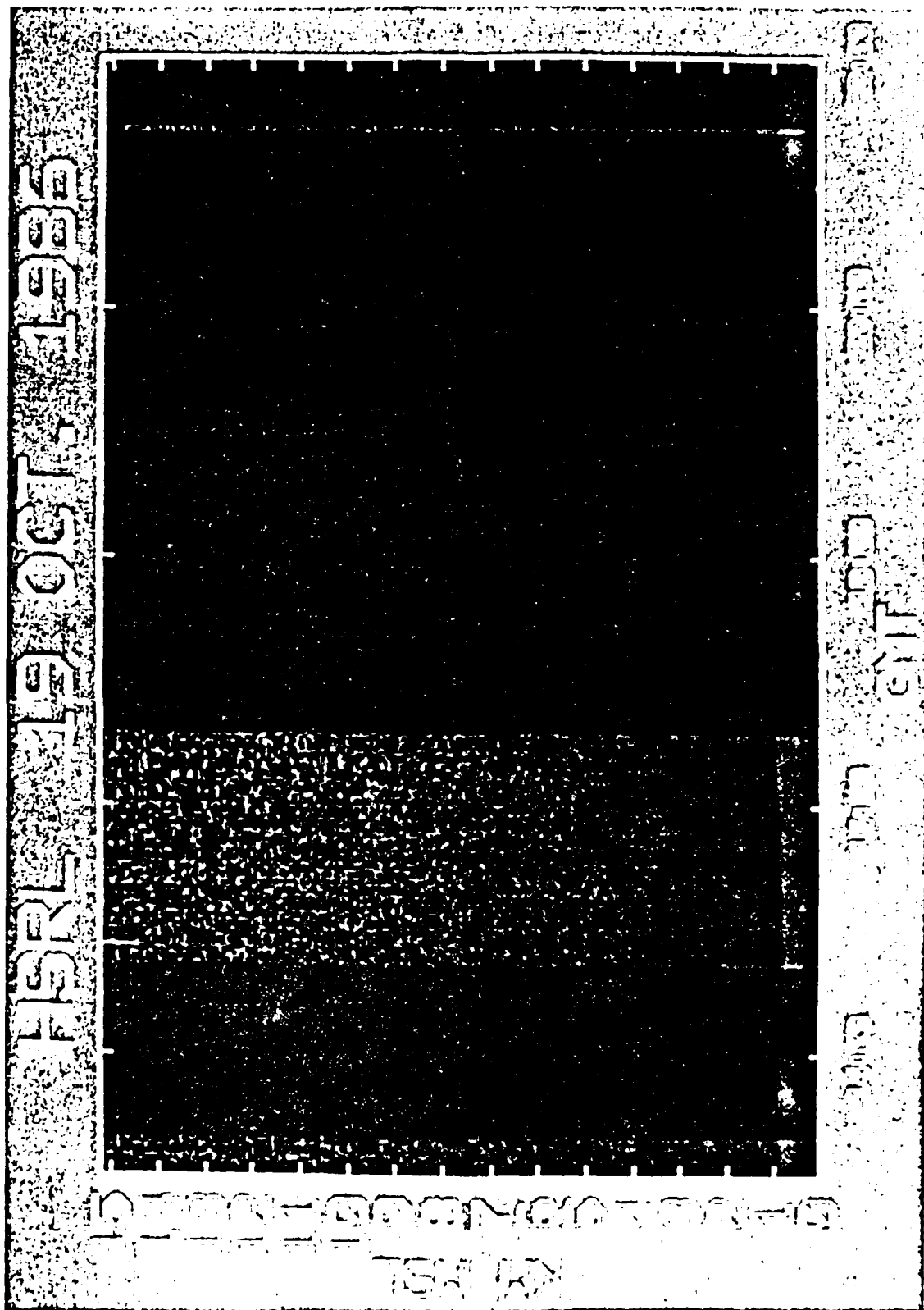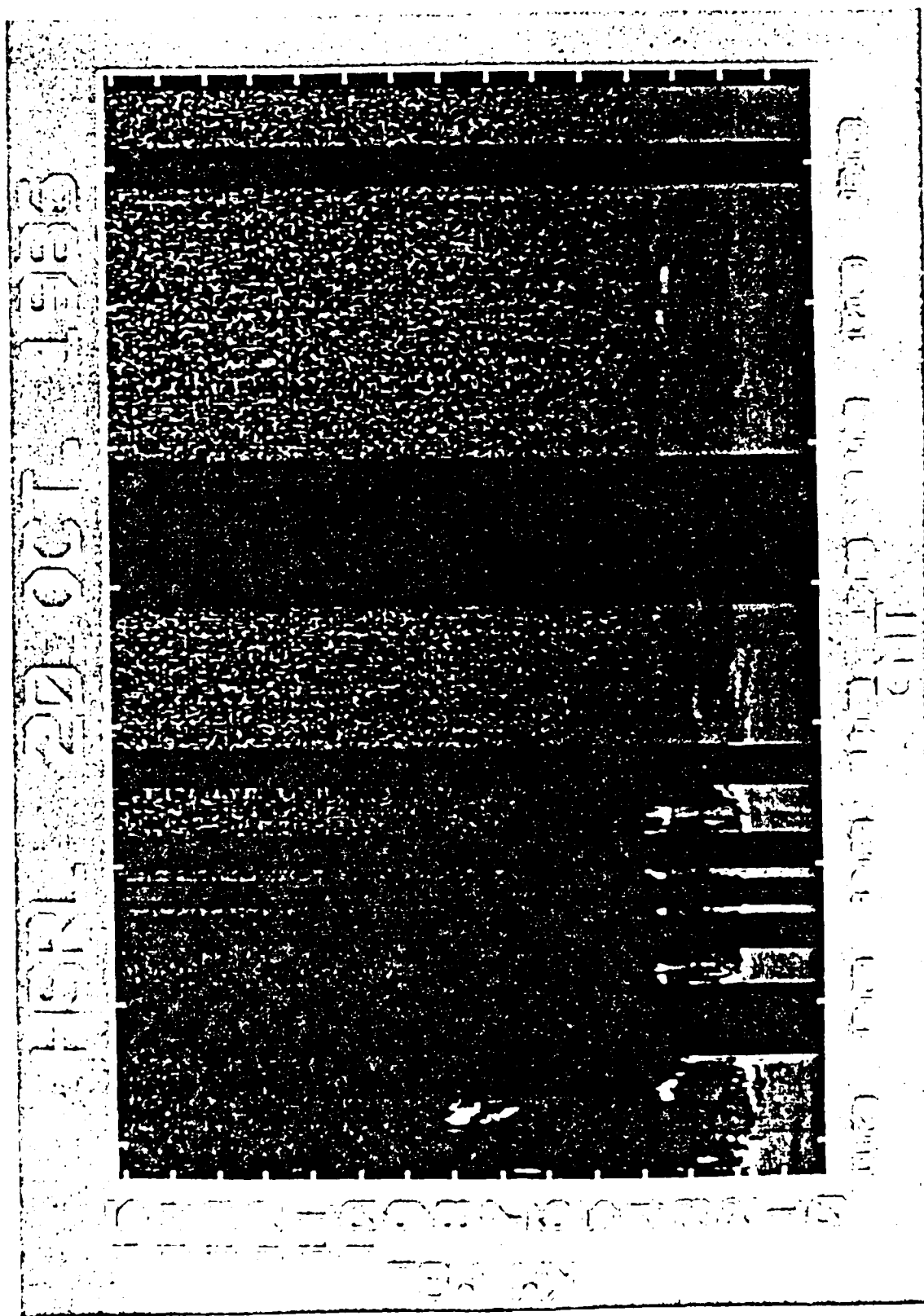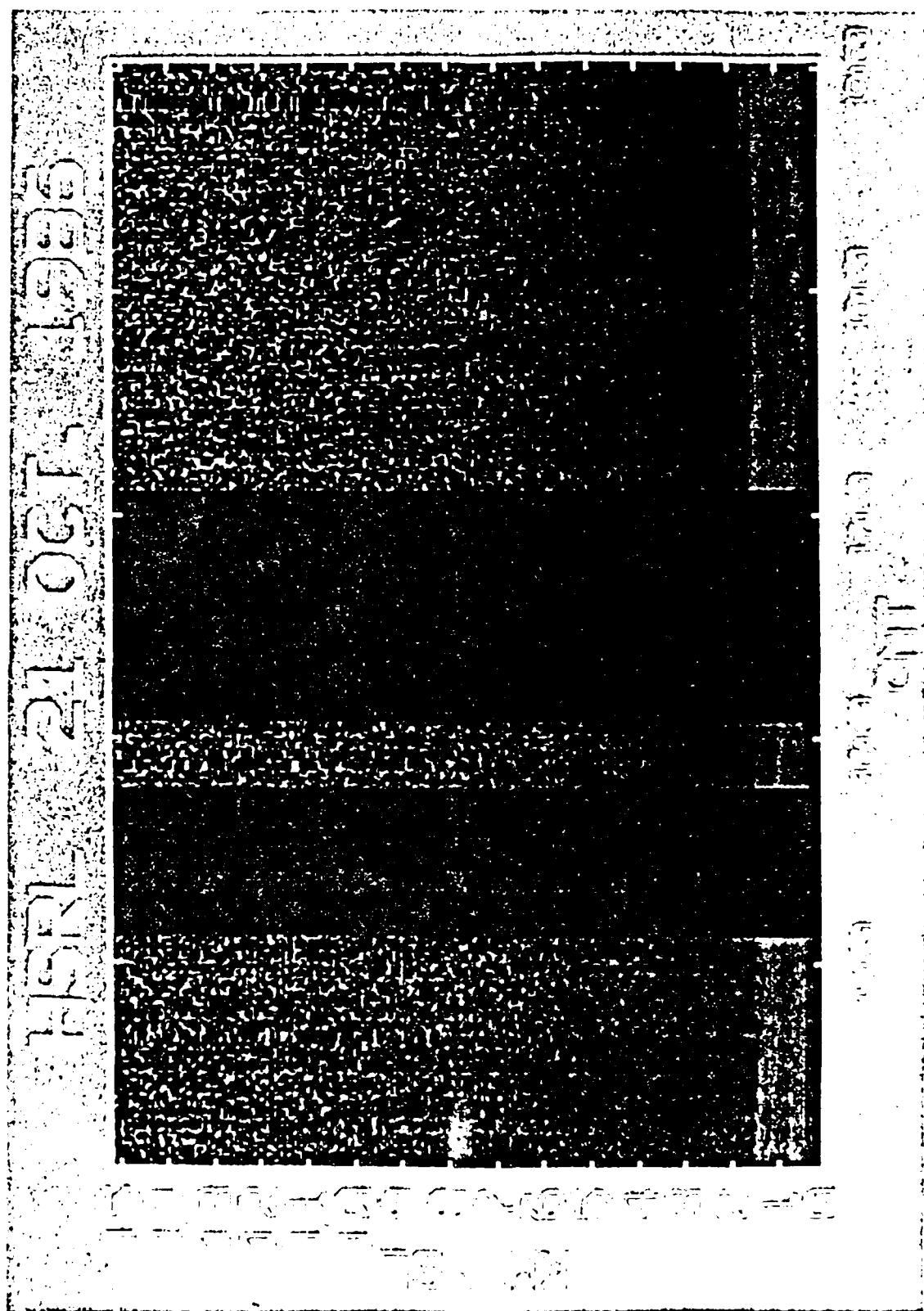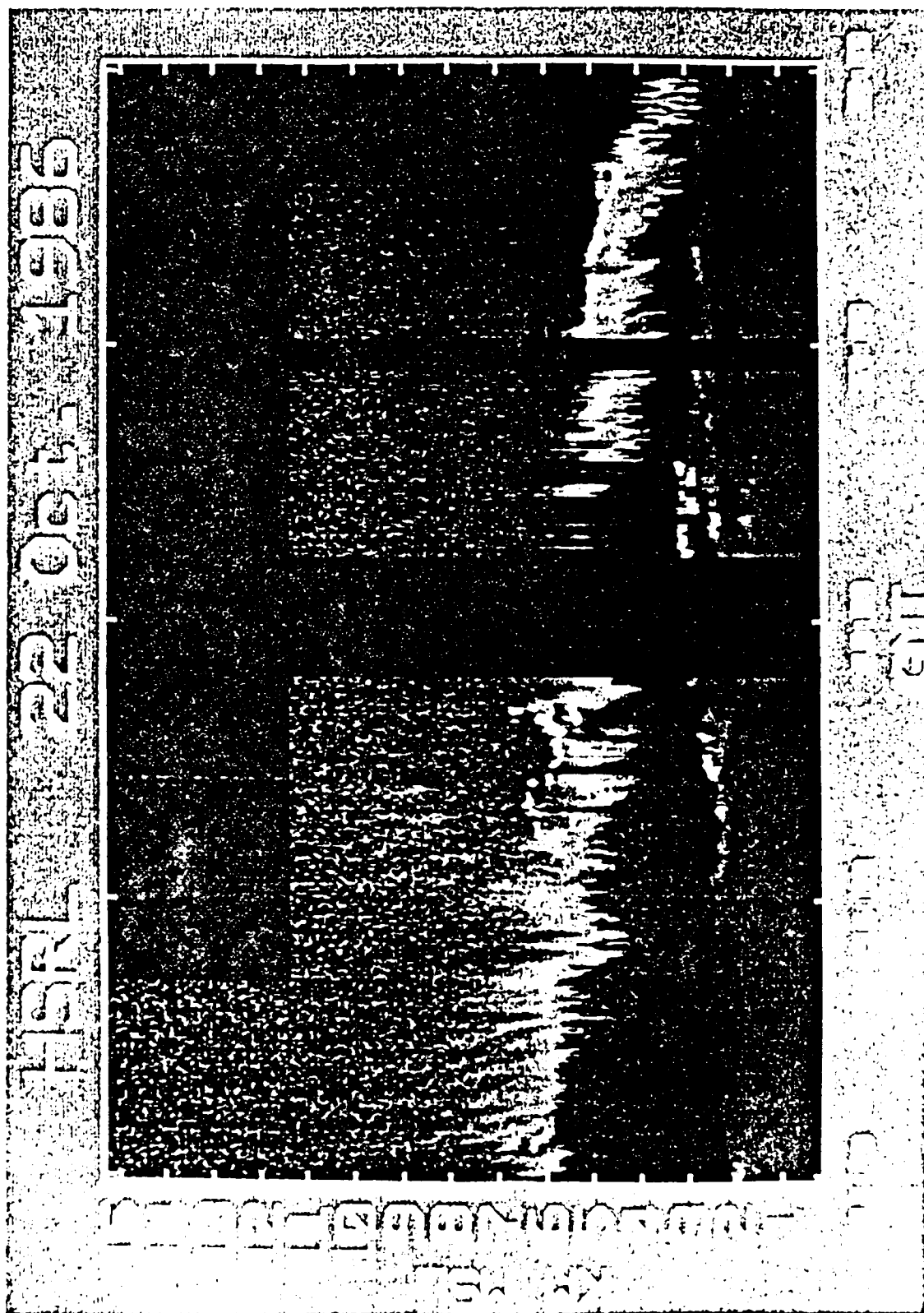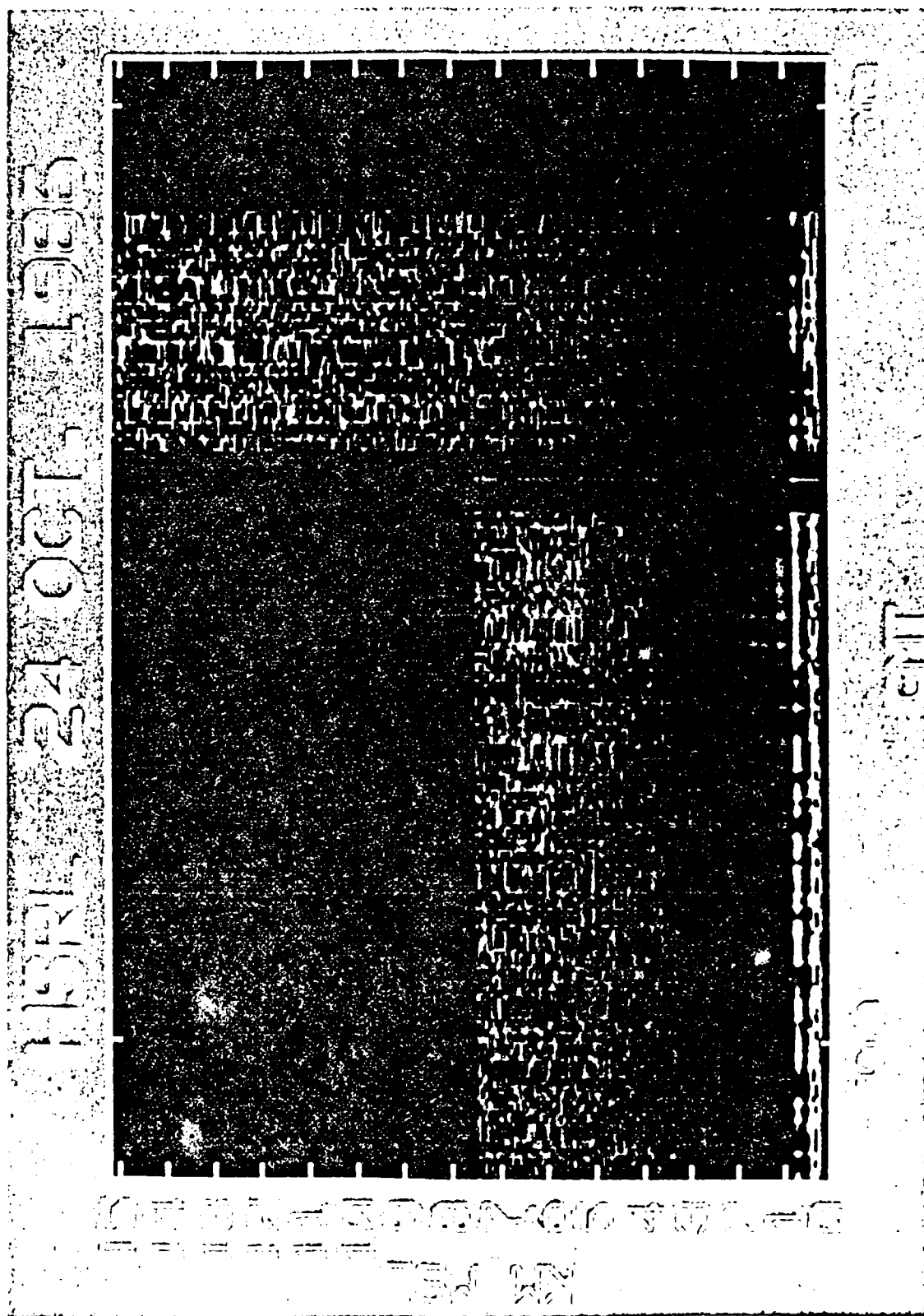
Fig. 20

Fig. 21

Fig. 22

of display.

The pictures were produced from the log of the raw aerosol channel returns which have had the background light removed and have been corrected for the R^2 signal dependence. It is important to note that these images have not been corrected for extinction with increasing cloud penetration. This form of representation has been chosen because background count statistics precluded direct extinction estimations on a sufficiently short time scale to produce meaningful pictures. In addition, the grey scale has been enhanced by an arbitrary linear stretch of the log signal values to show the greatest detail in the cloud. White areas are those regions where the backscatter signal exceeded the maximum brightness value in the enhancement grey scale.

Frequent system calibration and background light checks generated gaps in the data of 16 - 36 seconds every 3.5 - 7 minutes. Accordingly, any data gaps of less than 1 minute duration have been filled, for esthetic reasons, by a linear interpolation in the time domain.

A vertical expansion of the data by linear interpolation has been performed since the present data acquisition system has a maximum resolution of 256 range bins, while the display is capable of a vertical resolution of 1024 pixels. On occasion, maximum range was traded-off for range resolution resulting in the horizontal black areas beginning at about 7 or 11 km and continuing to 15 km. Data acquired in these high resolution modes has been compressed by averaging to facilitate presentation alongside the data generated during maximum range operations.

Several caveats need to be applied when interpreting these pictures. Where low clouds exist, they can obscure the cloud data from higher levels. Also, in regions of thick cirrus (e.g. Oct. 22), the cloud signal can weaken markedly with penetration due to extinction, even though the physical cloud may be thickening. Extinction corrected time-averaged backscatter profiles for selected data cases will be presented later in this chapter.

On viewing fig.'s 19 and 22, one notes that the cloud tops are often observed to descend linearly with time while the cloud bottoms occasionally demonstrate an altitude dependence with time indicative of a decelerating decent rate. This is most clearly evident in fig. 19 between 6:30 and 7:30 GMT. A blow up of this regions was presented in chapter 1 fig. 1. On the assumption that the entire cloud is decreasing in altitude with time, the observed cloud form depicted in fig. 1 may be the result of a decrease in the in-cloud crystal fall speed with altitude. One possible cause for this effect is a decrease in terminal velocity with increasing atmospheric pressure. The change in terminal velocity may be evaluated following Starr and Cox (1985b):

$$\frac{V}{V'} = \left[\frac{P'}{P}\right]^{\frac{1}{3}}$$

where V is the terminal velocity at altitude and P is the atmospheric pressure at that altitude, with primed quantities evaluated at the original altitude, and unprimed quantities evaluated at the new altitude. This effect

produces an expected decrease of 2% in the fall velocities, much smaller than required to produce the observed phenomenon.

It is possible that the terminal velocities of the cloud particles decrease significantly as they become smaller due to evaporation (or sublimation) into a low relative humidity environment. Another possibility is that the addition of moisture to the atmosphere caused by the evaporation of cloud particles can decrease the rate of evaporation for particles falling at a later time, causing a time dependent lowering of the evaporation altitude. This latter mechanism can produce a curved cloud bottom in RTI displays without the need for the entire cloud to descend with time.

Quantitative evaluation of these two possible causes for the observed cloud shapes are beyond the intended scope of this thesis. Because of the complex interaction of the environment with the descending cloud particles, evaluation would require the development of a sophisticated model. Further, more detailed knowledge of the environmental conditions is required than is currently available. In addition, evaluation of these effects is complicated by environmental wind sheer and the effects of synoptic scale advection. An estimate of the effects of wind sheer on this data indicated that the cloud view presented in this RTI was a slice through a complex three-dimensional cloud structure. Detailed evaluation of the true cirrus cloud profiles will therefore await a more powerful lidar with real time scanning capabilities.

The increasingly mottled appearance of the displays with altitude in figures 10 - 22 is a function of the photon count statistics in the background

light and backscatter signals. Thus the effects of background skylight on signal integrity may be clearly seen by the conspicuous absence of noise from 22:00 GMT on Oct. 27 to 12:00 GMT on Oct. 28 (local sunset to sunrise). An evaluation of the HSRL sensitivity to this effect was presented in part C of chapter III. Because of limitations imposed by the low average power and per pulse energy of the current system transmitter (see Table 3.1), quantitative measurements have been restricted to a few data segments which met the following criteria:

1. Cirrus with sufficiently small integrated optical depths to allow estimation of the Rayleigh backscatter from below-cloud and beyond-cloud altitudes.

2. Cases with reasonable homogeneity with regard to altitude and physical thickness. Thus allowing time averaged properties to be representative of true in cloud properties.

3. Cases where the above criteria held for at least 45 minutes in daylight cases, and 20 minutes at night.

It was found that the HSRL FIRE data set contained only 4 hours of data which met these criteria. Range resolved calibrated backscatter cross section profiles for these cases are presented in figures 23 - 28.

Figures 23 - 28 were produced from 45 minute data sums (centered on the stated time periods) according to equation 2.8. The separated aerosol signal was applied directly, while the molecular signal was smoothed according to a technique outlined in 3 below. The following rationale was used to generate this technique:

1. Since the raw aerosol channel is spectrally narrow, the

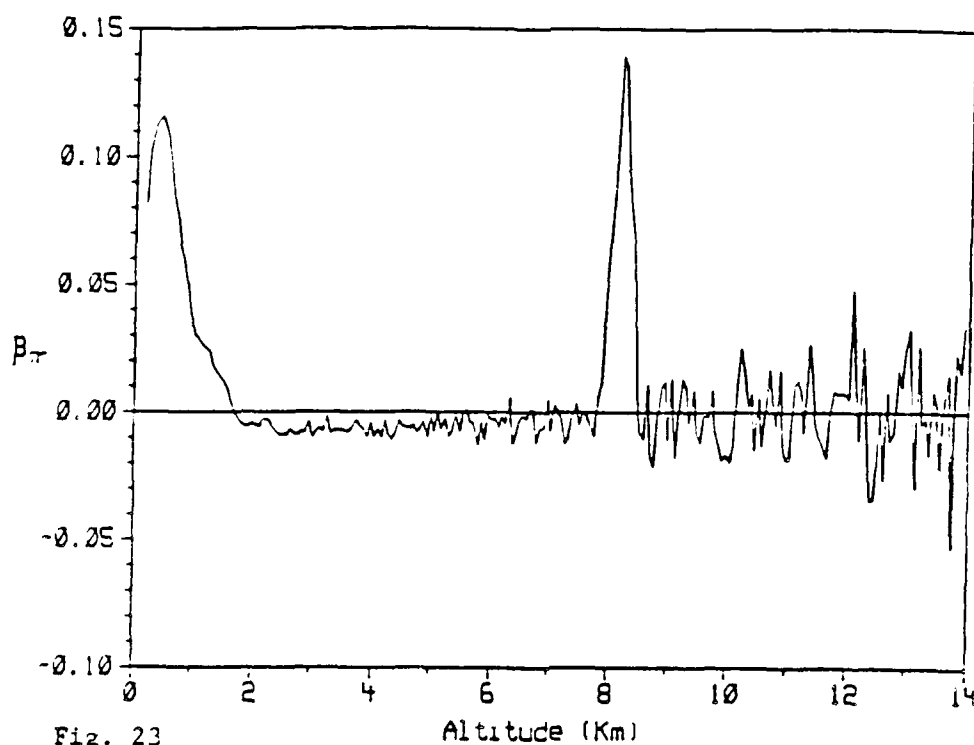X10^{-5} Backscatter X-Section (M^{-1} SR^{-1})   23:00 GMT 10/27/86

β_π

Fig. 23

Altitude (Km)

X10^{-5} Backscatter X-Section (M^{-1} SR^{-1})   14:25 GMT 10/31/86

β_π

Fig. 24

Altitude (Km)

Fig. 25

Backscatter X-Section (M⁻¹ SR⁻¹)   15:05 GMT 10/31/86

Fig. 26

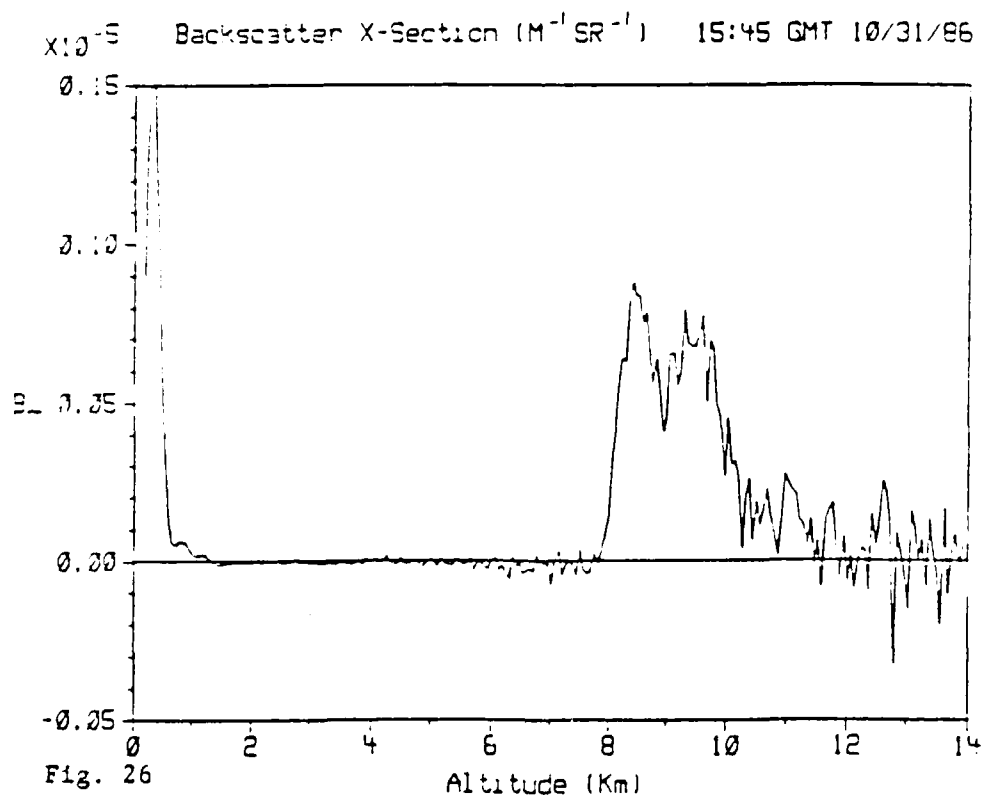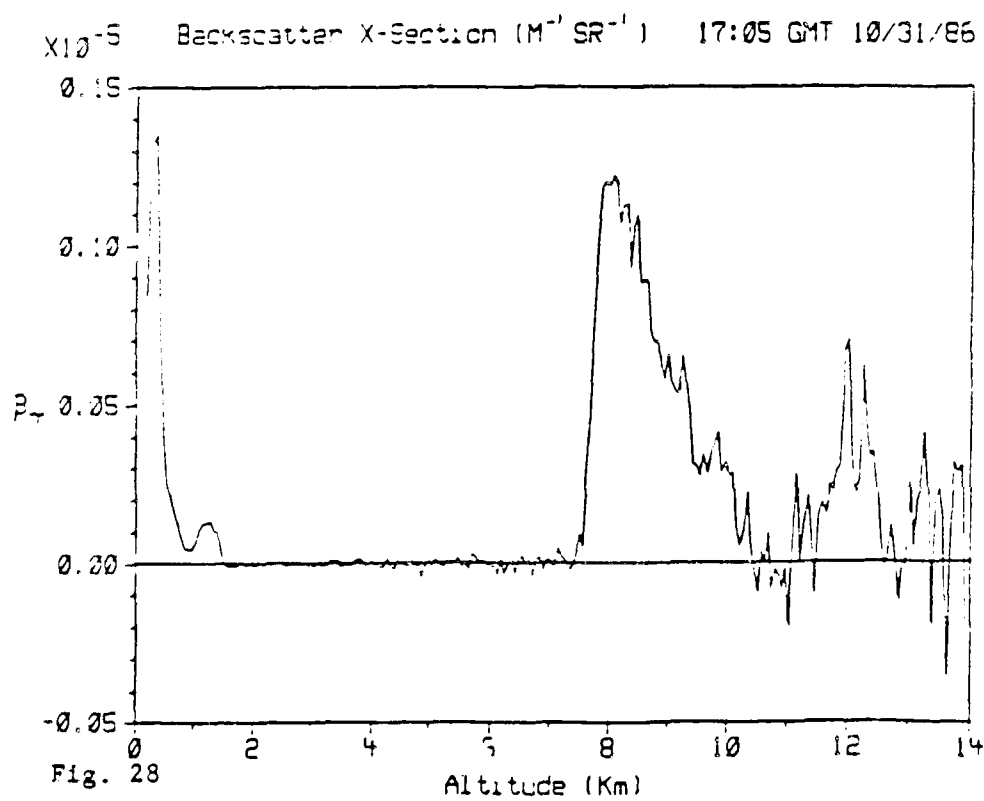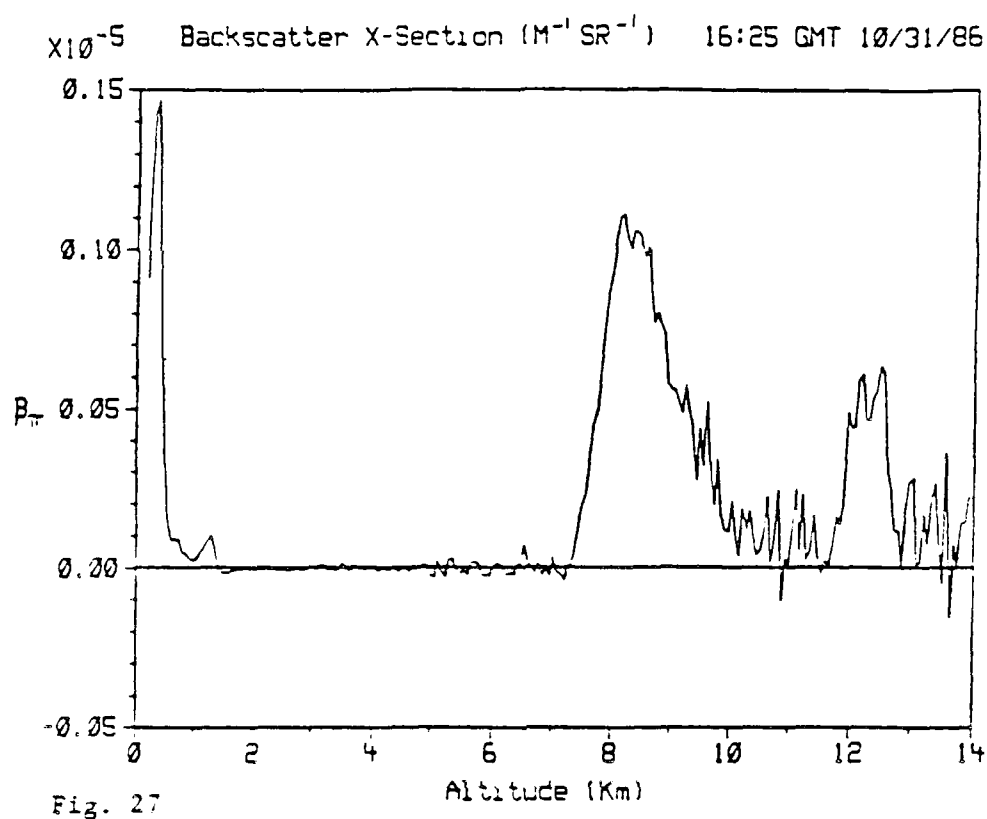Backscatter X-Section (M⁻¹ SR⁻¹)   15:45 GMT 10/31/86

Fig. 27

Fig. 28
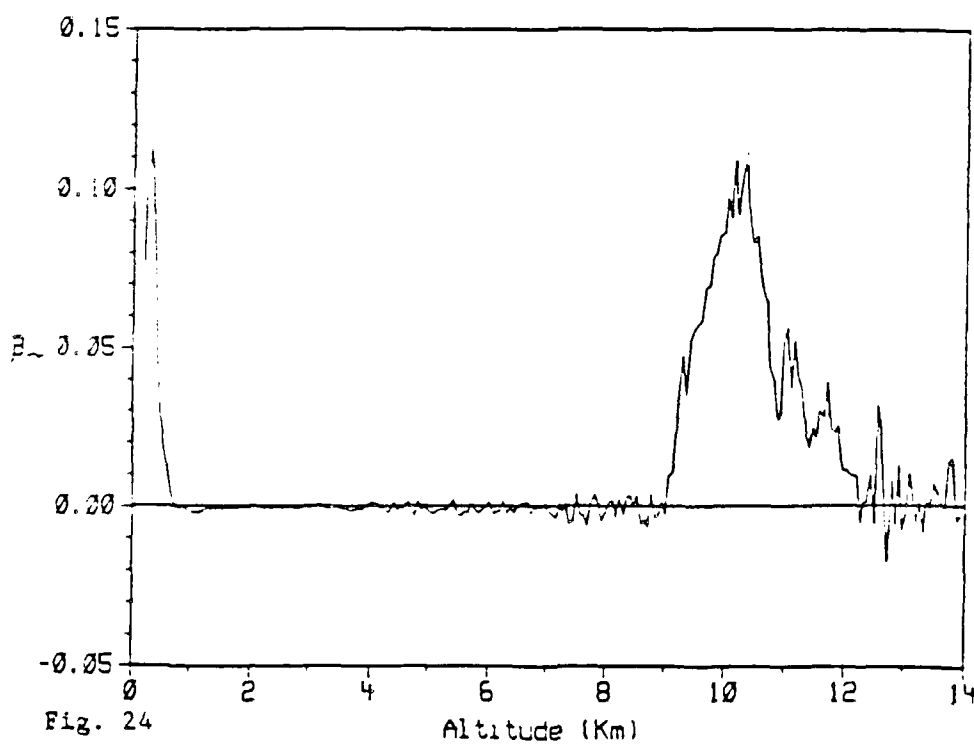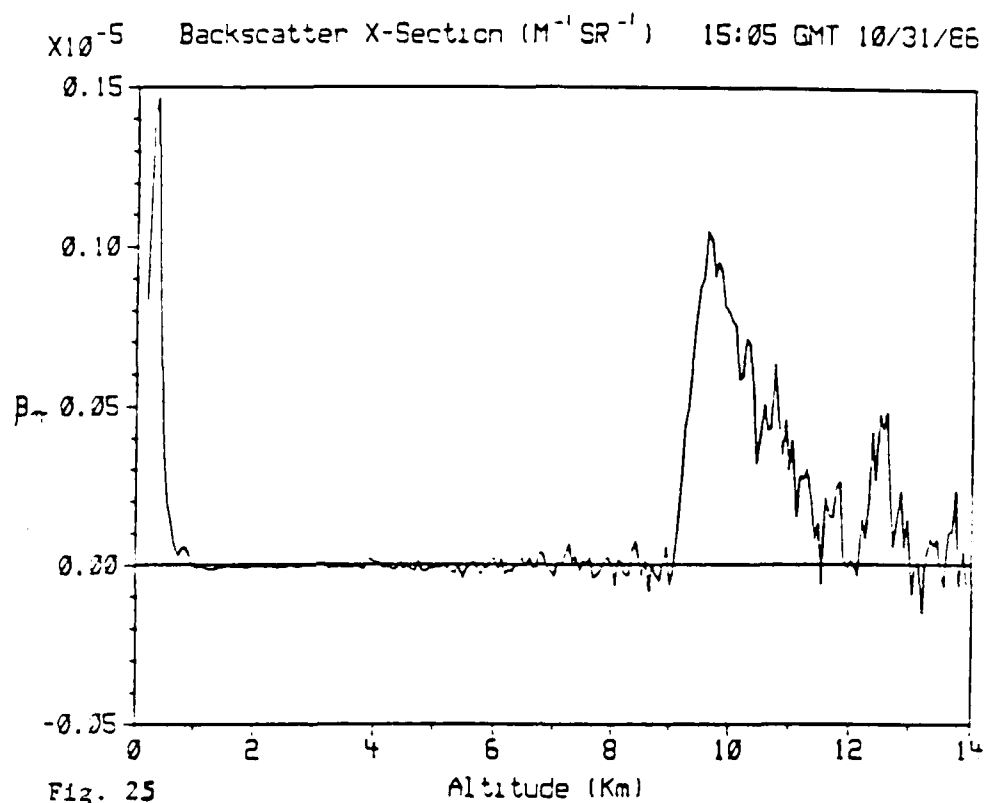
effective background skylight contribution to this channel is a factor of 6 smaller than i.. the raw molecular channel; yet, most of the information about particle backscatter is contained in this channel. Thus, smoothing in addition to the time average was not found to be necessary for the inverted aerosol signal.

2. The separation of the aerosol scattering component of the backscatter depends only on the calibration coefficients Cmm and Cma (eq. 3.15). These coefficients have been established with greater accuracy than Caa a..d Cam, owing to the smoothing effects of the convolution operation used in their calculation (see eq.'s 3.17, 3.18). Thus, the magnitude of the inverted aerosol return was considered to be an accurate representation of the true, attenuated, particle backscatter.

3. As stated, the coefficients Caa and Cam are less well known, therefore the inverted molecular signal return is subject to a small cross-talk contribution in regions of strong particulate backscatter. In addition, the molecular profile is re a: .-. noisy at the altitudes of interest. Consequently, an e·· ·· the true molecular backscatter signal va .e ·· · by a least squares fit of a range-atter..a··· · based on the known density pro· e ·· ·· above-cloud clear a·r ·e- ·· · · regions w·th ·he ·· S·· ·· .
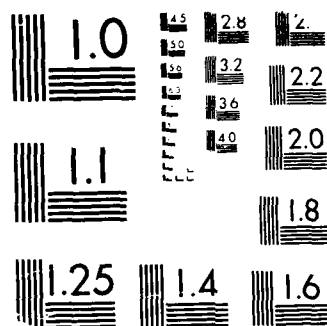
MICROCOPY RESOLUTION TEST CHART

section profiles for altitudes where the cross section is zero. The in-cloud region of the molecular profile is then estimated by connecting a straight line (in logarithmic domain) between the upper end point of the beneath-cloud fit and the lower end point of the above-cloud fit.

Negative backscatter cross sections are not physically possible; however, the negative going portion of the scale has been plotted to illustrate the local noise component in the measurements. It is important to note that there seems to be a slight systematic bias toward negative values which decreases with range. This effect is particularly evident in the fig. 24. The bias is an artifact of small inaccuracies in the determination of coefficients Cmm and/or Cma, and represents an overestimate of the number of photons backscattered from molecules. An error of -.08% in Cmm or +.12% in Cma can account for the discrepancy on this day.

On scanning through the backscatter cross section plots from Oct. 31 (fig.'s 24 - 28), one can plainly see that, for this day, the bottoms of the 9-11 km cloud layer were clearly defined. However, the tops of this layer dissipated slowly with altitude. It is important to note that the total cloud-layer optical thickness was less than 0.1. If one were to assume all the cloud extinction occurred at one point in the profile then errors at any point in the reported backscatter cross sections, due to the homogeneous-cloud fitting scheme applied to the molecular signal, could not exceed 20%. Also note that the cloud layer between 12 and 13 km (see fig. 27) had quite sharply defined tops and bottoms, even while the lower cloud exhibited a dissipating top structure. Therefore, the cloud top profiles indicated in the

backscatter cross section plots are real phenomena, and not due to inaccurate compensation for extinction with cloud penetration.

Such dissipating cloud top structures may have important implications for the estimation of cirrus cloud heights from space-borne lidar systems. As can be seen from equation 1.1, it is possible that an appropriate increase in backscatter cross section with range may just cancel the loss of signal due to increasing 2-way optical depth with cloud penetration. Under these conditions, the cloud may be invisible to simple lidar systems. Under other conditions, the cloud height and layer thickness could be poorly determined. This effect has been recently noted by other researchers (Kunz (1987)).

In order to demonstrate this effect, it is possible to solve equation 1.1 for a family of extinction profiles which would yield straight log-linear return signals. Assuming the extinction and scattering cross section are related by a constant backscatter phase function, one may write the range derivative of the logarithm of the lidar equation as:

$$S = \frac{d \ln\left[\beta_\varepsilon(R)\right]}{dR} - 2\beta_\varepsilon(R)$$

Where S is the log slope of the expected return signal. A Bernoulli solution may be employed to reduce this representation to a first order linear equation with the solution:

$$\beta_\varepsilon(R) = \cfrac{1}{\left[\dfrac{1}{\beta_0} + \dfrac{2}{S}\right] e^{\left[(R_0 - R)S\right]} - \dfrac{2}{S}}$$

(4.21)

Here R_0 is the range at which the cloud begins, and β_0 is the extinction at that range.

Fig. 29 presents the extinction profiles of three hypothetical clouds which would be "invisible" to nadir viewing lidars with the signal detection limits of 6, 4 and 1 (denoted A, B, and C) times the expected molecular backscatter signal from 8 km calculated at a wavelength of 510 nm. The clouds depicted in profiles A, B and C have respective optical depths of 1.1, .46, and .08 through the 3 km cloud thickness, and are thus both realistic and radiatively significant. Curves A, B, and C were calculated from eq. 4.21 to yield a log slope near 0 for a nadir lidar profile constructed according to eq. 1.1. β_0 was then chosen so that the resultant down-looking profile would produce a scattering ratio of 6, 4, or 1 for curves A, B, and C, respectively[*]. Thus, for example, a nadir viewing lidar with a minimum scattering ratio detection limit of 6 would not be capable of distinguishing from noise the backscatter signals produced clouds A, B, or C.

---

[*] Scattering ratio is defined here as the observed cloud backscatter cross section (including the effects of extinction) divided by the molecular backscatter cross section at 8 km calculated using eq. 2.6 and the density values given in the U.S. Standard Atmosphere (Hess (1979)).

Fig.'s 30, 31, and 32 depict the expected scattering ratio observations from lidar systems viewing clouds described by the β_ϵ profiles A, B, and C, respectively. The simulations assumed a fixed backscatter phase function of .03 sr^{-1} for the cloud particles. Lidar profiles are plotted for each cloud profile for both zenith viewing and nadir lidar observations. Note that for a cloud with this soft top/distinct bottom structure, it is possible to see the cloud bottom from below, but it may be possible to miss the cloud entirely from above. Also note that in all cases the up-looking lidar would not see the cloud tops because the backscatter cross section at this range must decrease to a level insufficient to produce a signal which exceeds the noise floor.
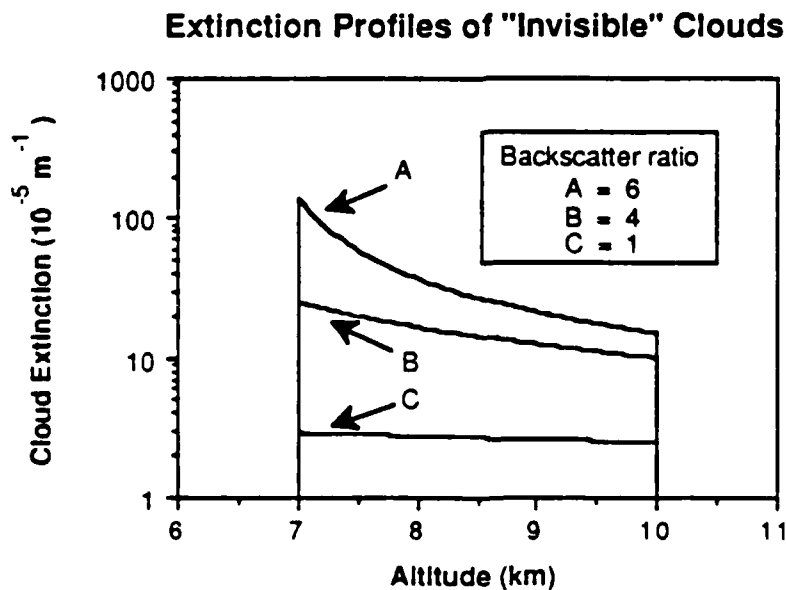
Extinction Profiles of "Invisible" Clouds

Fig. 29 From space, simple lidar systems with the detection limits A, B or C (see text) would not be capable of recognizing a cloud with the indicated extinction profile because the backscatter cross section increase with range is just large enough to compensate for the added

extinction with increasing penetration depth. Profiles A, B, and C have 3 km integrated optical thicknesses of 1.1, .46, and .08, respectively.
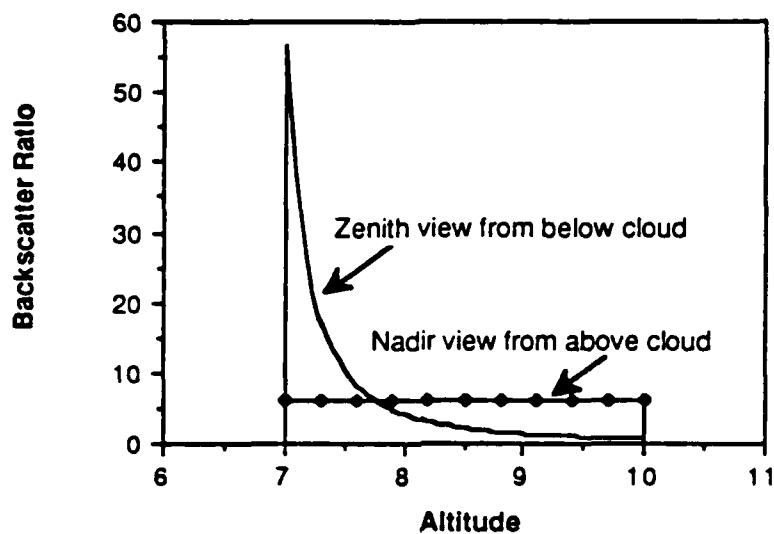
Lidar Profiles Calculated from Extinction Curve A

Zenith view from below cloud

Nadir view from above cloud

Altitude

Backscatter Ratio

Fig. 30 Simulated lidar profile calculated from extinction profile A.

Lidar Profiles Calculated from Extinction Curve B

Zenith view from below cloud

Nadir view from above cloud

Altitude

Backscatter Ratio

Fig. 31 Simulated lidar profile calculated from extinction profile B.
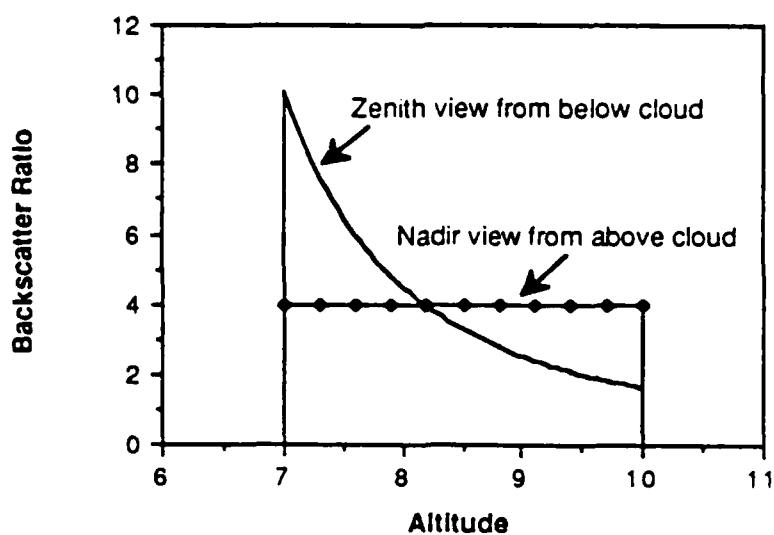
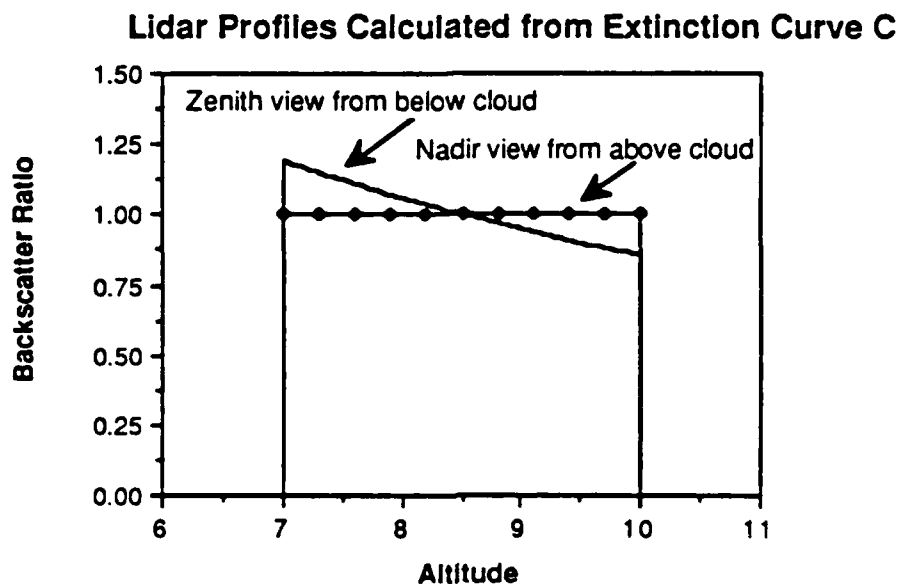## Lidar Profiles Calculated from Extinction Curve C

Fig. 32 Simulated lidar profile calculated from extinction profile C.

Note that equation 4.21 demonstrates that it is physically possible to generate $ß_\varepsilon(R)$ profiles with both positive and negative observed log-slopes. In addition, slant angle entry into clouds can easily produce any variety of signal slopes.

This phenomena does not affect the HSRL technique because of its built-in molecular signal-dependent range calibration; but, the currently proposed space-borne systems are of the simple lidar type. It is important that the designers of such systems and of lidar analysis techniques be wary of this important effect.

Bulk extinction and backscatter phase function estimates coincident with the backscatter cross section profiles have also been calculated using equations 2.7 and 2.10 respectively, where the extinction measurements

were calculated using the log slope of the in-cloud fit line noted in 3 above. In addition, the molecular scattering component has been removed according to eq. 2.9 so that the reported values are cloud-particle extinction cross sections (β_a). The results of these calculations are presented in Table 2. The temperature and RH% estimates presented in table 2 were obtained from high resolution radiosonde measurements released from Platteville, Wisconsin as part of the FIRE effort. The relative humidities values presented are questionable at these low temperatures due to instrumental limitations.

In Fig. 33, the HSRL-determined backscatter phase functions are plotted as a function of temperature. Error bars on the HSRL data are ±1 standard deviation estimated from the summed effects of statistical variations in the background light subtraction and the estimated effects of inaccuracies in the knowledge of Cma and Cmm on the inverted aerosol signal (following the method presented in appendix V of Grund(1984)).

Table 2: Data Summary

Date	Time GMT	Altitude km	β_a 10^{-5} m^{-1}	$P_a/4\pi$* sr^{-1}	T C^0	RH %
10/27/86	23:00	8.0	4 2±.85	.028	-32.6	70
10/31/86	14:25	10.5	2.4±.80	.030	-59 0	59
10/31/86	15:05	10.2	1.9±.72	.032	-51.5	62
10/31/86	15:45	9.1	2.7±1.1	.024	-41 5	68
10/31/86	16 25	8 6	1.8±.83	.039	-38 0	69
10/31/86	16:25	12.1	1.2±.71	.023	-66.5	43
10/31/86	17:05	8.8	1.2±.45	.034	-39.3	69
10/31/86	17 05	12.1	.68±.52	.045	-66.5	43

* Errors in these measurements are plotted in fig. 33.

Platt and Dilley (1984) (hereafter referred to as P&D) presented observations which indicated a straight forward dependence of backscatter phase function on temperature. The phase function values were determined by indirect inference from coincident lidar and IR radiometer measurements. This relationship is also plotted in fig. 33, for comparison. The HSRL has made direct measurements of the backscatter phase function; and, although the current data set is small, it does not demonstrate this dependence of backscatter phase function on temperature.
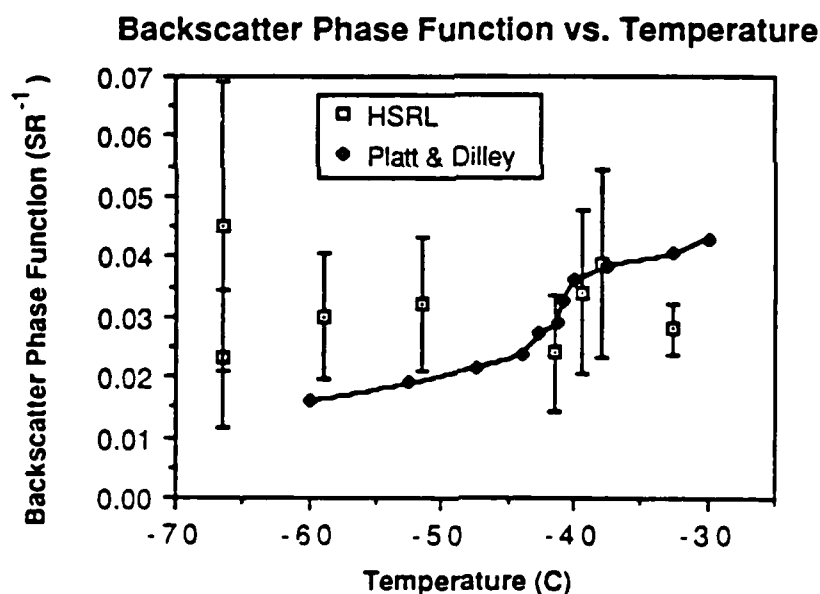
Backscatter Phase Function vs. Temperature

Fig. 33 The relationship of $P_a(\pi)/4\pi$ to temperature as reported by Platt & Dilley (1984) is compared with the independent HSRL measurements acquired during FIRE. A clear cut relationship between backscatter phase function and temperature is not apparent in the latter data set. Mie calculations show that an ensemble of liquid water spheres with an average size parameter of 500 could be expected to exhibit a backscatter phase function of .072 sr^{-1} (Shipley (1978)).

It is important to note several details of the P&D study. As stated in the introduction to this thesis, P&D removed "anomolusly high" backscatter events from their data set, possibly biasing the results. These were data which did not fit an indicated relationship between radiometer determined IR emissivity and lidar measured backscatter. The effects of such data deletions on the functional form of the presented dependence are not clear.

In addition, the radiometer measurements needed to be corrected for surface light contributions. Such contributions to the radiometer signal may have an altitude dependence. Since temperature is strongly correlated with altitude, this effect may influence the relationship shown by P&D.

Further, it has been suggested that the inflection point in P&D's curve is related to the temperature at which water droplets spontaneously freeze without nucleation (in laboratory experiments). It is reasonable to expect a shift in ice crystal habit and light scattering behavior at that temperature. However, during FIRE, liquid water was never observed at temperatures below -35^0 C (Heymsfield (1987)). If this is true of the general case, one would expect the inflection to occur at a temperature 5^0 C warmer than indicated by P&D. It is possible, however, that the ice condensation nucleii found in coastal Australia may be significantly different from those found at the mid-continent location of the HSRL measurements.

V. Summary and conclusions

This thesis has presented the methods by which the University of Wisconsin high spectral resolution lidar technique may be extended to observe cirrus cloud optical properties. The effects of limitations of the current instrument configuration with regard to calibration uncertainties and transmitted power have also been examined. It is important to note that the HSRL is the only currently available, operational, monostatic remote sensing technique capable of making unambiguous and separate determinations of backscatter phase function and extinction in optically thin clouds.

In order to meet some of the needs established in the introduction, the following HSRL observations have been reported:

1. A synoptic depiction has been presented of the cloud cover over Madison, Wisconsin during the FIRE experiment from 10/15 - 11/2 1986. The color RTI displays clearly illustrate the variability, height, physical thickness, and extent of cirrus clouds during this period. Cloud layers often reach 3 km in thickness, yet may be visually quite thin.

2. Measurements of calibrated backscatter cross section have demonstrated the capabilities of the HSRL with regard to operations at cirrus altitudes.

These observations have shown that cirrus cloud tops may be ill-defined. This structure can have detrimental effects on the consistency of determination of cirrus cloud existence, altitudes and thickness from space-borne simple lidar systems.

3. Measurements of bulk average backscatter phase function and extinction have been presented from selected cirrus cloud observations. An attempt has been made to verify the observed relationship between backscatter phase function and temperature presented in Platt and Dilley (1984). Measurements made by the independent HSRL technique do not show this simple relationship for the cases studied.

The evaluation of the HSRL data set has revealed that an increase in the per-pulse power of the laser transmitter would allow observations of cirrus cloud optical properties with the time and/or spatial resolution frequently seen in the evolution of cloud features. To this end, a new, frequency stabilized doubled YAG laser has been specified and is currently in the requisition stage. Integration of this new laser into the HSRL is planned early next year. The new configuration should provide a minimum per-pulse daylight signal gain of 80 over background light which will reduce the necessary averaging time by a

factor of 40 (for conditions equivalent to those of 10/31). In addition, this laser will reduce the non-statistical fluctuations in the uniform aperture illumination tuning ratio observations, thus decreasing the calibration uncertainty. This is because the new laser will not require spectral stripping by an etalon. The current $CuCl_2$ laser requires such stripping, and is subject to small drifts in the angular position of the optical axis. The etalon converts these short term angular drifts into spectral drift.

By use of the calibration techniques established in this thesis, and on incorporation of the new laser into the HSRL, it will be possible to establish an on-going study of the time and range resolved optical properties of cirrus.

Appendix A: Estimation of Multiple Scatter Effects

The term M(R) in equation 2.2 depends upon the probability of a photon arriving at the receiver after more than one scattering event. This discussion will use the techniques and results presented in Eloranta and Shipley (1982) to estimate the accumulated effects of multiple scattering on the HSRL cirrus measurements of 10/31/86. In that presentation, the component of the return signal P_N due to N^{th} order multiple scattering is calculated for n small angle forward scatterings followed by a single backscatter which is subjected to a further $m = N - n - 1$ small angle forward scatterings before impinging on the receiver. The solution to this problem was given as:

$$\frac{P_N}{P_1} = 2^{N-1} <a>^{N-1} \frac{<\mathbb{P}(\pi)>}{\mathbb{P}(\pi)} A_N \frac{\tau^{N-1}}{(N-1)!}$$

(A.1)

Where:

P_1	total return signal from single scatter events
P_N	total return signal from N^{th} order scatter events
$<a>$	fraction of the total scattering in the forward scatter peak
$<\mathbb{P}(\pi)>/\mathbb{P}(\pi)$	average normalized value of the backscatter phase function
A_N	coefficients for estimation of the contribution of multiple scattering for a coaxial monostatic lidar in a spatially homogeneous cloud (see fig. A.1)

$$(0 <= A_N <= 1)$$

R_C range to cloud base

τ optical thickness from R_C to R

Figures A.1 and A.2 show estimations of the parameters A_N and $<\mathbb{P}(\pi)>/\mathbb{P}(\pi)$ as a function of dimensionless parameters, where ψ is the receiver half-angle FOV and $<\Theta_f^2>$ is the mean square angle for forward scattering by cloud particles. It is important to note that the narrow half-angle FOV of the HSRL (160 μR) favors small values of A_N.

From the in-situ cloud samples gathered by Heymsfield (1987) over Oshkosh, Wisconsin, it is believed that the phase function for the crystals extant on this day were similar to the calculations presented in Liou (1980) for randomly oriented hexagonal columns of 60/300 μm. Using Liou (1980) the mean square forward scatter angle is estimated to be $6.7 \cdot 10^{-5}$ radians^2 which yields an A_N of 0.2 from fig. A.1 for second order scattering and a penetration depth of 2 km into a cloud with a base at 10 km. The average value of the backscatter phase function is estimated as 0.7 from fig. A.2. In addition, since the size parameter of the particles is large compared to the laser wavelength, $<a>$ is chosen as 0.5. The optical thickness of a 2 km deep cloud is measured as 0.1 for the conditions observed on 10/31/86.

Using these criteria, the integrated second order scattering contribution to M(R) is estimated to be 1.4% of the integrated single scatter return. Multiple scattering contributions are therefore quite small for the HSRL in thin cirrus measurements and are neglected in the calculations of optical properties in this thesis.
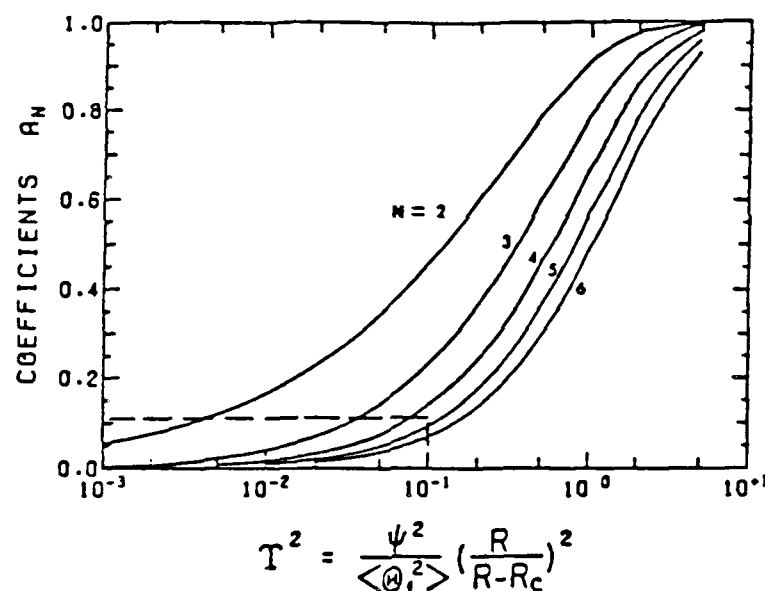
$$T^2 = \frac{\psi^2}{\langle \Theta_1^2 \rangle} \left(\frac{R}{R-R_c}\right)^2$$

FIGURE A.1 *Variation of the coefficients A_N as a function of the parameter T^2 for $2 \le N \le 6$. These coefficients can be used to estimate the contribution of multiple scattering to a coaxial monostatic lidar signal from a spatially homogeneous medium of iostropic backscatters. The area enclosed by the dashed line is shown in an expanded view in Fig. 2.*
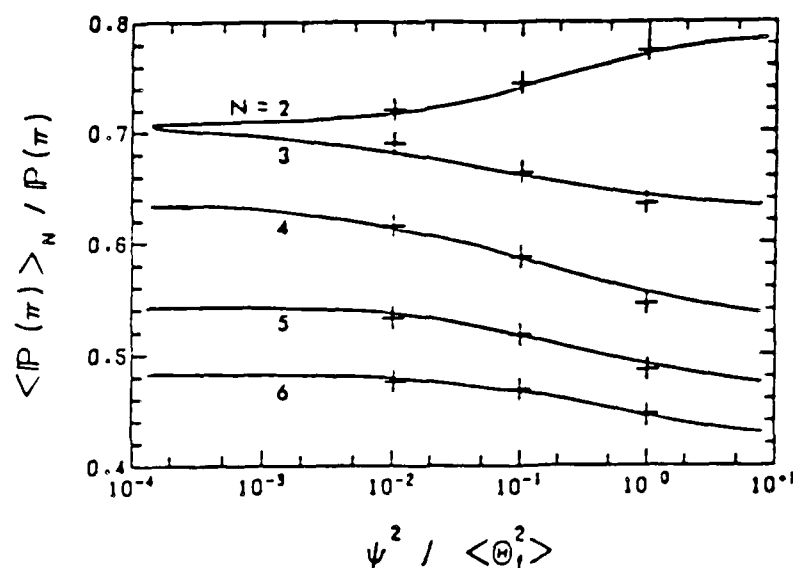

$$\psi^2 / \langle \Theta_1^2 \rangle$$

FIGURE A.2 *The average backscatter phase function for a spatially homogeneous medium with $R_c = 0$, $Q = 1$ and $2 \le N \le 6$. The abscissa is given in terms of the ratio of squared half angle receiver field of view to the mean square angle for forward scattering.*

References

Dubinsky, R.H., A.I. Carswell and S.R. Pal (1985) Determination of cloud microphysical properties by laser backscattering and extinction measurements. App.Opt., 24, pp.1614-1622.

Eloranta, E.W., and S.T. Shipley (1982) A solution for multiple scattering: in Atmospheric Aerosols: Their Formation, Optical Properties and Effects, Ed. A. Deepak., pp. 227-239.

Eloranta, E.W., and D.K. Forrest (1986) Generation of attenuation corrected images from lidar data: in Thirteenth International Laser Radar Conference, NASA conference publication 2431, pp. 291-294.

Eloranta, E.W. (1987) personal communication.

Fiocco, G. and D.B. DeWolf (1968) Frequency spectrum of laser echoes from atmospheric constituents and the determination of the aerosol content of the air. J.Atmos.Sci., 25, pp 488-496.

Grund, C.J (1984) Application of the HSRL model II to measurements of aerosol backscatter phase function and cross section. M.S., Dept. of Meteorology, University of Wisconsin - Madison.

Grund, C.J., and E.W. Eloranta (1985) Measurements of aerosol Backscatter phase function and extinction by high spectral resolution lidar. In the digest from: Topical Meeting on Optical Remote Sensing of the Atmosphere, Op. Soc. of Amer., pp WC11-1 - WC11-4.

Hess, S.L. (1979) Introduction to Theoretical Meteorology. K.E.Krieger, Huntington, N.Y. 362pp.

Heymsfield, A.J (1987) personal communication

Klett, J.D. (1981) Stable analytical inversion solution for processing lidar returns. Appl.Opt. 20, pp 211-220.

Kunz, G.J. (1987) Lidar and missing clouds. In Letters to the editor, Appl.Opt., 26, p 1161.

Liou, K.N. (1980) An Introduction to Atmospheric Radiation. Academic Press, N.Y. 392pp.

Platt, C.M.R. and A.C. Dilley (1981) Remote sounding of high clouds. IV: Observed temperature variations in cirrus optical properties. J.Atmos.Sci., 38, pp1069-1081.

Platt, C.M.R. and A.C.Dilley (1984) Determination of cirrus particle single-scattering phase function from lidar and solar radiometric data. App.Opt., 23, pp 380-386.

Russell, P.B., B.M. Morley, J.M. Livingston, G.W. Grams, and E.M. Patterson (1981) Improved Simulation of Aerosol, Cloud, and Density Measurements by Shuttle Lidar. NASA contractor report 3473. 155 pp.

Sassen, K., and K.N. Liou (1979) Scattering of polarized laser light by water droplet, mixed-phase and ice crystal clouds. Part I: Angular scattering patterns. J.Atmos.Sci., 36, pp 838-851.

Shettle, E.P., and R.W. Fenn (1979) Models for the Aerosols of the Lower Atmosphere and the effects of Humidity Variations on their Optical Properties. AFGL-TR-79-0214, 94 pp.

Shipley, S.T., J.H. Joseph, J.T. Trauger, P.J. Guetter, E.W. Eloranta, J.E. Lawler, W.J. Wiscombe, A.P. Odell, F.L. Roesler, and J.A. Weinman (1975) The Evaluation of a Shuttle Borne Lidar Experiment to Measure the Global Distribution of Aerosols and Their Effect on the Atmospheric Heat Budget. Final Report NSG-1057, 150 pp.

Shipley, S.T. (1978) "The measurement of rainfall by lidar", Ph.D. Thesis, U. of Wisconsin-Madison, 187 pp.

Shipley, S.T., D.H. Tracey, E.W. Eloranta, J.T. Trauger, J.T. Sroga, F.L. Roesler, and J.A. Weinman (1983) High spectral resolution lidar to measure optical scattering properties of atmospheric aerosols. 1: Theory and instrumentation. App.Opt., 22, pp 3716-3724.

Spinhirne, J.D., J.A. Reagan, B.M. Herman (1980) Vertical distribution of aerosol extinction cross section and inference of aerosol imaginary index in the troposphere by lidar technique. J.Appl.Meteor., 19, pp 426-438.

Sroga, J.T., E.W. Eloranta, S,T. Shipley, F.L. Roesler, and P.J. Tryon (1983) High spectral resolution lidar to measure optical properties of atmospheric aerosols. 2: Calibration and analysis. Appl.Opt., 22, pp 3725-3732.

Starr, D.O'C., and S.K. Cox (1985) Cirrus clouds. Part II: Numerical experiments on the formation and maintenance of cirrus. J.Atmos.Sci., 42, pp 2682-2694.

Starr, D.O'C., and S.K. Cox (1985b) Cirrus clouds. Part I: A cirrus cloud model. J.Atmos.Sci., 42, pp 2663-2681.

Stephens, G.L., and P.J. Webster (1981) Clouds and climate: Sensitivity of simple systems. J.Atmos.Sci., 38, pp 235-247.

Weinman, J.A. (1976) Effects of multiple scattering on light pulses reflected by turbid atmospheres. J. Atmos. Sci., 33, pp1763-1771.

Weinman, J.A. (1984) Tomographic lidar to measure the extinction coefficients of atmospheric aerosols. App.Opt., 23, pp 3882-3888.

Welch, R.M., S.K. Cox, and W.G.Zdunkowski (1980) Calculations of the variability of ice cloud radiative properties at selected solar wavelengths. App.Opt., 19, pp 3057-3067.

Wendling P., R. Wendling, H.K. Weickmann (1979) Scattering of solar radiation by hexagonal ice crystals. App.Opt., 18, pp 2663-2671.

Wylie, D.P., and W.P. Menzel (1986) Cloud statistics using VAS. From: Proceedings of the 26th COSPAR conference in Toulouse, France, pp A.1.1-A.1.10.

END
DATE
FILMED
DTIC
JULY 88